Characterization and Utilization

of Self-Assembled

Diphenylalanine Nanotubes

Kairuo XU BSc.

Thesis submitted to

The University of Nottingham for the degree of

Doctor of Philosophy

September 2011

Abstract

Diphenylalanine (FF) peptide is the core-recognition motif of β-amyloid polypeptide, a peptide associated with diseases such as Alzheimer's and which is known to be capable of self-assembly. FF has attracted interest in nanotechnology due to the physical and chemical stability and mechanical rigidity of the self-assembled nanotube form of the peptide. A number of promising applications of FF nanotubes have previously been explored. To extend this work to biomedical and pharmaceutical areas, an improved understanding of the physicochemical properties of FF tubes, together with the influence of assembly conditions, cytotoxicity properties and potential in drug delivery field are presented in this thesis.

The studies presented in Chapter 2 address the self-assembly of FF peptide prepared by two known methods of preparation, one aqueous based, the other utilizing an organic solvent. A range of complementary characterization methods is applied including atomic force microscopy, scanning electron microscopy, focused ion beam-scanning electron microscopy, X-ray powder diffraction, and Raman Spectroscopy. The investigations reveal differences in morphology of the tubes formed by the different preparation methods. The aqueous based method produces tubes that are long, straight and unbranched and are consistent with previous work. The alternative organic solvent method produced tubes that are shorter and narrower. In addition, these tubes displayed flexibility and nucleation points. Following on from these findings, a proposed mechanism of tube growth is discussed.

Chapter 3 further extends the investigation to the biological field. Possible cytotoxicity issues are studied using a MTT assay on a HeLa cell line. Moreover, total internal reflection microscopy was applied to investigate HeLa cell behaviour in the presence of FF nanotubes. The results from these studies reveal that the nanotubes and FF peptide do not cause any mitochondrial related damage to HeLa cells. Furthermore, short tubes were observed to be taken up by cells through a suggested macropinocytosis pathway.

Finally, in Chapter 4 the focus turns to the investigation of the potential of FF tubes as drug carriers in drug delivery. Here, successful synthesis of drug-loaded FF tubes is presented with two model drugs. The physical characterization of the complex formed under different conditions using scanning electron microscopy reveals FF nanotube self-assembly is a drug concentration and solvent type dependent process. Finally, *in vitro* drug release from FF nanotubes is performed and compared to that of the drug alone. Extended drug release is observed for both drug candidates and release mechanisms are proposed.

The results presented throughout this thesis demonstrate the versatility of self-assembling FF peptides for the formation of tubular nanostructures with different morphologies and physical properties under different conditions. The assembled nanostructures appear non-toxic to cells and offer promise in drug delivery as novel drug carriers.

Acknowledgements

I would like to thank my supervisors, Professor Clive Roberts, Professor Saul Tendler and Dr Cynthia Bosquillon, for their continuous guidance and various contributions towards this thesis and throughout the whole project. I would like to thank the University of Nottingham and Professor Clive Roberts for funding this project.

There are many within my research group and the School of Pharmacy whom I would like to thank for their helps and advices during my studying and writing periods. Many thanks to Dr Stephanie Allen for the advice and guidance throughout the PhD study, Professor Xinyong Chen for the training on AFM, Dr Jonathan Burley for the help on XRPD and Raman spectroscopy, Dr Christopher Parmenter for FIB-SEM experiment, Mrs Christine Grainger-Boultby for her assistance on the SEM, Mr Colin Wills for the instruction and advices on the drug dissolution test, Mr Paul Cooling on the UV-visible spectroscopy training. I would like to express my thanks to all the lovely friends I have made in Nottingham.

I wish to thank for three important people in my life. I thank my Mum and Dad for their support and faith during my PhD, especially my Mum who has given me so many helpful advices throughout the project. Finally, thank you Haotian for always being there and without his understanding everything would have been so much different.

Contents

List of Figures

List of Tables

Chapter 1 Introduction

1.1 Protein folding and misfolding

Proteins serve important functions in our life; they are among the most important molecules in living organisms and are crucial to the maintenance of life. There are more than a million different proteins in our body and over half the dry weight of a cell is comprised of proteins [1, 2]. They take part in almost every chemical process that occurs within our body and have always attracted interest in research and investigation.

Proteins are made up of amino acids linked by peptide bonds [3]. There are 20 naturally occurring amino acids. The sequence which these amino acids occur within the polypeptide chain is referred to as the primary structure of a protein. The secondary structure of a protein is referred to the localized organization of the polypeptide chain; different spatial arrangements such as α-helices or β-sheet structures are formed as a result of hydrogen bonds between the side chains of the amino acids. These secondary elements further arrange themselves to create functionalized domains which are referred to as the tertiary structure of a protein. All of the domains are held together by ionic, disulfide and salt bridges and other non-covalent interactions such as van der Waals forces between different amino acid residues. For the majority of proteins that are comprised of more than two polypeptide chains, the final level of structural organisation is the quaternary structure which is completed by the

assembly of each subunit into a functionalized final structure (Figure 1-1) [3]. The secondary and tertiary structural elements of proteins are various and adopt different orientations and combinations, which then self-assemble into intricate 3D structures. Ultimately this is based on the primary amino acid sequence, which has been selected to achieve a certain function through evolutionary pressure [4-6].
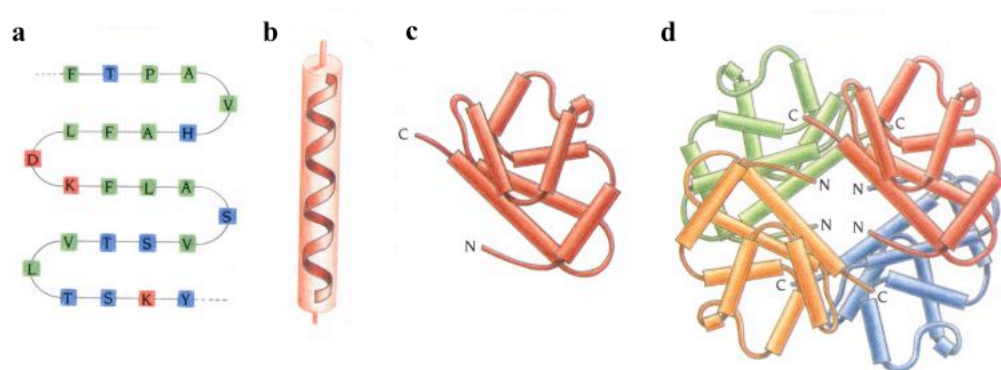
Figure 1- 1 Protein structures. (a) The amino acid sequence of a protein is referred to as the primary structure; (b) different units of the sequence form the secondary structures via hydrogen bonding between residues of the amino acids presented in the sequence; (c) these elements further arrange themselves into tertiary structure that is stabilized by ionic, disulfide and salt bridges and other non-covalent interactions; (d) quaternary structure of a protein is completed by assembly of each polypeptide chains into a functionalized final structure [5].

1.1.1 Underlying mechanism of protein folding

Protein folding is a complex process still far from fully understood. There are 20 naturally occurring amino acids hence the total possible number of primary sequences is extremely large. Moreover, there are various secondary structures

with different orientations and combinations. All these elements self-recognise and fold into the final complex structure with specific functions within milliseconds. One may question how such a complex structure can be created from numerous possible elements and combinations within such a short amount of time. Indeed, Levinthal proposed this question in 1968 which is known as Levinthal's paradox, which states that it is impossible for a protein to adopt all possible conformations in such a short time in search for the correct fold [6]. This paradox was solved recently evidenced upon a large number of experimental and theoretical studies, and the proposal of the energy landscape theory [7-12]. It is now believed that protein folding process is a 'random search' rather than a restricted pathway; each possible conformation accessible to a polypeptide chain is included in the searching process and the search is based on the entropy, enthalpy and free energy of each available conformation. The search is made possible because the native conformation is, in general, more stable and requires less energy than the non-native states [13-15]. This description of protein folding is referred to as the 'new view' of the protein folding process [16]. The conceptual basis of this approach is shown in Figure 1-2. In general, each possible conformation of a protein is associated with a specific free energy. Plotting free energies against the corresponding conformations generates an energy landscape and the resultant 'funnel shape' leads to the final correct conformation, ensuring the number of conformations accessible to a polypeptide chain is always reduced as the search approaches the native state [2, 16]. During folding, proteins, especially ones with large numbers of amino acid residues, often form intermediate states; the native state

is the most stable formation thus enthalpy favoured which compensates the decreased entropy as a result of the reduced disorderness of the native state [2, 16].

An earlier model that describes the mechanism of protein folding was proposed by Fersht, and is known as the 'nucleation-condensation' model [11, 17, 18]. This model proposes that during the folding process, a folding nucleus of a small number of key residues forms first, followed by the spontaneous formation of secondary and tertiary structures as the whole protein condenses around the nucleus.

Proteins are synthesized inside of ribosome within cells. Few proteins fold spontaneously in a co-translational manner whilst a nascent chain is still attached to the ribosome [19, 20]. The majority of protein folding undergoes a much more complex route, which occurs in the cytoplasm or endoplasmic reticulum [21]. Considering the crowded environment in the cell, where the concentration of macromolecules can reach 400 mg/ml [22], newly synthesized polypeptide chains can easily interact with surrounding cellular components and result in misfolding in this environment. To prevent this from occurring, cells have a number of strategies, one of them being the molecular chaperones [23-27].
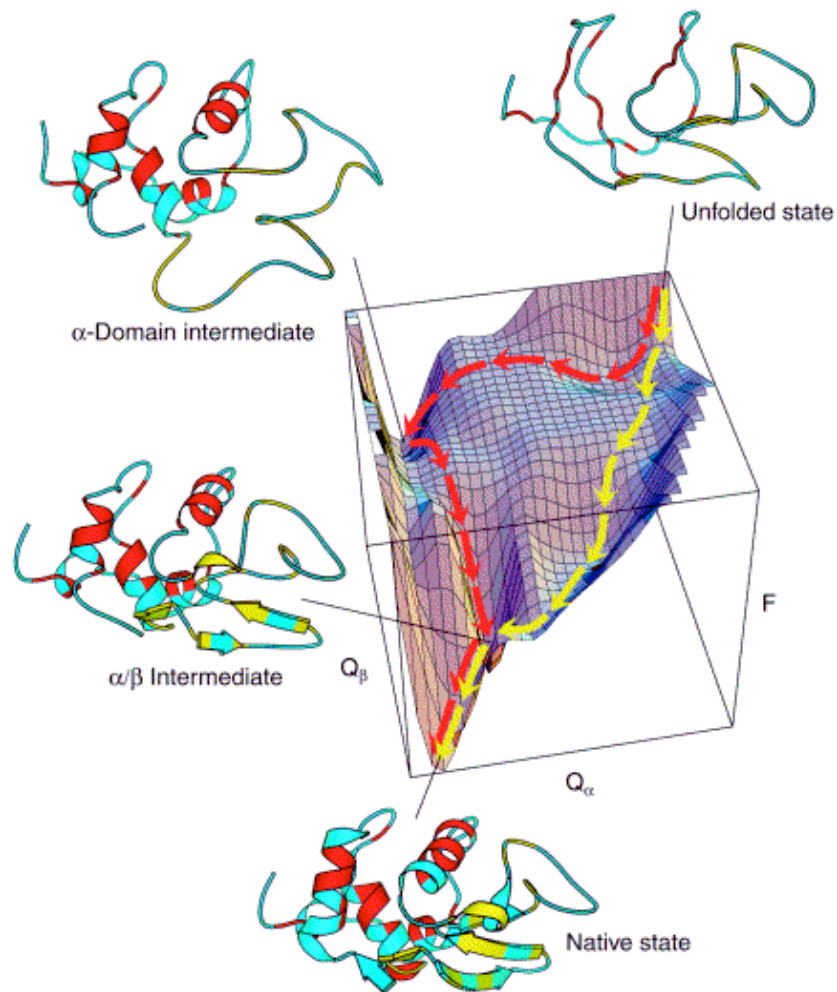
Figure 1- 2 Energy landscape for the folding of lysozyme which has 129 residues and consisting of two domains, denoted as α or β. The free energy (F) is represented as a function of the number of possible conformation (Qα and Qβ). The schematic energy landscape has a 'funnel-like' shape that ensuring the efficiency of folding [16].

The function of molecular chaperones is to bind to polypeptide chains at the regions that are not normally present in the final structure e.g. unwanted backbone parts, thereby maintaining them in a folding competent conformation, shielding them from their surroundings [28]. For proteins that

have misfolded, cytosolic enzymes recognise and tag them with ubiquitin molecules, from where they undergo further assembly in the assist of proteasome to be degraded [29, 30].

1.1.2 Protein misfolding and diseases

Despite the natural defence mechanisms that prevent proteins from misfolding, there are a large number of diseases caused by, or related to, the abnormal folding of proteins [2, 31-44]. The causes of protein misfolding are diverse; for example, it can be triggered by mistranslation [45], mistranscription [46] or gene mutation [47], which all lead to the disturbance of the primary sequence of the protein. Alternatively errors could occur after protein synthesis is completed; changes of surrounding conditions such as pH or temperature could cause destabilization of protein, resulting in misfolding or unfolding [48-50]. Failure to fold correctly will give rise to the malfunctioning of proteins and possibly lead to disease [34, 37, 51, 52]. Alternatively, misfolded proteins can create intractable aggregations which are related to a number of diseases, for instance, Alzheimer's and Parkinson's diseases [35, 53]. Some of the diseases associated with protein misfolding are presented in Table 1.1.

Table 1. 1 Representative protein folding diseases [53].

Disease	Protein	Site of folding
Hypercholesterolemia	Low-density lipoprotein receptor	ER
Cystic fibrosis	Cystic fibrosis trans-membrane regulator	ER
Phenylketonuria	Phenylalanine hydroxylase	Cytosol
Huntington's disease	Huntington	Cytosol
Marfan syndrome	Fibrillin	ER
Osteogenesis imperfecta	Procollagen	ER
Sickle cell anaemia	Haemoglobin	Cytosol
α1-Antitrypsin deficiency	α1-Antitrypsin	ER
Tay-Sachs disease	β-Hexosaminidase	ER
Scurvy	Collagen	ER
Alzheimer's disease	Amyloid β-peptide/tau	ER
Parkinson's disease	α-Synuclein	Cytosol
Scrapie/Creutzfeldt-Jakob disease	Prion protein	ER
Familial amyloidoses	Transthyretin/Lysozyme	ER
Retinitis pigmentosa	Rhodopsin	ER
Cataracts	Crystallins	Cytosol
Cancer	P53	Cytosol

1.1.3 Amyloid fibril formation

It is known that a number of diseases caused by protein misfolding are associated with the occurrence of protein aggregations called amyloid fibrils [32, 54, 55]. Examples include Alzheimer's disease that is associated with amyloid β-peptide [56-60], type II diabetes which is associated with the islet amyloid polypeptide [61-63], and Creutzfeldt-Jakob disease that is associated with prion protein [64, 65] (some of these diseases are shown in Table 1.1). These stable, insoluble aggregates are very resistant to protease degradation and share similar morphology but not necessarily obvious gene sequences [66]. The common structure of amyloid fibrils is usually made up of 2-6 protofilaments (i.e. the fibrillar subunits) that twist around each other with an overall diameter of few nanometres in width and a few micrometres in length suggesting that amyloid fibrils might be a generic conformation that all proteins could adopt (Figure 1-3) [67]. Furthermore, it is now suggested that amyloid fibrils may be the consequence of the pathological changes related to disease state, rather than the cause of the associated diseases [66]. Indeed, there are examples of proteins or polymers that can form amyloid fibrils that share common morphology and display similar properties *in vitro*, examples include myoglobin [68] and polylysine [69], and short peptides taken from the sequence of amyloid polypeptides [70]. These proteins follow a nucleation-dependent process just like the rest of amyloid fibrils formations. The aggregation is most likely to occur from partially folded intermediates, and is characterized by a critical concentration below which no aggregation will

occur, followed by a lag phase then a period of rapid growth, and eventually a

steady state phase where monomers are in equilibrium with fibrils [71, 72].
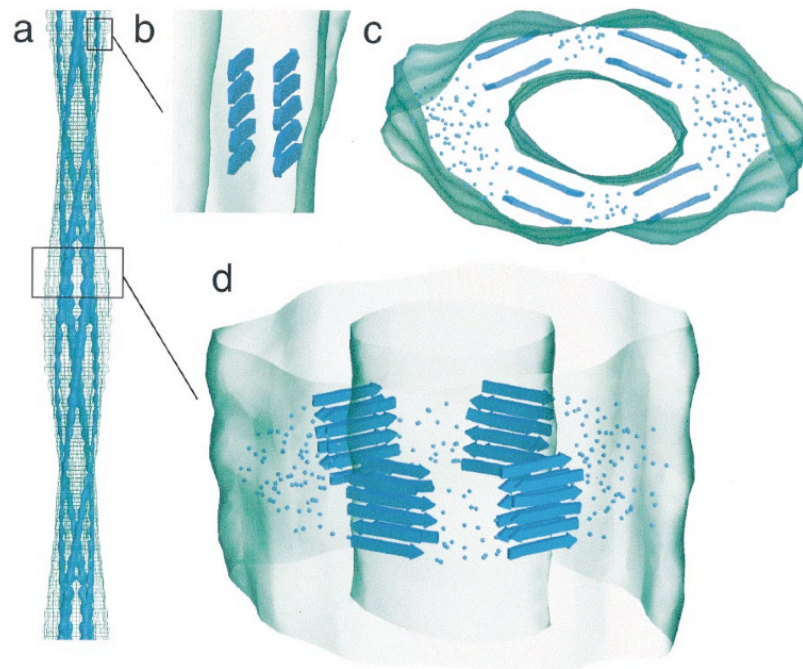
Figure 1- 3 A molecular model generated from cryo-EM analysis of an amyloid fibril grown from an SH3 domain. Figure 1-3a is a representation of an overview of the fibril structure; four twisted protofilaments are shown in blue. Figure 1-3b represents the side view of a single protofilament. Figure 1-3c represents the cross-section of the fibril and Figure 1-3d is a slightly tilted side view of the fibril. The outer surface of the fibril is shown in green and the direction of the β–sheet packing is shown by the blue arrows [67].

1.2 Molecular self-assembly into various diphenylalanine-based nanostructures

As mentioned above, the ability to form amyloid fibrils appears general; there are various investigations of short peptide fragments taken from parent amyloid proteins that undergo self-assembly in mild *in vitro* conditions into amyloid-like nanofibrils [73-75]. One study that investigated the minimal amyloidogenic fragments within β-amyloid polypeptide led to the discovery that the short dipeptide, diphenylalanine (FF) could self-assemble [76]. It is now known that this core-recognition motif of β-amyloid polypeptide rapidly self-assembles into discrete tubular nanostructures that retain many characteristics of amyloid fibrils formed by the parent polypeptide, for instance, birefringence in polarized light with Congo red staining and β-sheets conformation [77, 78].

Since the emergence of FF as the simplest self-assembling building blocks, many studies have been carried out to investigate the physical and chemical properties of FF and its self-assemblies [79-82]. The nanostructures formed by FF peptide are diverse ranging from nanotubes and nanorods to spherical vesicles [83]. A summary of various FF nanostructures and their potential applications is presented in Figure 1-4. For each type of nanostructure a detailed review of its chemical and physical characteristics, together with its previous studies and potential applications will be discussed later.
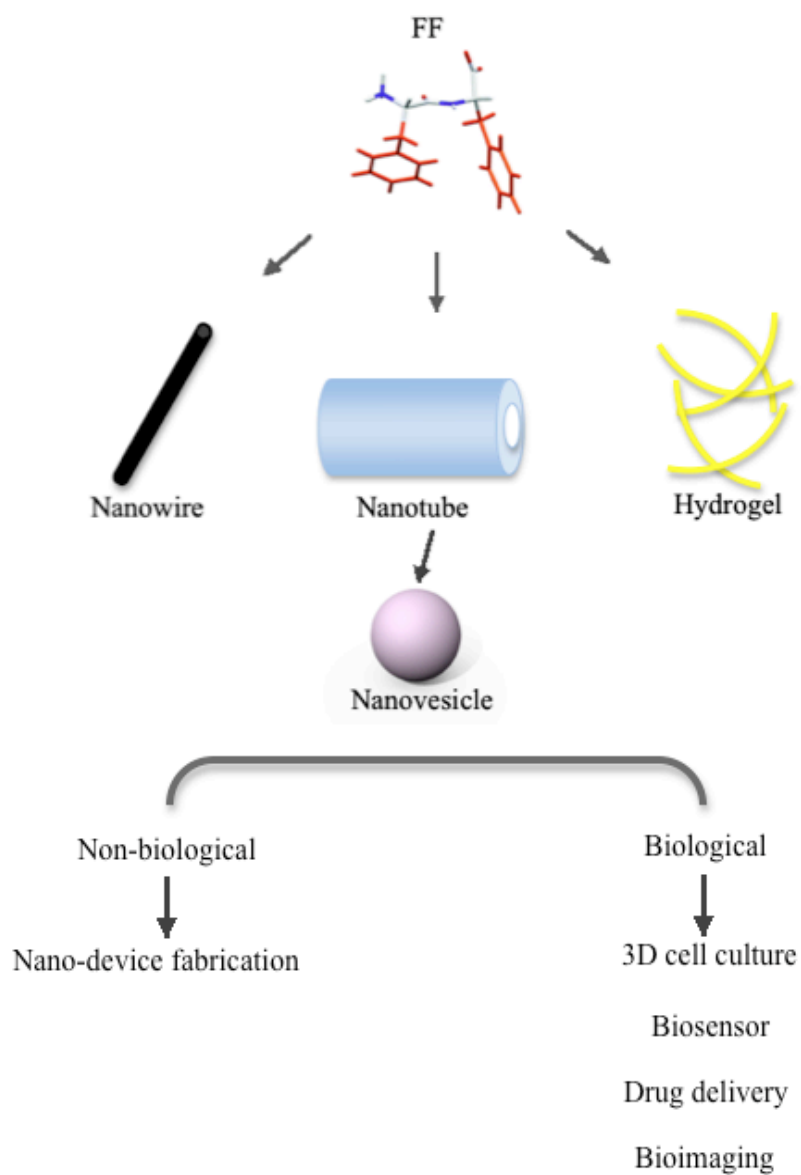
Figure 1- 4 Schematic representation of various nanostructures formed by diphenylalanine-based peptide building blocks and their potential applications.

1.2.1 FF-based nanotubes

Reches and Gazit have shown that FF, like the complete β-amyloid sequence, can undergo rapid self-assembly in mild *in vitro* conditions [84]. The nano- and micro- structures formed have been studied by a range of techniques, including atomic force microscopy (AFM) [79, 81, 85], scanning electronic microscopy (SEM) [86, 87] and transmission electronic microscopy (TEM) [79, 88]. These studies have shown that the assembled FF adopts a hollow tubular structure, with open ends. The diameters of such tubes vary from around 50 to 2000 nm depending primarily upon the original concentration of the peptide [89]. FF tubes are long on the nanoscale, discrete and unbranched, with a persistence length up to hundreds of microns, and a Young's modulus of approximately 19 GPa [78]. The mechanical stiffness of FF tubes is comparably higher than other biological materials, such as amyloid fibrils formed from protein insulin (Young's modulus = 3.3 GPa) [90] and other synthetic polypeptides (e.g. amyloid fibrils self-assembled from poly-Val-Gly-Gly-Leu-Gly have a Young's modulus in the range from 3.5-7MPa) [91]. FF tubes also display remarkable thermal stability up to 90 °C; the tube structural integrity is lost and phenylalanine released at temperature above 150 °C [79, 92, 93]. Moreover, the chemical stability of FF nanotubes in various organic solutions has also been investigated revealing that FF nanotubes have outstanding chemical stability. One such study investigated FF nanotube solutions mixed with various organic solutions including ethanol, methanol, isopropanol, acetone and acetonitrile for half an hour, and then the incubated solutions were air-dried and investigated with SEM analysis to reveal the assembled tubes,

showing the stability of FF nanotubes in these solvents [79]. Furthermore, the stability of FF nanotubes submerged in acetone and acetonitrile for half an hour was also investigated using SEM analysis, where again the FF tubes retained their structure [79]. Taken together, these remarkable properties have made FF nanotubes among the stiffest biological materials presently known, enabling the potential of FF nanotubes for nano-fabrication applications.

There are two methods of FF nanotube preparation published to date, one established by Gazit's group [76], and the other reported by Song's group [89]. The former method of preparation involves dissolving FF peptide (L-Phe-L-Phe) in an organic solvent, 1,1,1,3,3,3- hexafluoropropan-2-ol (HFIP), followed by dilution with water. Another preparation omits HFIP by heating FF peptide (D-Phe-D-Phe) at 65°C in water for thirty minutes and the solution was then cooled to room temperature. The latter preparation avoids the toxic HFIP which is known to be extremely destructive to tissues of the mucous membrane, upper respiratory tract and eyes [94], thus making this approach more attractive for the potential development of FF nanotubes as drug delivery systems and other *in vivo* applications. AFM and SEM visualization of these nanotubes show no apparent difference in morphology from those prepared in a HFIP/water mixture, although they exhibit slightly larger diameters (ranging from 400-2000 nm) [89].

Gazit's group investigated the rationale behind the process of molecular self-assembling of FF, they hypothesized that the dipeptides are linked via hydrogen bonding to cause one-dimensional propagation. The resultant

intersheet stacking interaction between aromatic groups of FF provides an energetic contribution to forming the extended β-sheet, i.e. a two-dimensional layer. The final overall tubular structure is accomplished by closure of the extended sheet along one axis of the 2D layer (Figure 1-5) [83].

FF   Extended β-sheets   Closure of 2D layer   FF nanotube
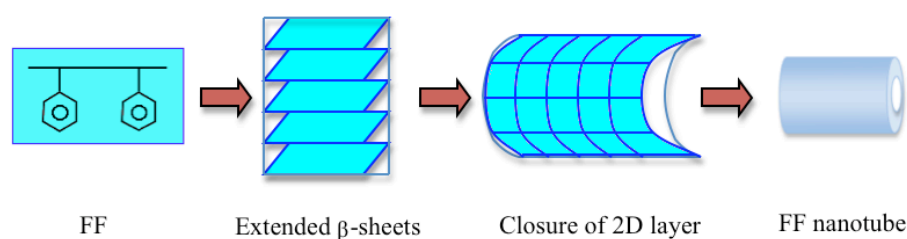
Figure 1- 5 Model for the assembly of the diphenylalanine nanotube. Extended β-sheet is formed as a result of π-π stacking interactions between the aromatic groups of FF molecules, a closure of the sheet gives the final tubular structure that is further stabilized by H- bonding and aromatic interactions.

This hypothesis is consistent with previous evidence found by Makin's group, where they suggested the importance of phenylalanine groups in amyloid fibril formation by means of π-π stacking interactions [95]. The molecular packing of FF nanotubes was further investigated by Gorbitz. His group found that FF nanotubes have chiral hydrophilic channels composed of 6 numbers of peptide per turn with a van der Waal's diameter up to 10Å (Figure 1-6) [96]. Water molecules stay well ordered in the hydrophilic channels [96-98]. This finding is consistent with previous result from Song's group, which they have found there were parallel channels running in the direction of the FF tube axis [89].
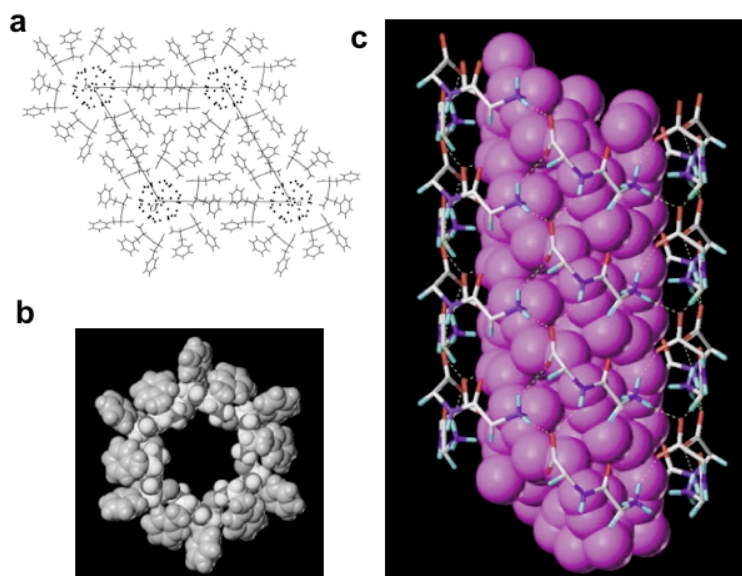
Figure 1- 6 Molecular packing arrangement of diphenylalanine nanotubes. The unit cell and molecular packing of FF tube was presented in 1-6a showing each unit composed of 6-FF molecules with peptide backbones arranged in the centre and hydrophobic aromatic rings oriented outside. Small spheres represent water molecule positions. A single channel view from the top is presented in 1-6b, and a side-view of the channel is presented in 1-6c. Purple clusters represent water molecules that stay in the centre of the channel [96].

Many efforts have been applied to achieve ordered spacial organization of self-assembled FF nanotubes. Several strategies have been developed to achieve both vertical and horizontal alignment of FF tubes [80, 99-103]. Vertically aligned 'nanoforests' by axial unidirectional growth of FF peptide tubes was achieved by a vapour deposition method [99]. FF peptide powder was heated to 220 °C and at this temperature FF molecule altered the chemical structure from liner to cyclic, cyclo (-Phe-Phe). The subsequent assembly was achieved on a substrate placed above the peptide source to form the ordered vertical alignment of the FF nanotube array (Figure 1-7).
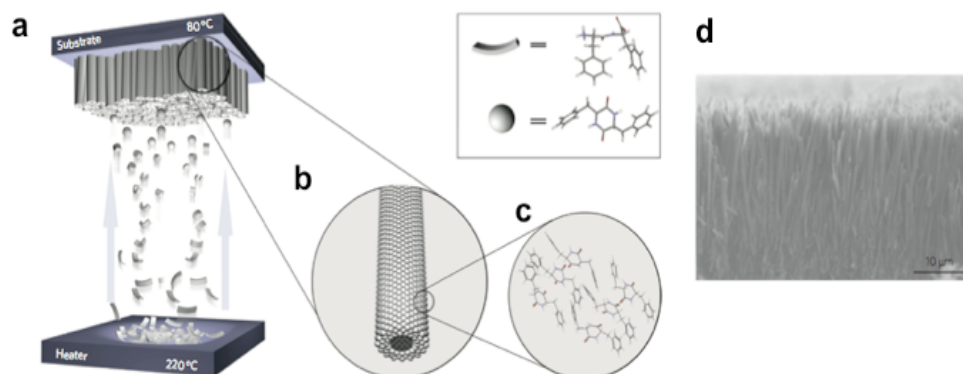
Figure 1- 7 Vertical alignment of diphenylalanine nanotubes. A schematic representation of the vapour deposition technique is shown in 1-7a; a representation of a single peptide nanotube is shown in 1-7b; the molecular arrangement of a unit cell composing 6 Cyclo-Phe-Phe molecules is presented in 1-7c and a typical SEM image of the vertically aligned nanoforest (side-view) is presented in 1-7d [99].

In another study, vertical alignment was achieved by using a FF peptide thin film as a template to grow tubes [102]. FF peptide was dissolved in HFIP in the complete absence of water to produce an amorphous peptide thin film first; the film then acted as a template under the proper amount of water vapour or high thermal energy (above 100 °C) to grow FF nanorods (nanorods were used to describe the assembled nanostructures rather than nanotubes as these assemblies were solid inside under SEM) (Figure 1-8). The powder X-ray diffraction pattern of the native FF nanotubes was also different from that of the FF nanorods, indicating a change in the crystal structure of the nanorods. Time-of-flight secondary ion spectroscopy and high-performance liquid chromatography have shown the presence of cyclo (-Phe-Phe), instead of the linear H-Phe-Phe-OH in the assembled aligned structure. This finding is in

good agreement with the former study which also pointed out the change of FF structure from liner to cyclic [99]. Furthermore, horizontal alignment of FF nanotubes has also been demonstrated by coating ferrofluid on the surface of nanotubes or exposing them to a strong magnetic field without any additional treatment [104].
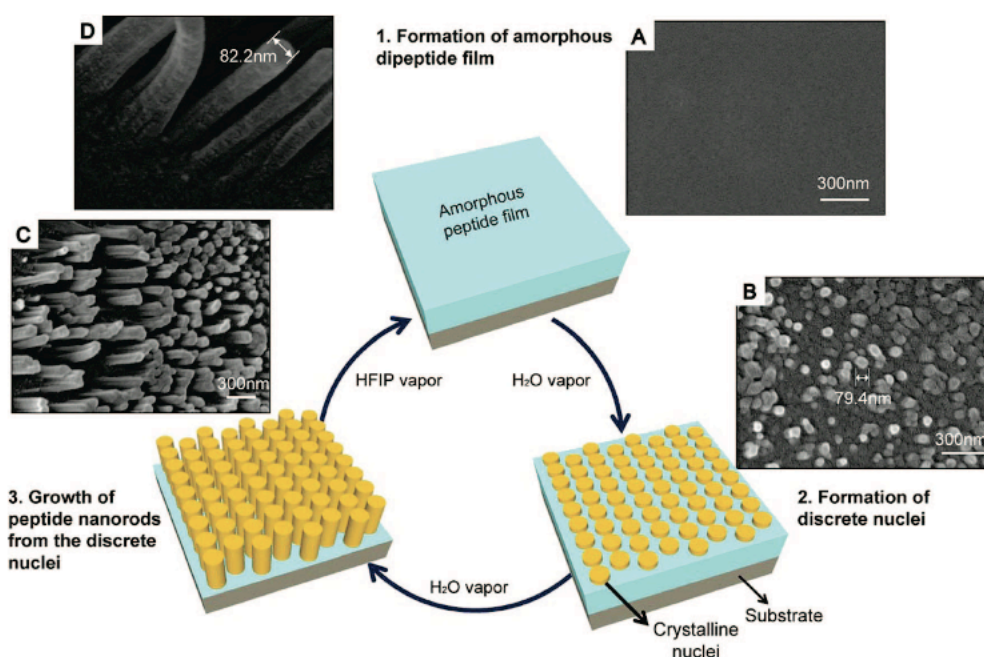
Figure 1- 8 Vertical alignment of diphenylalanine nanorods from a peptide thin film. SEM micrographs are presented from A to D with schematics representing the effect of water on the formation of ordered peptide nanorods. Starting from the right: (A) Amorphous dipeptide film was formed by placing a drop of FF dissolved in HFIP on solid substrate and allowing to evaporate in the absence of water; (B) formation of discrete nuclei was achieved after water vapour treatment; (C) unidirectional growth of FF nanorods from nuclei after further water vapour exposure; (D) high-resolution SEM image of FF nanorods [102].

1.2.2 Phase transition of diphenylalanine from nanotubes to nanovesicles

Interestingly, in the original work demonstrated by Song's group, spherical nanostructures were found together with nanotubes (Figure 1-9) [89]. They claimed that by further diluting one part of the nanotube solution with an equal volume of water, vesicles with diameters of a few hundred nanometres were observed. This finding has led to the suggestion that the concentration of the peptide is a key factor in the formation of the nanotubes and may play an important role in determining the morphology of the assemblies. Precise control of the shape and the size of the self-assembled nanostructures enables their applications in nanofabrication, therefore an understanding of the structural transition and the key factors that may influence the shape and the size of the final nano-assemblies are crucial.
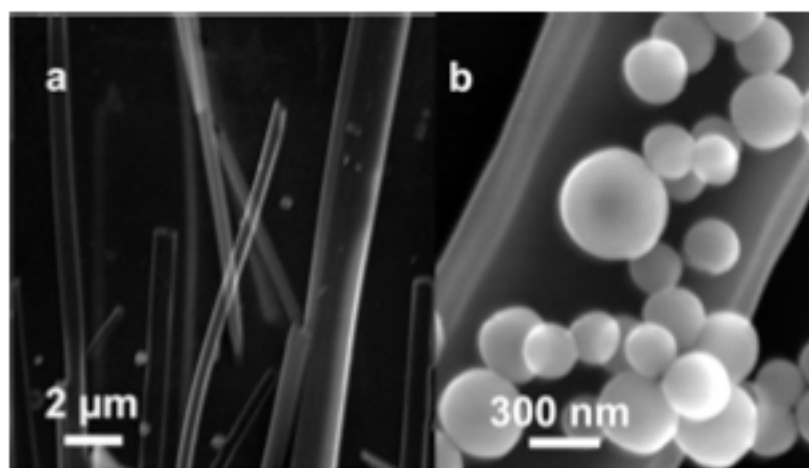
Figure 1- 9 SEM micrographs of (a) diphenylalanine nanotubes and (b) nanotubes mixed with nanovesicles [89].

There are a number of features that may affect the formation and the shape of FF nanotubes, including concentration of the peptide [105], solvent type [106, 107], solvent pH [107], temperature [108], and chemical modification of the peptide [109]. Monomer-concentration-induced shape transition is found to be very common not only for FF, but other materials [110, 111]. For instance, the formation of micelles is critically dependent upon the concentration of the monomer, and micellization will only occur when the monomer concentration reaches a specific point, known as the critical micelle concentration. This is characteristic of all nucleation-dependent processes [112]. After the monomer critical concentration is reached, a lag phase when nucleus is formed from monomers occurs, followed by an elongation phase when tubes are growing out from the nucleus, and eventually to a steady state when monomers and nanotubes are at equilibrium. Li and co-workers have described the shape of the assemblies as dependent on three energy terms: the internal cohesion energy that compensates the decrease of entropy when random monomers (isotropic phase) form ordered nuclei (aggregation phase); the energy associated with the isotropic-aggregation interface; and the shape-dependent curvature elastic energy of the layer (i.e. the free energy cost related to other degrees of freedom of molecules in aggregation phase, for example, the orientation of growth of aggregations) [113]. Using these concepts they were able to define the critical tube-to-vesicle monomer concentration (CTVC) by the following expression (Equation 1.1):

$$CTVC = C_A e^{-3\gamma/hC_A k_B T} \qquad (1.1)$$

Where C_A is the molecule concentration of aggregation phase, γ is the surface tension constant of solution/aggregation interface, k_B is the equilibrium constant, and T is temperature [113].

Solvent type, pH and concentrations are other important factors affecting the shape of self-assembled nanostructures [106]. A study conducted by Zhu's group revealed a structural transition from gel to flower-like microcrystal of an organogel self assembled from FF in toluene after introducing ethanol as a co-solvent [106].

Examples of temperature-driven phase transformation in self-assembled FF nanotubes have been described [99-103, 114]. A change was observed in the original molecular assembly of FF at 220 °C [99] (100 °C [102] and 140 °C – 150 °C [114] from other studies) from a linear peptide to a cyclic structure. The XRPD analysis indicated an irreversible phase transition of FF from a non-centrosymmetric hexagonal space group to a centrosymmetric orthorhombic space group.

Introducing chemical modification during FF tube assembly has been demonstrated to form closed-cage nanostructures [83]. After dissolving FF peptide in HFIP, 2-iminothiolane dissolved in dimethyl sulfoxide with 2% N,N-diisopropylethylamine was added to the solution and spherical nanostructures with diameters around a few hundred nanometres were observed. The transformation into spherical nanostructures was achieved upon complete closure of the extended β sheet (Figure 1-10).
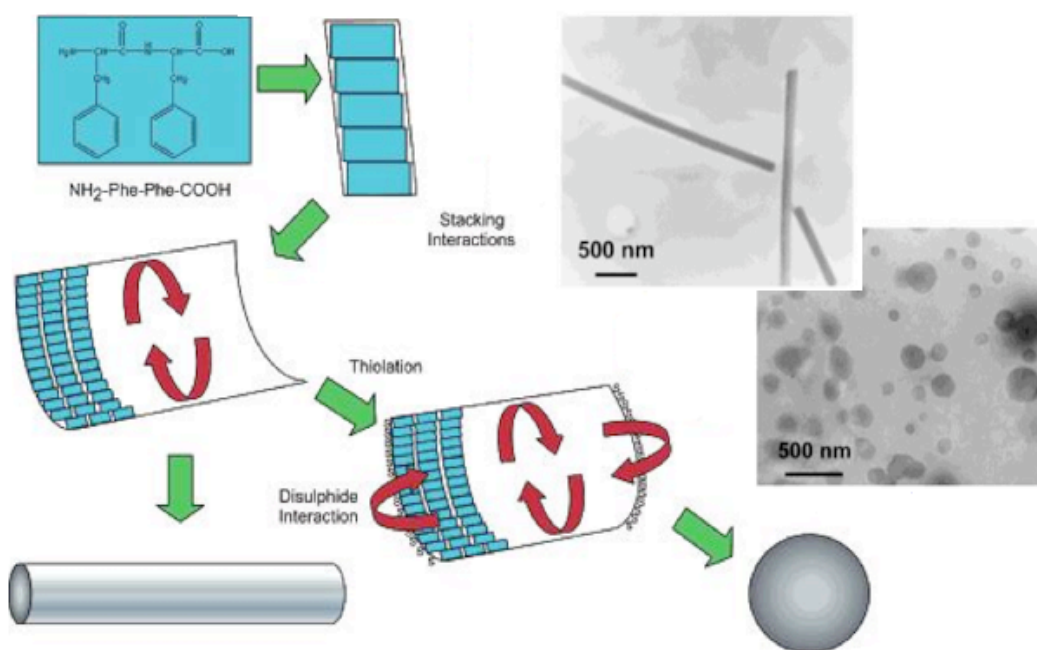
Figure 1- 10 Schematic model of closely packed spherical nanostructure formation. Chemical modification of FF peptide of changing an amine to thiol introduces formation of closed-cage nanospheres. TEM micrographs of FF nanotubes and nanospheres formed by FF peptide that self-assembled in the presence of 2-iminothilane are presented on the right [83].

1.2.3 Nanowires

A number of published works have been focused on FF-based nanowire production [76, 100, 115]. The synthesis of 1D FF nanowire can be achieved by dissolving the peptide in carbon disulfide solution, followed by 20 minutes sonication [116]. The formed nanowires exhibit liquid crystallinity with an average diameter of 346 nm and a length of 8.6 μm, and achieved rapid alignment under an external electric field (Figure 1-11a). Another study by Gazit et al. introduced ionic silver solution with the FF tube-forming solution, followed by addition of citric acid [76]. The reduced silver ions were observed to fill in the centre of FF tubes. Finally, the peptide mould was degraded by Proteinase K enzyme via proteolytic lysis. The formed silver nanowires had an average diameter of 20 nm observed by TEM, slightly narrower than the tubes as expected (Figure 1-11b). This work was further investigated by Gazit and his co-workers [115]. Recently, they reported the successful fabrication of coaxial FF nanocables: After silver-filled FF tubes were formed, a linker peptide containing the diphenylalanine motif (to enable π-π interaction with FF tube) and a cysteine residue (to provide a thiol group allowing further chemical modification) was added to bind the FF tube surface, the position of the linker was visualized by addition of gold nanoparticles which rapidly bind to the thiol group and distributed evenly on the tube surface. The binding and even distribution of the gold nanoparticles act as nucleation sites, enabling site-specific initiation of electroless deposition of metal ions over the FF tube surface, thus forming silver-FF-metal coaxial nanowires (Figure 1-11c). Moreover, Ryu and co-workers published another method of nanowire

production with vertical alignment [103]. FF peptide was dissolved in HFIP to obtain a peptide thin film (as illustrated in Figure 1-8), polyaniline vapour was used instead of water vapour to promote vertical unidirectional growth of nanorods. From SEM analysis, polyaniline was clearly coated over the FF rods. This FF-polyaniline nanowire was then used as a template for synthesis of FF/$C_{O3}O_4$ composite nanowires [100, 101]. The formed FF/cobalt oxide hydrbid nanowires exhibit high stability against thermal, chemical and proteolytic attacks, demonstrating remarkable potential for energy storage (Figure 1-11d). In addition, Song et al. synthesized FF-nanotube platinum-nanoparticle composites by simply mixing FF tube solution with K_2PtCl_4, followed by adding a reductant (ascorbic acid) solution [89]. A layer of Pt nanoparticles of 2-3 nm thickness was observed embedded in the FF tube walls under high resolution TEM (Figure 1-11e). A summary illustration of the above mentioned nanowire production approaches is presented in Figure 1-11.

a

FF NT + CS₂ →

b

sodium citrate — Proteinase K

Silver-filled nanotube → silver nanowire I ~20 nm

c

Diphenylalanine → Self-Assembly

Silver Ions

Linker Peptide

Gold Nanoparticles

Gold Ions

Formation of peptide nanotube → Reduction of silver inside the peptide nanotube → Binding of linker peptides to peptide nanotube surface → Attachment of gold nanoparticles → Reduction of gold over the peptide nanotube

d

diphenyl-alanine (Phe-Phe)

aniline vapor 100 °C

Co₃O₄ coating layer

CoCl₂ +NaBH₄ oxidation at RT

1. Formation of amorphous peptide thin film

2. Growth of peptide nanowires (PNWs)

3. Peptide/Co₃O₄ Nanocomposite

e

FF NT + K₂PtCl₄ + ascorbic acid →

600 nm

1 µm   4 nm

Figure 1- 11 Schematic illustration of different methods of FF nanowire production [76, 89, 100, 115, 116].

1.2.4 Hydrogels

Another type of nanostructure that FF peptide can self assemble into is a nanoscale-ordered hydrogel [117-120]. Compared with synthetic polymer-based hydrogels, peptide-based ones are of great interest for tissue engineering and regeneration as they are expected to be biocompatible, easy degradable by proteolysis, very simple to chemically modify and to manufacture on a large scale, more over they are cost effective as well. FF is probably one of the smallest peptides that can self-assemble to form hydrogels [106, 121]. The procedure is very simple; gels were rapidly formed when FF peptide was dissolved in HFIP, followed with chloroform or toluene dilution. The formed gel has been demonstrated to encapsulate quantum dots and gold nanoparticles at room temperature (Figure 1-12).
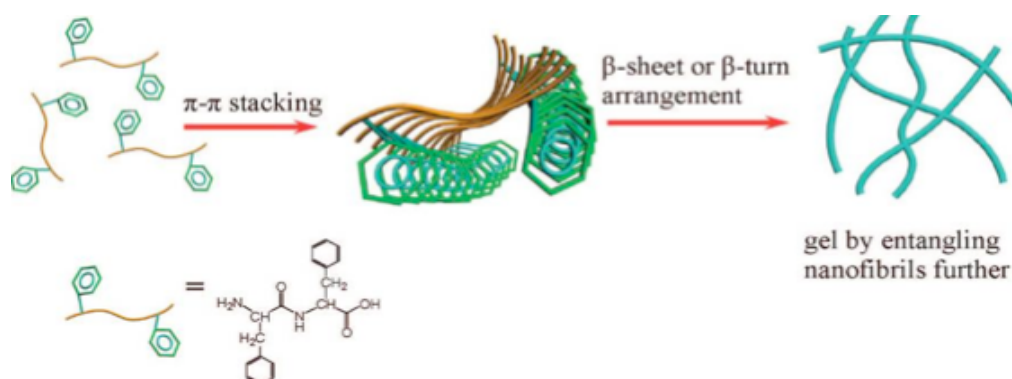
Figure 1- 12 Schematic of FF-hydrogel formation. FF peptides self-assemble via extensive π-π stacking interactions and hydrogen bonding to form nanofibrils. Such nanofibrils undergo further entanglement to form organogel [121].

Another example of FF-based hydrogel uses FF with an α, β-dehydrophenylalanine residue (ΔPhe) [122]. The residue is an unsaturated analogue of phenylalanine that induces conformational constraints in the peptide backbone and also protects the dipeptide from proteolysis. The free termini of ΔPhe-FF offers potential gelation control by modulation of electrostatic interactions via further chemical modifications. The rapidly formed hydrogel was stimuli responsive to a number of external conditions such as pH, temperature and ionic strength. Encapsulation of bioactive molecules has been demonstrated and shown remarkable sustainable release. Moreover, the biocompatibility of the hydrogel has been confirmed with a MTT assay on HeLa and L929 cells [122].

It has been demonstrated that an amine-modified analogue of FF, 9-fluorenylmethoxycarbonyl (Fmoc)-FF, self-assembles into a nanoscale hydrogel with fibril diameters ranging from 10 to 100 nm in aqueous solution with physical characteristics of a gel (Figure 1-13) [118, 123-125]. The formed hydrogel is found to have stability over a wide range of temperature, pH range, and various solutions including urea, guanidinium hydrochloride and extreme acidic conditions. Rheology analysis of the Fmoc-FF hydrogel has shown a value of a storage modulus that is greater than the value of the loss modulus by one order of magnitude, which is a characteristic of a solid-like gel [118]. An MTT assay was performed on Fmoc-FF hydrogel exposed Chinese hamster ovary cells, showing >90% cell viability confirming its potential biocompatibility and as a scaffold for tissue engineering [123].

A number of spectroscopy techniques have been applied to study the intermolecular structure of FF-based hydrogels, including circular dichroism (CD) and fourier transform infrared (FTIR) [106, 121, 126], X-ray powder diffraction (XRPD) [121, 127], and fluorescence spectroscopy [128, 129]. CD analysis showed a wavelength of Fmoc-FF at 218 nm which is consistent with that of fluorescence spectroscopy a β–sheet structure; FTIR spectrum of Fmoc-FF showed two characteristic peaks of amide I band at 1630 and 1685 cm^{-1}, which are in good agreement with an anti-parallel β–sheet structure; the XRPD pattern showed a sharp peak at 2θ of 5.2° with d spacing of 1.7 nm, which corresponds to the thickness of a β–sheet monolayer; furthermore, the fluorescence emission spectrum of Fmoc-FF was compared that of Fmoc-F, a shift of a peak from 320 to 330 nm was found, together with a new broad peak at 460 nm, which indicates the formation of excimer and higher order aggregates [118].
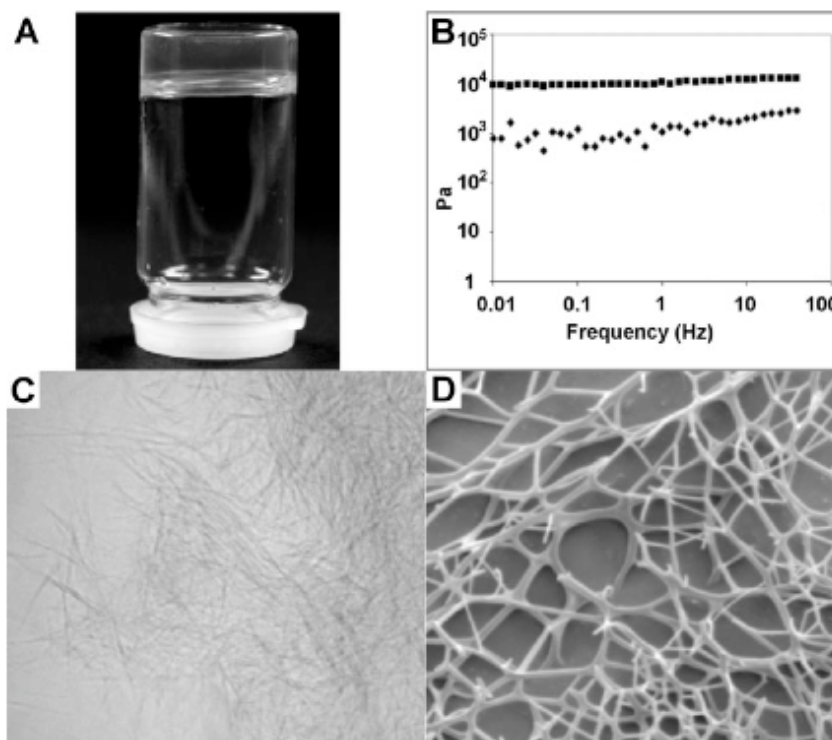
Figure 1- 13 Fmoc-FF hydrogel. The transparent, self-supporting hydrogel is presented in (a); rheology which confirms the solid-like property is shown in (b); light microscopy image of the hydrogel is presented in (c) and cryo-SEM micrograph is shown in (d) [118].

1.3 Application of diphenylalanine-based nanostructures

FF and FF-based self-assembling nanostructures have demonstrated a broad range of applications in both non-biological [76, 100, 103, 116, 130] and biological fields [131, 132]. Their physical strength, chemical and thermal stability have made them of great interest in novel material synthesis such as nanowires [76], nanocables [115], nanosensors [133]; their proven

biocompatibility and ease for chemical modification offers potential as biosensor [131, 132, 134] and molecular scaffolds for tissue engineering [119, 135-138]. The application of FF-based nanostructures in both nano-device fabrication and biological field will be summarized in following sections.

1.3.1 Application for nano-device fabrication

As mentioned earlier, FF is known as one of the shortest yet stiffest biological building block. The self-assembled nanotube presents remarkable physical and chemical characteristics which enable their applications in novel material synthesis, such as conductive nanowires [76], peptide-polymer coaxial nanocomposite [89, 100, 101], and nanocables [115]. A summary of current applications in nano-device fabrication is presented in Table 1.2.

Table 1. 2 Summary of diphenylalanine nanostructures reported in the literature.

Application	Description	Reference
FF nanorods	FF tube solution was mixed with CS_2 to form conductive FF nanorods.	[116]
Silver nanowire	FF tube solution was mixed with ionic silver solution, followed by adding sodium citrate and Proteinase K enzyme.	[76]
Silver-filled FF nanowire with metal ion tube surface decoration	FF tube solution was mixed with ionic silver solution. A linker peptide solution was added followed by addition of gold ions	[115]
FF-polyaniline nanowire	FF thin film was formed by dissolving FF peptide in HFIP without water dilution; vertical growth of Fr-based nanowire was formed by aniline vapour exposure at high temperature.	[103]
FF/polyaniline-cobalt oxide hydrbid nanocomposite	FF/polyaniline-cobalt oxide hydrbid nanocomposite was formed by C_OCl_2 and $NaBH_4$ exposure to FF-polyaniline nanowire at room temperature.	[100]
FF nanotube platinum nanoparticle composites	FF nanotube solution was added with K_2PtCl_4 and ascorbic acid	[89]

1.3.2 Application in drug delivery and tissue engineering

A number of studies have been focused on the potential applications of FF-based nanostructures in the biological field. For example, FF and FF analogue-formed hydrogels have proven ability to encapsulate nanocrystals and bioactive materials [120, 121, 126, 139]. The release of such bioactive material shows sustainable manner. The self-assembled hydrogels are easy to fabricate by a variety of methods and support cell growth of various cell lines [140, 141]. Furthermore, some of these hydrogels are responsive to enzyme and other stimuli, such as temperature and light [122]. Therefore enzymes can be used to control the formation of hydrogels, which normally take place *in vivo*; in other words, target-specific hydrogel formation might be possible. A number of natural enzymes, including thermolysin [142], β-lactamase [143], and phosphatase [144, 145], have been applied to the enzyme-tuned self-assembly of FF-based nanostructures.

FF-based nanostructures possess potential for *in vitro* delivery of drugs and genes [146-148]. A recent study revealed a successful delivery of oligonucleotides to the interior of cells by a self-assembled FF analogue nano-carrier. The cationic analogue of FF, H-Phe-Phe-NH$_2$•HCl, self-assembles into nanotubes and nanovesicles with further dilution at physiological pH. Confocal laser scanning microscopy confirmed the stable attachment of oligonucleotides via electrostatic interactions [146].

1.4 Thesis outline

The aims of this PhD project are to investigate the self-assembly of diphenylalanine peptide utilizing a number of microscopy and spectroscopy techniques, including SEM, AFM, Raman spectroscopy, and XRPD, to study the morphology, intermolecular structure, self-assembly mechanism and other properties of FF peptide nanotubes; and to compare FF nanotubes prepared by different methods. To investigate the potential of the formed FF nanotubes as carriers for drug delivery purposes, selective drug molecules were incorporated into the FF structures and the subsequent *in vitro* drug release was performed.

The first chapter of this thesis has presented a broad background of FF-based nanostrcutures. The physicochemical properties and biological properties of these nano-assemblies were introduced, together with the current and potential applications.

The studies presented in Chapter 2 are focused on FF nanotubes. Although FF nanotubes are well studied by numerous investigations, there is no study which compares the properties of FF tubes prepared by different methods. This Chapter focuses on the characterization of FF nanotubes fabricated using two published methods. A variety of microscopy and other techniques including AFM, SEM, FIB-SEM, XRPD and Raman spectroscopy were applied. The differences in morphology of the tubes formed by different methods are discussed. This chapter concludes with a tentative suggestion of the peptide nanotube assembly pathway.

The work presented in Chapter 3 explores the biological properties of FF nanotubes. The cytotoxicity of the tubes on a HeLa cell line is investigated using a MTT assay. The tubes are manufactured by the two previous methods as described in Chapter two from a range of concentrations. The cytotoxicity is investigated after incubation with HeLa cells. Furthermore, other factors that may influence the cytotoxicity, such as the presence of HFIP and serum in cell culture medium are also explored.

The experiments presented in Chapter 4 exploit the potential of FF tube as a drug carrier for delivery applications. Based upon the results from previous chapters, the scope of the chapter focuses on the utilization of FF tube as potential drug carriers. The opening section of the chapter documents the synthesis of nanotube-drug complex using two model drugs with different solvents at different loading concentrations. Characterization of the complex is investigated with SEM. *In vitro* drug release is performed showing a notable sustained manner.

Finally, a brief summary of all the work and its implications is presented in presented in the last chapter.

Chapter 2   Characterization   of   Diphenylalanine Nanotubes

2.1 Introduction

2.1.1 Molecular self-assembly

There are numerous examples in nature where complex biological structures are formed from repeat small building blocks through spontaneous self-recognition processes on a nanoscale [149, 150]. Such processes, termed 'molecular self-assembly', play a vital role in many biological systems [151]. Self-assembly facilitates the achievement of various biological functions but can also be part of a pathogenic process. Examples of this dichotomy are the folding of polypeptide chains into useful functional proteins and the formation of amyloid fibrils that are associated with a number of diseases such as diabetes and Alzheimer's [2, 152]. Self-assembly is also a principle theme in nanotechnology, where molecular self-recognition facilitated by a combination of different non-covalent interactions between simple building blocks allows the fabrication of functional 2- and 3-dimensional structures (Figure 2-1) [153-156]. Such a so called 'bottom-up' strategy, compared with the conventional 'top-down' methods, offers several advantages including ease of production and precise control of the final assembled structure by optimizing the starting building blocks.
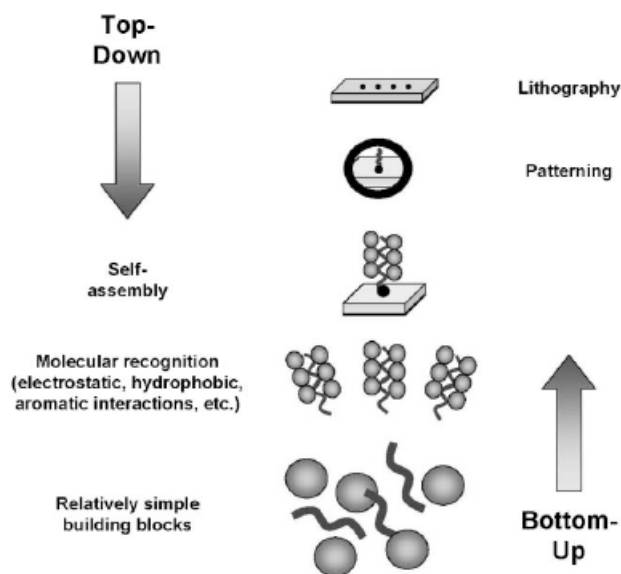
Figure 2- 1 Schematic comparison between top-down and bottom-up approaches: bottom-up approaches describe the spontaneous formation of an ordered structure from individual disordered entities under thermodynamic equilibrium condition [156].

2.1.2 Diphenylalanine self-assembly

Biological-based building blocks in self-assembly processes are favoured by researchers due to their potential biocompatibility and their ability for specific molecular recognition over non-biological systems [157-160]. Since the discovery of the role of FF in the formation of amyloid fibrils, there has been rapid progress in the investigation of assembled FF dipeptide [87, 161-164]. Methods of forming FF nanotubes *in vitro* have been developed. There are essentially two recognized approaches. It has been demonstrated by Gazit's group that nanotube suspensions of FF can be rapidly obtained by dissolving FF peptide in an organic solvent, 1,1,1,3,3,3- hexafluoropropan-2-ol (HFIP), followed by dilution with water [76]. Another group led by Song have reported

an alternative method for preparing FF nanotubes omitting HFIP; FF peptide was heated at 65 °C in water for thirty minutes and the solution was then cooled to room temperature [89].

Over the past decade, applications of FF nanotubes have been widely spread over the field of nanotechnology. Studies have shown their utility as novel materials in nanoelectronics; for example, to act as scaffolds for nanowire [76], nanocomposite [89, 100, 101], and nanocable production [115], and as electrochemical biosensor platforms [131]. The applications of FF tubes in biological and pharmaceutical areas have been broadened by chemical modification of the FF peptide to form specific functionalized nanomaterials. For instance, by attaching the amino-terminal of FF with a fluorenylmethyloxycarbonyl (Fmoc) group, the derivatives have been shown to be capable of forming scaffolds for drug encapsulation and controlled release, and for supporting 2D and 3D cell culture proliferation [118, 124, 136, 141, 145].

2.1.3 Objectives of this chapter

The experiments within this chapter focus on the investigation of the physical properties of the FF nanotubes prepared by two different methods as previously described. The nanotube preparations were carried at the same peptide concentrations to investigate potential differences in morphology of the tubes formed. Knowledge of how FF nanotube self-assemble and the mechanism of fibril growth is important to understand their potential use; modification of the

tube size and other physical properties such as rigidity offer chances to broaden the scope of applications. For example the size of the tube is crucial when evaluating its potential as a drug carrier. A valid and reproducible method to produce homogenously sized tubes would be advantageous.

2.2 Experimental

2.2.1 Materials

FF peptide and 1,1,1,3,3,3- hexafluoro-2-propanol (HFIP) were purchased from Sigma-Aldrich, UK.

2.2.2 Method

2.2.2.1 Nanotubes prepared in HFIP/water mixture

Fresh stock solutions were prepared by dissolving the lyophilized peptide in HFIP at a concentration of 100 mg/mL. The peptide stock solution was subsequently diluted in double distilled water (ddH$_2$O, pH 6.5, resistivity 18.2 MΩcm) to a final concentration of 1 mg/mL and vortex mixed for 30 seconds.

2.2.2.2 Nanotubes prepared in water alone

Lyophilized FF peptide was dissolved in ddH2O (1mg/mL) at 65 °C. After a 30 minute equilibration at 65 °C, solutions were allowed to cool to room temperature.

2.2.2.3 Sample characterization

2.2.2.3.1 Atomic force microscopy imaging

Aliquots (20 μl) of freshly prepared FF nanotube suspensions (as prepared by the methods stated above) were placed onto freshly cleaved mica substrates (Agar Scientific Ltd., Stansted, UK), and gently dried in a stream of nitrogen gas. Topographic and phase images of the sample were generated using a D3000 AFM (Bruker Nano/Bruker AXS, Santa Barbara, CA) with a J-type scanner. All imaging was performed in air in tapping mode using silicon TESP cantilevers (Veeco Metrology Group) with a nominal spring constant of 42 N/m. The scan rates employed ranged from 1.0 - 2.0 Hz. Data was analyzed using Scanning Probe Image Processor (Image Metrology A/S, Denmark). Corresponding topography and cross-sectional analysis data are presented alongside images where appropriate.

2.2.2.3.2 Scanning electron microscopy imaging

Nanotube samples were dried on mica substrates following the same procedure as in the AFM sample preparation. The mica substrates were then mounted onto 12 mm aluminium sample stubs (Agar Scientific Ltd.) using carbon tabs (12mm diameter, Agar Scientific Ltd.) The samples were deposited with a thin layer of gold by low-vacuum sputter coating to facilitate imaging (argon gas with an ion current of 30 mA). SEM images were recorded using a JSM JEOL 6060 SEM (JEOL, Tokyo, Japan) operating at 10 kV. The size of the tubes was measured using SM-35080 SMILE VIEW software.

2.2.2.3.3 Focused ion beam-scanning electron microscopy imaging

Aliquots (20 μl) of freshly prepared FF nanotube suspensions were placed onto 12 mm aluminium sample stubs (Agar Scientific Ltd.) and then allowed to dry at room temperature. The stub was then coated with carbon using a turbo carbon coater (Agar Scientific Ltd.) The images were collected at low electrical voltage to minimize the over charge of the sample. The milling process was undertaken by an ion beam current of 0.3 – 0.5 nA at a voltage of 30 kV.

2.2.2.4 X-ray powder diffraction

XRPD measurements were recorded on a Bruker D8 (Bruker, Coventry, UK). Powders were loaded into glass capillaries (0.7 mm, Capillary Tube Supplies Ltd.). Data were collected in step scan mode between 2.0° and 90° (2θ) with a step size of 1° and a counting time of 10 s/step. The working conditions were 10 kV and 30 mA. All peak positions were used for the determination of micro structural parameters.

2.2.2.5 Raman spectroscopy

Aliquots (20 μl) of freshly prepared FF nanotube suspensions were placed onto freshly cleaved mica substrates (Agar Scientific Ltd.), and gently dried in a stream of nitrogen gas. Spectra were recorded on a home-constructed Raman micro-spectrometer consisting of major components such as laser (785 nm, Photonica), microscope (Olympus), Spectrometer and CCD (Andor). Other

optics components included are microscope stage, lenses, plasma and Rayleigh filters (Prior Systems, Thorlabs, Newport and Semrock, respectively). The instrument was operated using a program developed in-house in Labview (National Instruments) which controlled the microscope stage, the spectrometer and the CCD camera. The beam path was 800 mm.

2.3 Results

2.3.1 Characterization

2.3.1.1 AFM imaging

Samples of the nanotubes formed by FF peptide were imaged by AFM using tapping mode imaging in air. The images shown in Figure 2-2 and Figure 2-3 are representative AFM images of the dried FF nanotube samples formed in HFIP/water mixture and water alone, respectively. The range of diameters of the nanotubes observed is in agreement with previous work (from few nanometers to 2μm) [76, 78, 79, 92, 93]. AFM characterization of FF nanotubes was repeated on several tens of samples and the data showed good reproducibility.

The AFM images presented in Figure 2-2 were taken from dried FF nanotube sample prepared by HFIP/water mixture. Figure 2-2a is a topography image of a selected nanotube displaying long, discrete and unbranched morphology with a slight bend along the tube. A 3D representation of the nanotube is presented in Figure 2.2b demonstrating the tubular nature of the structure. The selected

nanotube shows parameters in terms of height and half-height widths consistent with published values (Figure 2.2c) [80, 84, 93, 121].

The AFM images shown in Figure 2-3 represent a selection of tubes formed in water alone. The 3D representation is presented in Figure 2-3b presenting long, straight, unbranched and tubular nature of the tubes. A profile of the nanotube cross-section (location is highlighted by the line in Figure 2-3a) is presented in Figure 2-3c showing data in agreement with published AFM measurement of FF tubes [80, 84, 93, 121].
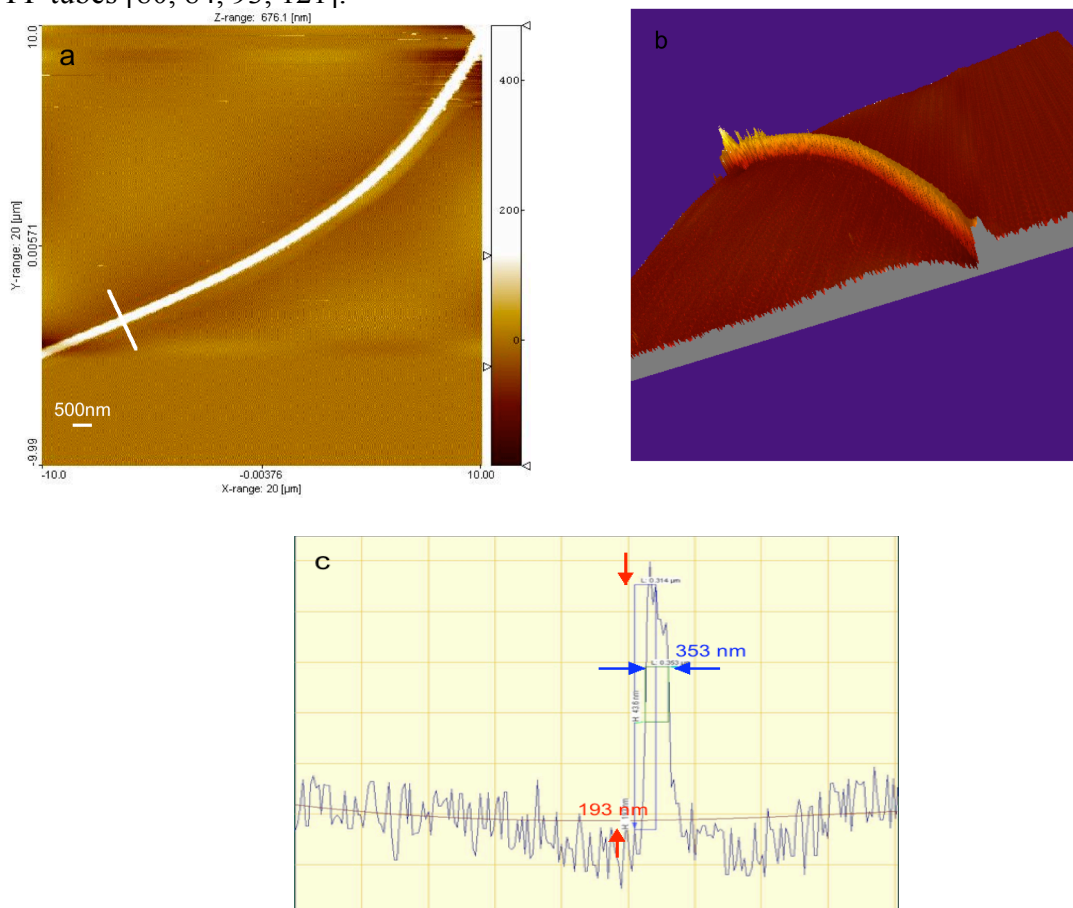
Figure 2- 2 AFM images of a FF nanotube formed in HFIP/water mixture. Figure 2-2a is a topography image of the FF nanotube dried onto freshly cleaved mica substrate and imaged by tapping mode AFM in air. Figure 2-2b is a 3D representation and Figure 2-2c is a cross-sectional profile of the nanotube (location is highlighted by the line in Figure 2-2a).
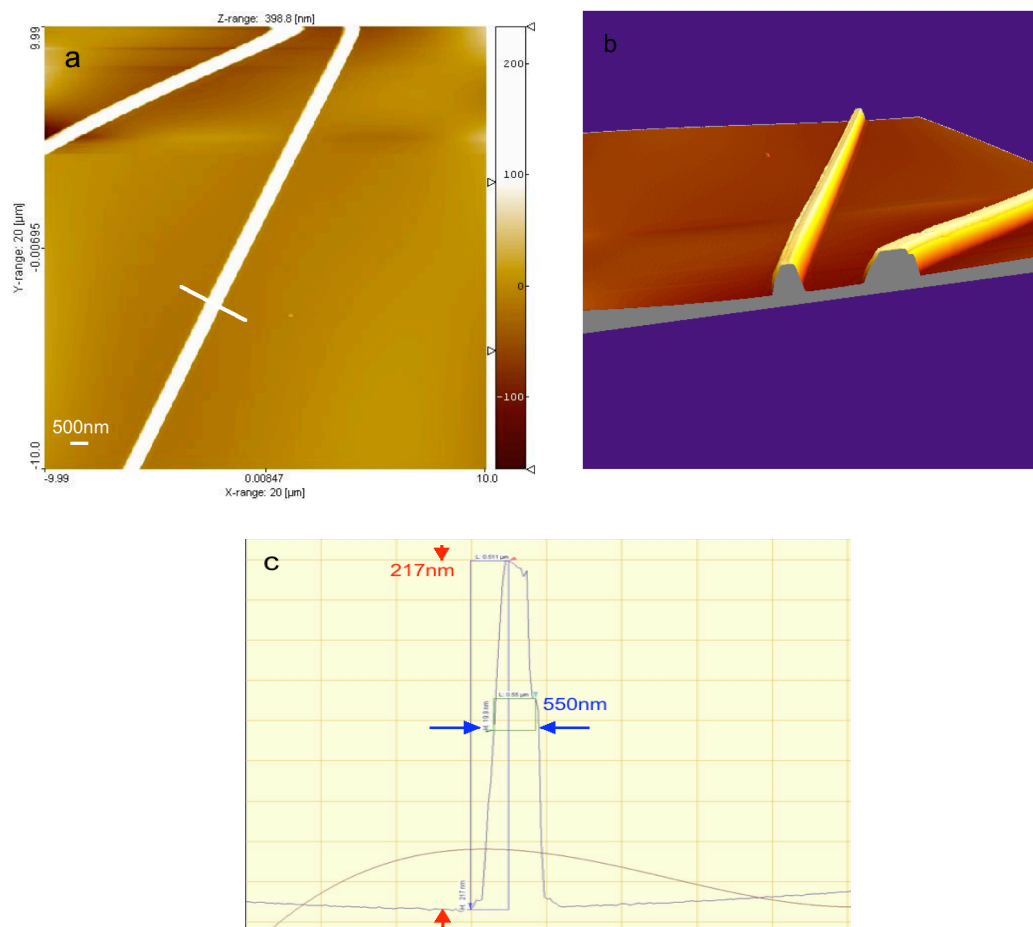
Figure 2- 3 AFM images of FF nanotubes formed in water alone. Figure 2-3a is a topography image of the FF nanotubes dried onto freshly cleaved mica substrate and imaged by tapping mode AFM in air. Figure 2-3b is a 3D representation and Figure 2-3c is a cross-sectional profile of the nanotube on the left (location is highlighted by the line in Figure 2-3a).

2.3.1.2 SEM imaging

Dried samples of FF nanotubes prepared by both methods were imaged by SEM under vacuum with the same experimental parameters (electrical voltage = 10kV, working distance from the lens to the sample = 30mm, and spot size = 40mm).

2.3.1.2.1 SEM imaging of FF nanotubes formed in HFIP/water mixture

Figure 2-4 presents a low resolution SEM image of a nanotube sample prepared in HFIP/water mixture. The nanotubes are closely associated with each other with lengths up to hundreds of microns; different areas of the sample are shown at higher resolution from Figures 2-5 to 2-8. Compared with published SEM studies on FF nanotubes that display long, straight and unbranched morphology, the results presented here show some interesting differences, which will be addressed below [79]. A size distribution of FF nanotubes was made based on a large number of samples (n>1000) and is presented in section 2.3.1.4.

The SEM image presented in Figure 2-4 is a typical overview of the dried FF nanotube samples. The images in Figure 2-5 are selections of the nanotube samples viewed at a higher resolution (magnification ranges from x1700 to x6000). The bundles of nanotubes presented in Figure 2-5a display 'crystal-like' features: there is a repeating pattern of the tubes originating from a common nucleating centre and projecting outwards. The nucleation points are shown at higher resolution in Figure 2-5b and Figure 2-5c (as annotated by the arrows).
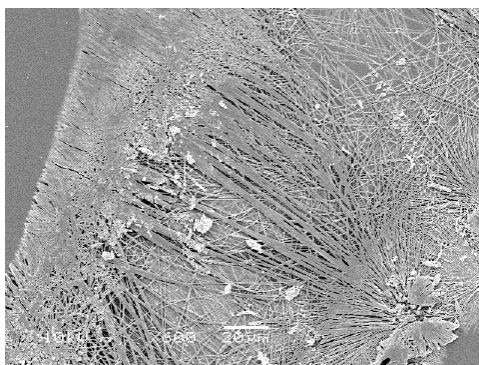
Figure 2- 4 SEM micrograph of FF nanotubes prepared in a HFIP/water mixture dried onto freshly cleaved mica coated with gold and imaged by SEM in vacuum.
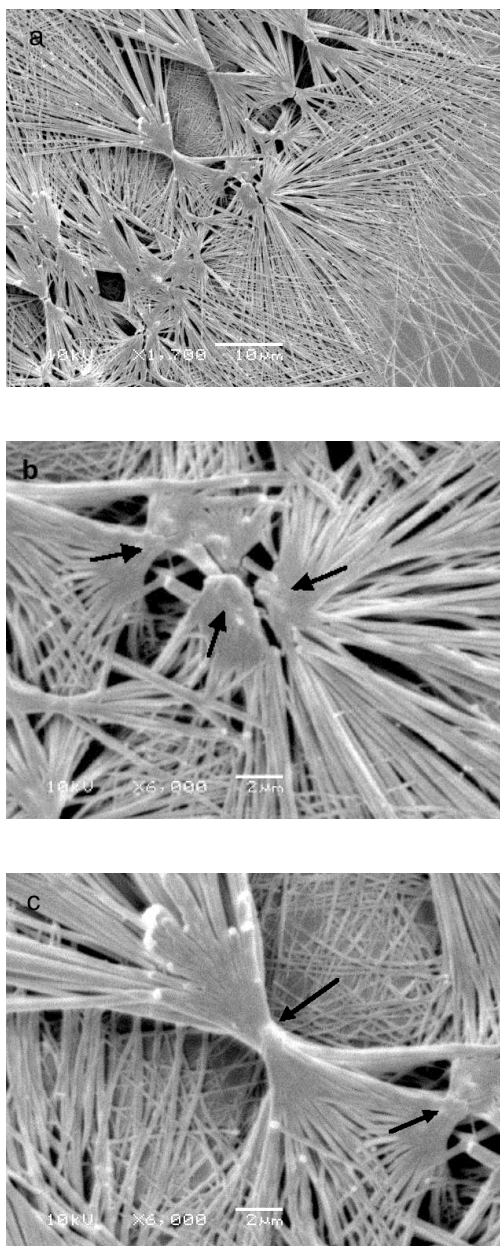
Figure 2- 5 SEM micrographs of FF nanotubes displaying nucleation points. Figure 2-5a is a SEM image of nanotubes prepared in HFIP/water mixture dried onto freshly cleaved mica coated with gold and imaged by SEM in vacuum. The origins of tubes are shown by arrow in Figure 2-5b and Figure 2-5c at a higher resolution (magnification x6000).

The SEM images presented in Figure 2-6 are different areas of the dried nanotube samples. The diameters of the tubes are up to 2 μm and lengths are hundreds of microns, which are consistent with previous studies [79]. A selection of the straight portions and curved portion of the tubes from Figure 2-6a (as highlighted by the black rectangle and the white rectangle, respectively) are presented at a higher magnification (x5500 and x2700, respectively) in Figure 2-6b and Figure 2-6c.
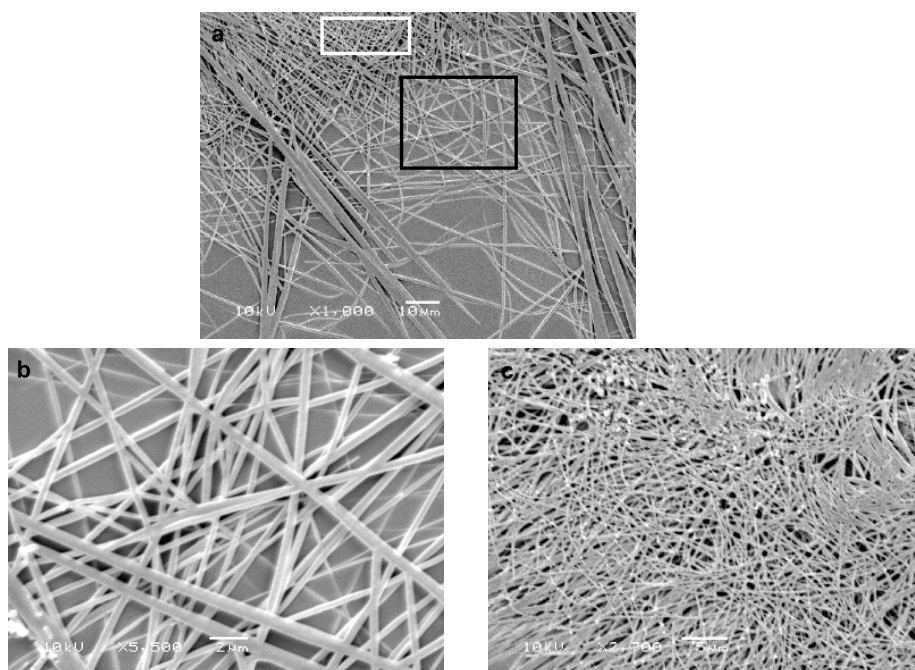
Figure 2- 6 SEM micrographs of FF nanotubes. Figure 2-6a is a SEM image of nanotubes prepared in HFIP/water mixture. A high magnification of the straight portion of the nanotubes (as highlighted by the black rectangle in a) is shown in Figure 2-6b, and that of the curved portion of the nanotubes (as highlighted by the white rectangle in a) is shown in Figure 2-6c.

The ends of the tubes originating from common nucleating centres are displayed in SEM images shown in Figure 2-7. Unlike common rigid and straight tubular ends, the morphologies of the tube ending prepared in HFIP/water mixture show variation: some exhibit a certain degree of flexibility, presenting a 'feather-like' morphology (Figure 2-7a) and some have merged with the substrate surface (Figure 2-7b).
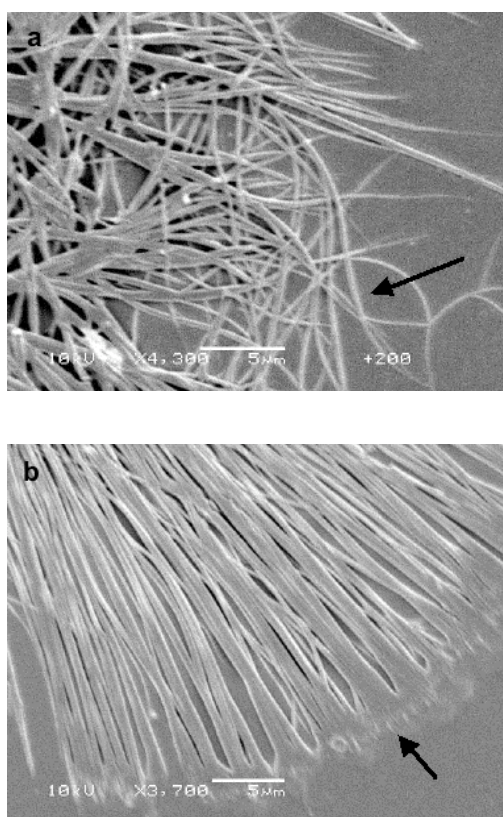
Figure 2- 7 SEM micrographs of FF nanotubes with ends with various features. Tubes were prepared in a HFIP/water mixture dried onto freshly cleaved mica coated with gold and imaged by SEM in vacuum. Figure 2-7a is a selection of the flexible ends of the tubes and Figure 2-7b is a selection of the tube ends merged with substrate surface (as indicated by the arrows).

Furthermore, a number of small structures and round objects were also seen in the samples (Figure 2-8). As shown in Figure 2-8a, a large number of small structures with lengths in the range of less than 5 μm to 20 μm are presented alongside the tube bundles. A high-resolution image (magnification x4000) is shown in Figure 2-8b. These needle-shaped structures are relatively large at one end and pointed on the other end, and can branch out (Figure 2-8c, highlighted by the arrows). There are also a number small round objects with diameters less than 10 μm seen in the nanotube samples, an example of which is shown in Figure 2-8d.
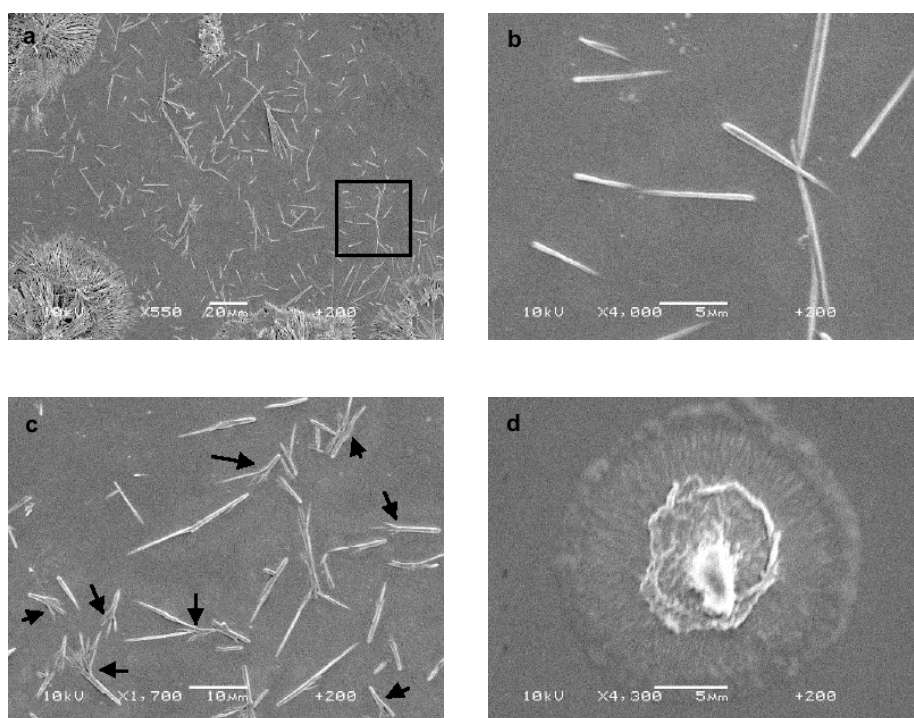
Figure 2- 8 SEM micrographs of short FF nanotubes. Figure 2-8a is a SEM image of nanotubes prepared in HFIP/water mixture dried onto freshly cleaved mica coated with gold and imaged by SEM in vacuum. A high resolution of the short, needle-like objects presented in Figure 2-8a (as highlighted by the rectangle) is shown in Figure 2-8b with a magnification x4000. The branching-out features were observed in Figure 2-8c (as indicated the arrows). Small round objects were also observed (Figure 2-8d).

2.3.1.2.2 SEM imaging of FF nanotubes formed in water alone

SEM images of the nanotube samples prepared by the aqueous method are presented in Figure 2-9 and Figure 2-10. The tubes have a similar morphology to that observed previously [79, 89]. Long, unbranched, and discrete tubular nanostructures are seen. A size distribution of FF nanotubes was made based on a large number of samples and is presented in section 2.3.1.4.

Figure 2-9 is a typical SEM image of the FF nanotubes prepared in water alone. In contrast to the images presented in Figures 2-4 to 2-8 (nanotubes formed in HFIP/water mixture), the image shown in Figure 2-9a presents well-formed nanotubes that are loosely distributed on the substrate. The distribution appears random, with the nanotubes not associated with each other, and no 'origins' of growth. A higher-resolution image of the tubes (as highlighted by the rectangle in Figure 2-9a) is presented in Figure 2-9b, displays a range of tubular diameters up to a few microns and lengths up to hundreds of microns. These values are in agreement with previous published data by Song's group in which they stated the FF tubes prepared by their procedure had a diameter that ranged from 100 nm to 2 μm and an exceeded length of 100 μm [89].

In addition, the ends of some of the FF tubes were observed to be hollow (Figure 2-10). Figure 2-10a is an SEM image of the tubes, where a tube with a hollow end is presented (highlighted by the rectangle). Under higher magnification, as presented in Figure 2-10b, the tube has a diameter around 20 μm and appear to be made up of bundles of tubes of smaller dimensions (~ 1

μm); the small tubes stack together and arrange themselves into a bigger tube with a hollow centre.
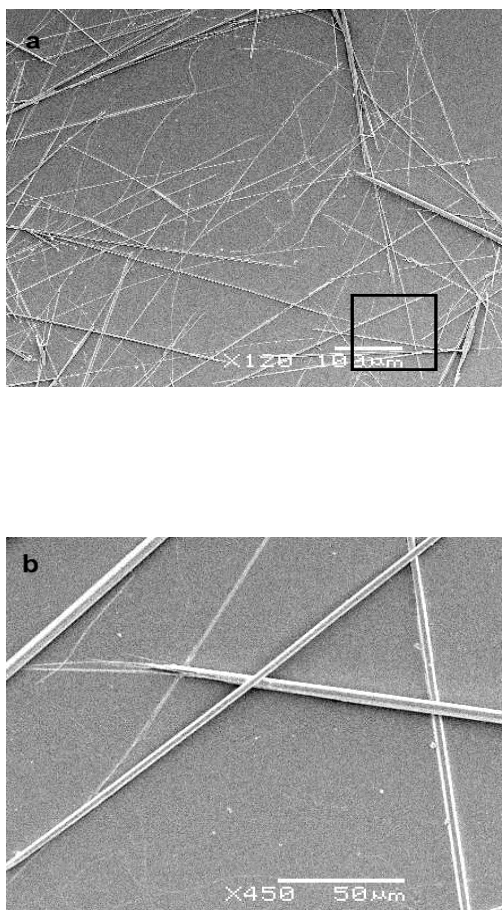
Figure 2- 9 SEM micrographs of FF nanotubes. Figure 2-9a is a SEM image of nanotubes prepared in water alone and dried onto freshly cleaved mica coated with gold and imaged by SEM in vacuum. A higher-magnification image of the rectangle highlighted in Figure 2-9a is shown in Figure 2-9b (magnification x450).
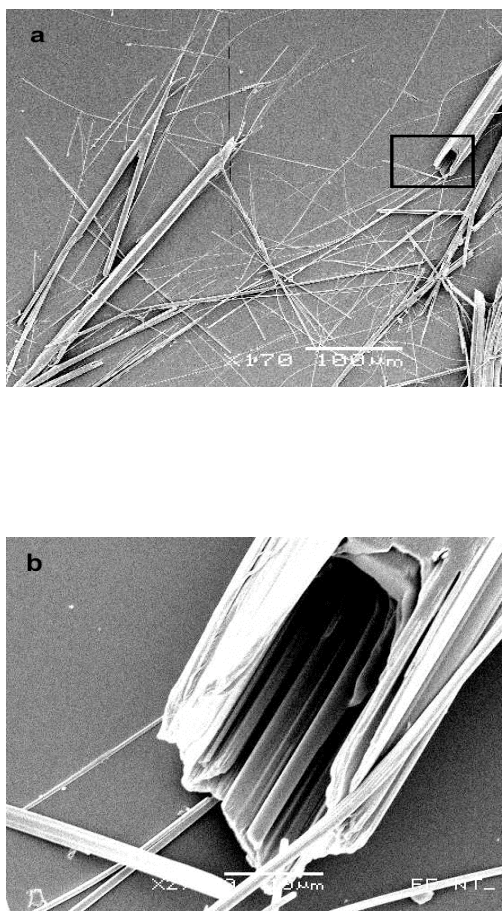
Figure 2- 10 SEM micrographs of FF nanotubes. Figure 2-10a is a SEM image of nanotubes prepared in water alone and dried onto freshly cleaved mica coated with gold and imaged by SEM in vacuum. A tube with a hollow end is annotated by the rectangle, and a higher-magnification image of which is presented in Figure 2-10b (magnification x2700).

2.3.1.3 Focused Ion Beam-SEM

A focused ion beam-SEM (FIB-SEM) study was performed on dried nanotube samples prepared using the water alone method. The aim of the experiment was to view the interior structure of the nanotubes bundles (as in Figure 2-10b)

by cross-sectional cutting the tube with a focused beam of ions at a precise position.

The FIB-SEM images presented in Figure 2-11 are of the nanotubes imaged by the primary beam of electrons at low current (5 kV). This allows SEM imaging of the sample as in standard SEM. Figure 2-11a is an overview of the FF nanotube samples dried on aluminium stub coated with carbon film. Figure 2-11b shows a bundle of nanotubes found with a diameter of around 13 μm. The position where the ion beam impacts the tube surface is indicated by the rectangle. Figure 2-11c is an end view of the bundle where a number of tubes with smaller dimensions stacking together in the direction of the bundle axis can be seen.

After localizing the position (as indicated by the rectangle in Figure 2-11b), a high voltage (30 kV) focused ion beam was applied and the milling process was induced. The ion beam impact at the tube surface generated secondary electrons and secondary ions which can be collected to generate a series of images of the milling process. The images presented in Figure 2-12 are a series taken at a time interval of seconds. As shown in Figure 2-12a to Figure 2-12d, the beam was scanned across the bundle surface which gradually cut a cross-section area. A higher-resolution view of the cross-sectional area of the tube bundle is presented in Figure 2-12e. The tube displays a hollow core with a diameter of about 1 μm. There are also smaller holes that might be the core of the smaller tubes stacked together, the axes of which run parallel to the direction of the bundle axis.
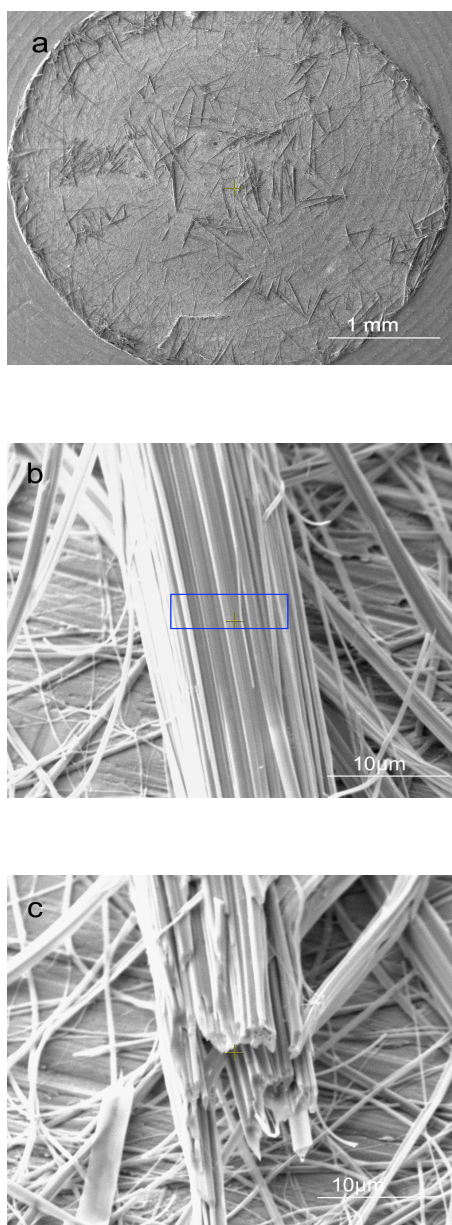
Figure 2- 11 FIB-SEM micrographs of FF nanotubes. Figure 2-11a is a SEM image of nanotubes prepared in water alone and dried onto aluminium stub coated with carbon film. The tube bundle with rectangle annotated is where the ion beam was applied (Figure 2-11b). Figure 2-11c is the end view of the tube bundle.
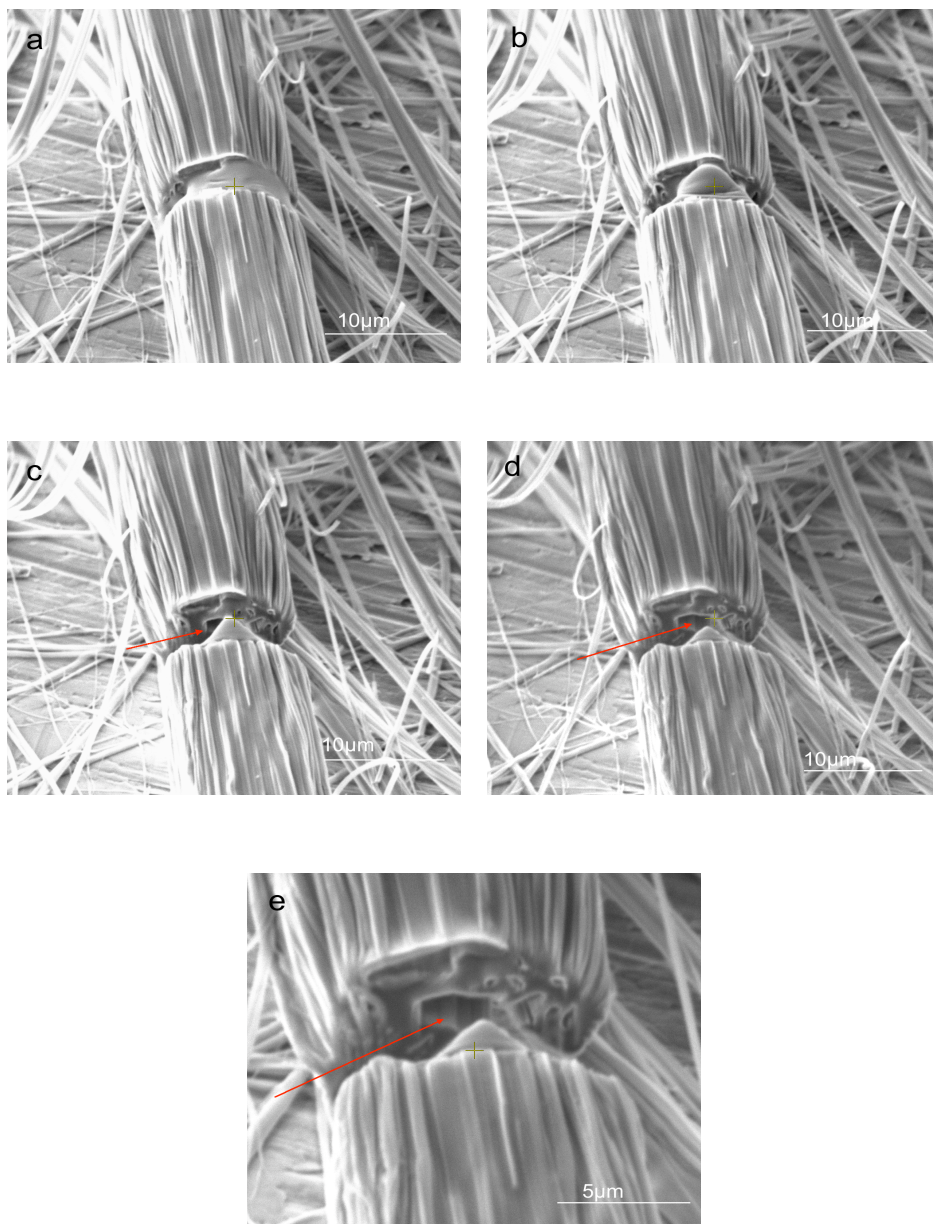
Figure 2- 12 FIB-SEM micrographs of FF nanotubes. Images presented in Figure 2-12a to Figure 2-12d are images of the milling process captured at second time intervals. A higher-resolution of the cut cross sectional area is presented in Figure 2-12e. The hollow centre can be seen (as indicated by the arrow) with small holes running parallel to the direction of the tubular axis.

2.3.1.4 Size measurement of FF nanotubes prepared by both methods

Size distributions of the nanotubes were determined for both methods of preparation based on the SEM data; length and width measurements were taken using SM-35080 SMILE VIEW software.

A representation of the length measurement of the nanotube samples prepared by both methods is displayed in Figure 2-13. Figure 2-13a is an SEM image of nanotube samples prepared in HFIP/water mixture. As seen previously these tubes are nucleated from a common origin and projecting outwards. The lengths of the tubes was determined by drawing a line from one end of the tube to the other end using the SMILE VIEW software (as indicated by the double arrowed line), and the length is automatically recorded (length = 92 μm of the tube presented in Figure 2-13a). Figure 2-13b is an SEM image of a nanotube sample prepared in water alone. Similar to previous SEM results, this method produced long, straight, and unbranched nanotubes. The length of the selected tube is 157 μm. Based on a large number of measurements (n > 1000) of tubes prepared by both methods, a length distribution is plotted in Figure 2-13c. The 'HFIP/water method' produces nanotubes with relatively shorter length, ranging from the nanoscale to > 300μm, with 54 % (n = 1108) in the range up to 50 μm. The 'water-alone method', on the other hand, gives a wider distribution; the tube length is up > 1400 μm, with 24% (n = 650) in the range up to 50 μm.

A representation of the width measurement of the nanotube samples prepared by both methods is presented in Figure 2-14. The width measurement of a tube

was undertaken by drawing a line from one side of the tube to the other using the software (as indicated by the line), with the width being automatically recorded. As shown in Figure 2-14a and Figure 2-14b, the selected tubes formed in HFIP/water mixture and the ones in water alone have diameters of 680 nm, 1200 nm and 1600 nm, respectively. A width distribution is presented in Figure 2-14c. The width distribution of the tubes formed in HFIP/water mixture ranged up to 2240 nm, with 40% between 200 nm and 300 nm. The tubes prepared in water alone, in contrast, were wider with widths up to 3620 nm, with 9% in the range of 600-700 nm. This result is consistent with previous studies which have also confirmed the water-alone procedure produced FF tube with wider dimensions than the ones produced by HFIP/water mixture [76, 89]. This is in good correlation with the AFM study; the half-height widths of the tubes prepared in the HFIP/water mixture and the water alone are 348 nm (± 9 nm) and 606 nm (± 13 nm), respectively (data presented as mean ± SEM, n = 27), which is in good agreement with the SEM data presented earlier.
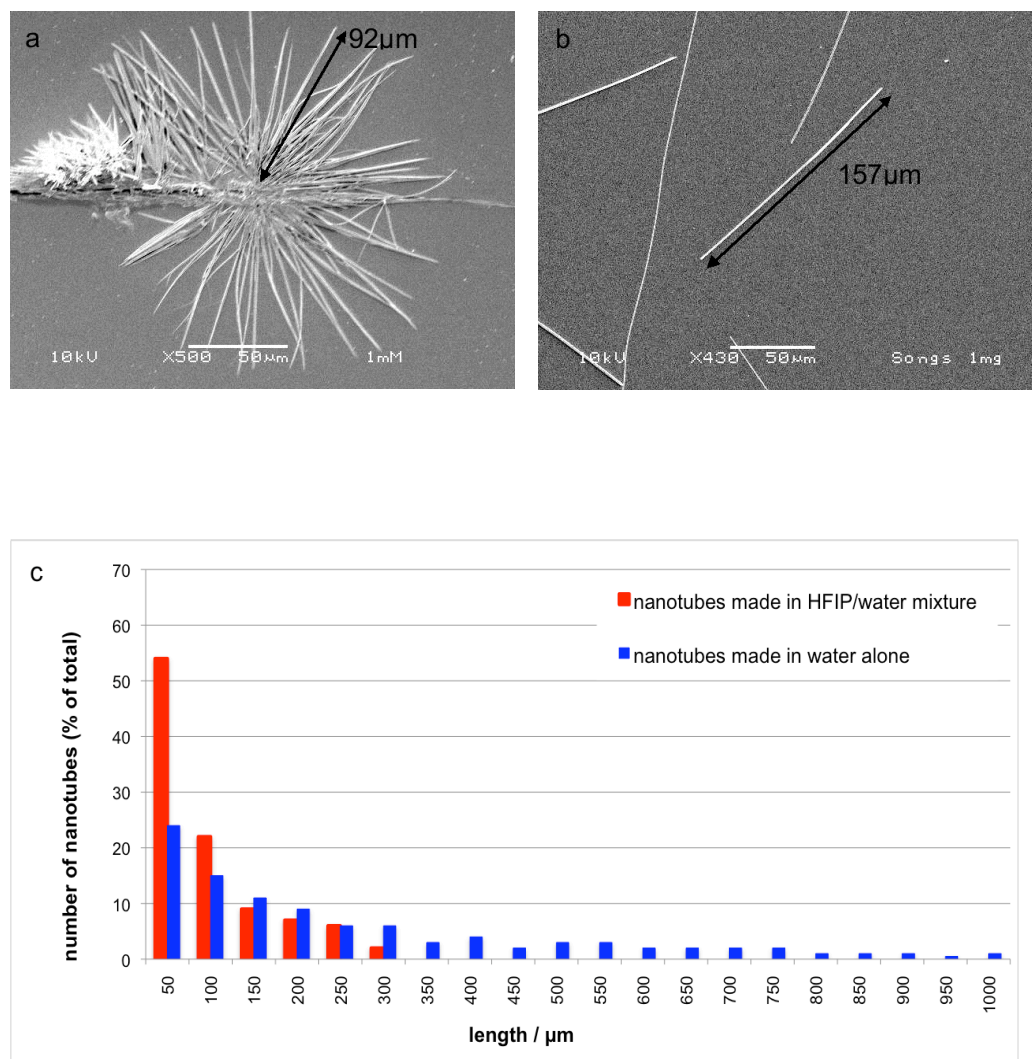
Figure 2- 13 Length measurement of FF nanotubes prepared by two methods. Figure 2-13a and Figure 2-13b are example SEM images of the tube samples formed in HFIP/water mixture and water alone, respectively. The double arrowed lines indicate the length measurement of the tubes. A distribution plots of FF nanotube (n > 1000) prepared in HFIP/water mixture (shown in red), and in water alone (shown in blue) is presented in Figure 2-13c.
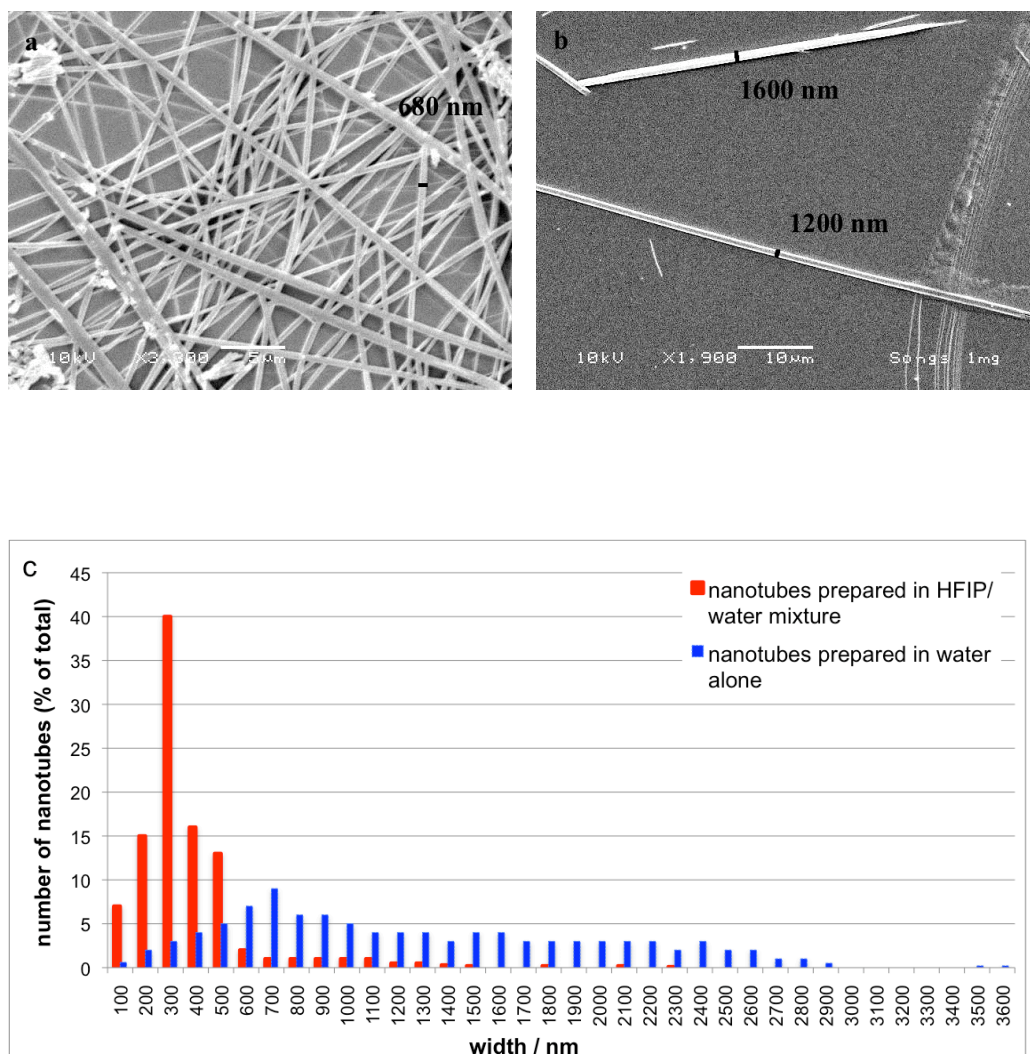
Figure 2- 14 Width measurement of FF nanotubes prepared by two methods. Figure 2-14a and Figure 2-14b are example SEM images of the tube samples formed in HFIP/water mixture and water alone, respectively. The lines indicate the width measurement of the tubes. A distribution plot of FF nanotube (n > 1000) prepared in HFIP/water mixture (shown in red), and in water alone (shown in blue) is presented in Figure 2-14c.

2.3.2 Raman Spectroscopy

Raman spectroscopy was performed on dried nanotube samples prepared by the two approaches. The advantage of the Raman spectroscopy in characterization over the microscopy techniques such as AFM or SEM is that the data has chemical and physical state sensitivity [85]. The chemical structure of FF is shown in Figure 2-15. The fingerprint region of most organic molecules is between wave numbers $500 - 2000$ cm^{-1}. The Raman spectra of the tubes formed by two methods are presented in Figure 2-16, a subtraction of the spectra is shown at the bottom. The Raman bands which can be attributed to the aromatic rings in the FF are at 1009 cm^{-1}, 1038 cm^{-1}, 1590 cm^{-1}, and 1610 cm^{-1} [85, 165]. Other characteristic bands found are at 1433 cm^{-1} and 1688 cm^{-1}, which were assigned to C-H bending within the alkyl groups and C=O stretching, respectively [85, 165]. The small peaks detected between 1100 cm^{-1} to 1300 cm^{-1} were attributed to the acyclic C-C stretching [85, 165]. The Raman band of the primary aliphatic amide bond C-N (1020 - 1090 cm^{-1}), however was not observed. A summary of the chemical groups of FF and the corresponding Raman shift values is listed in Table 2.1. The similar characteristic bands are observed from both Raman spectra of the tubes made by both methods and there is no significant difference between the two spectra.
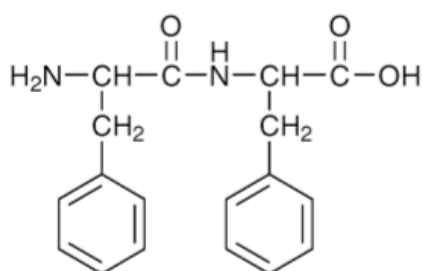
Figure 2- 15 Molecular structure of FF.
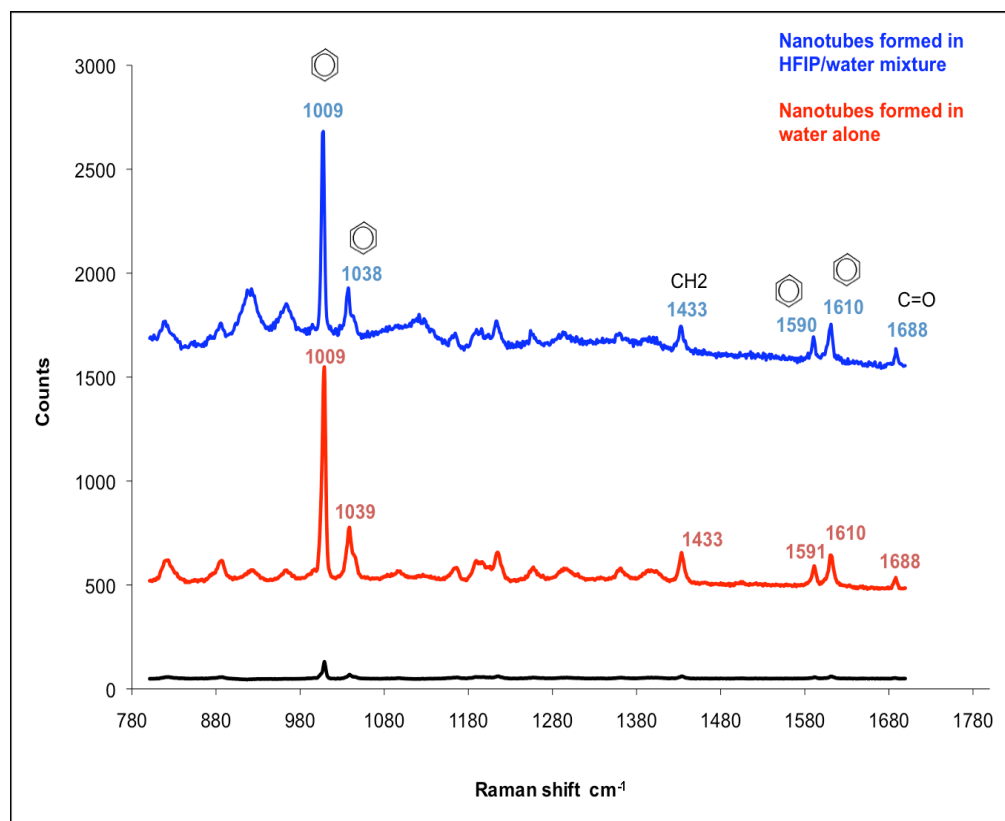
Figure 2- 16 Raman spectra of dried nanotube samples. Top blue pattern represents spectrum of the nanotube prepared in HFIP/water mixture (as shown in Figure 2-2a), middle red pattern represents spectrum of the nanotube prepared in water alone (as shown in Figure 2-3a, the one on the right), a subtraction of the spectra is shown in black at the bottom.

Table 2. 1 Chemical groups of FF and the corresponding Raman band values with relative intensities [165].

Chemical groups	Raman spectra Region/cm^{-1}	Intensity
C-N stretching (primary aliphatic amine)	1020-1090	Weak
C-C aromatic stretching	1000	Strong
	1450-1500	Medium
	1580-1600	Strong
C-C acyclic, aliphatic stretching	600-1300	Medium
CH$_2$ bending	1400-1470	Medium
C=O stretching	1680-1820	Strong

2.3.3 X-ray powder diffraction

In addition to Raman spectroscopy, X-ray powder diffraction was performed on dried nanotube samples prepared in both solvents so as to characterize, if there is any difference, in the crystal form of the nanotubes prepared by different methods.

A spectra summarizing the XRD patterns of the tubes from the two methods is displayed in Figure 2-17 and the subtraction of the two spectra is shown at the

bottom. All of the peaks are in good alignment. The subtraction of the spectra indicates that there is little/no difference observed between the two patterns.

To validate the results obtained in this experiment, a control study was performed on the prepared nanotube samples of the same batch (formed in HFIP/water mixture), and comparing the obtained experimental diffraction pattern with a simulated diffraction pattern from the database (CCDC 163340 file). As shown in Figure 2-18, the observed experimental peaks of the nanotube are in good agreement with a simulated powder diffraction pattern of the previously reported spectrum of the single crystal. This result is consistent with previous published XRPD studies on FF nanotubes [97].
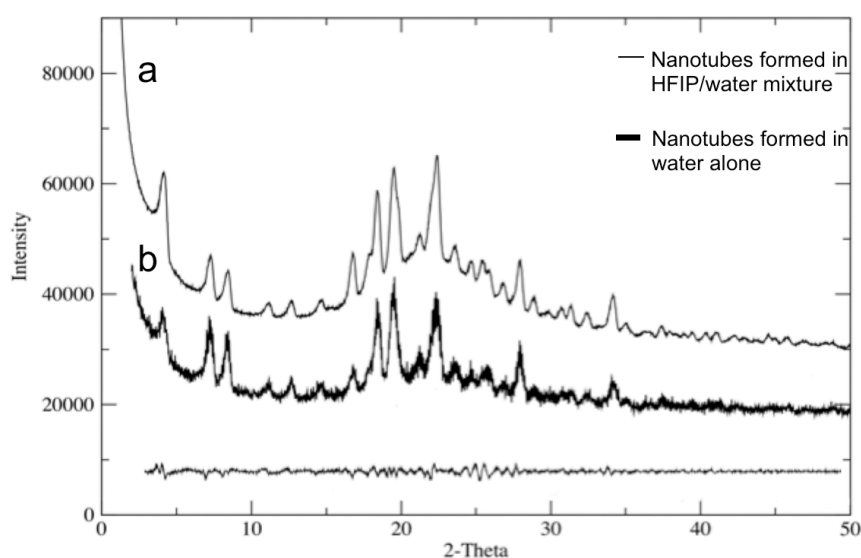
Figure 2- 17 XPRD patterns of FF nanotubes prepared (a) in water/HFIP mixture and (b) in water alone, and a subtraction of the two patterns reveals that the patterns are essentially identical.
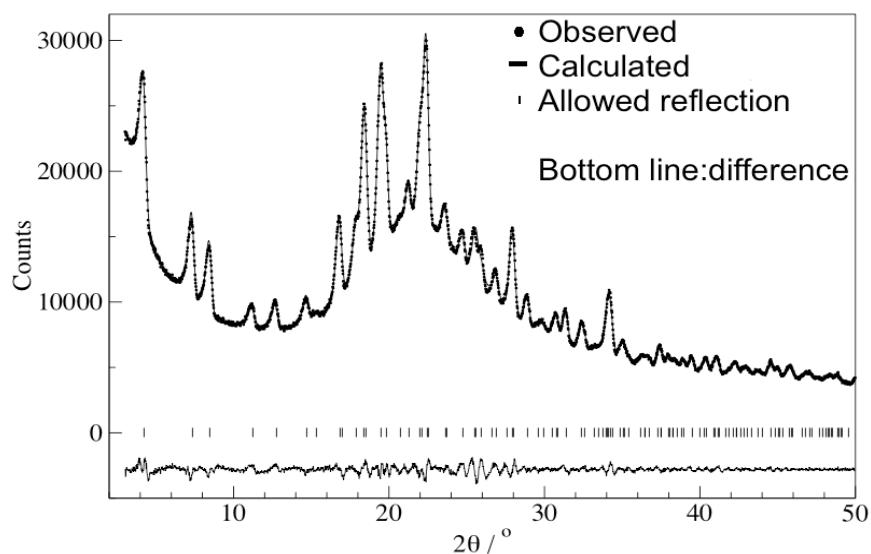
Figure 2- 18 XRPD pattern of nanotubes prepared in HFIP/water mixture. Dot marks represent the observed intensities, and the solid line defines calculated data of the single-crystal structure. Tick marks in the middle indicate the reflection positions and a difference between observed and calculated intensities is shown at the bottom.

2.4 Discussion

The SEM data presented in Figures 2-4 to 2-10 indicate that there are subtle differences in morphology and physical properties of the nanotubes prepared by the two methods. In general, the morphology of nanotubes prepared in the HFIP/water mixture presented in Figure 2-4 to 2-8 appear to have four defining features: the roots of these nanotubes are shown to be nucleated from a site of origin (Figure 2-5a and b shown by arrows) and projecting outwards (Figure 2-5c); along the tube length some tubes are long and straight (Figure 2-6a and b), whereas some other tubes show bending features stacking together (Figure 2-

6c); the ends of these tubes are quite flexible (Figure 2-7a) and some are open ended (Figure 2-7b); moreover, there are some short, needle-shaped structures that might be early stage nanotubes (Figure 2-8a and b), 'branching out' features of these short objects are seen (Figure 2-8c shown by the arrows), and small structures that might represent a precursor structure (Figure 2-8d). In contrast, the tubes prepared in water alone were discrete with no apparent nucleation points or tube-tube association (Figure 2-9). They display long, straight, and unbranched morphology similar to previous work on FF nanotubes [76, 89].

This difference in tube dimension was evaluated by size distribution undertaken from SEM data (Figure 2-13 and 2-14). These results show good correlation to AFM analysis. These studies have confirmed the physical property difference of the tubes made by different methods.

Furthermore, large bundles of nanotubes were observed in tubes from the water alone method of preparation (Figure 2-10). As can be seen from the high-resolution SEM image presented in Figure 2-10b, these aggregates are made up of smaller tubes stacking together to give the final tubular structure. This was confirmed by the interior cross-sectional morphology view from the FIB-SEM study (Figures 2-11 and 2-12). The large tube was indeed hollow from its cross-sectional view, with small holes that appear to be the cores of the smaller tubes running parallel to the direction of the tube axis. This finding is in agreement with previous studies which suggested that there are parallel channels running in the direction of the tube axis of some large FF nanotubes [89, 98].

In order to understand the observed differences in morphology of the FF tubes prepared by the two methods, knowledge of the formation mechanism is required. To date, there has been no clear elucidation of the mechanism underlying FF nanotube self-assembly, however, similar work has been undertaken on β-amyloid (Aβ) [95, 166-168]. *In vitro* studies have suggested that Aβ fibrillogenesis occurs in two distinct stages, nucleation and elongation of fibrils (Figure 2-19). The nucleation stage involves a series of energetically unfavoured steps where soluble protein monomers form stable nuclei; then elongation proceeds in which the nucleus rapidly grows to form larger fibrils [166]. The characteristic features of such a nucleation-dependent formation pathway are that no nucleation occurs at a protein concentration below a critical concentration; elongation of the fibrils stops when soluble protein monomers are exhausted. The length of the fibrils is inversely proportional to the total number of nuclei and that the elongation process follows first order kinetics, i.e. the monomers bind to the tip of the fibril at a rate that is proportional to the monomer concentration [166] This rate constant varies with conditions such as pH, temperature, and ionic strength [166]. Although there is no direct evidence proving the mechanism of FF nanotube formation is similar to that of Aβ fibrillogenesis, nevertheless FF which is the core recognition motif of Aβ and undoubtedly plays a vital role in Aβ fibril formation, furthermore the type of interactions responsible for and stabilize Aβ formation and FF nanotube formation are similar. There could be similarities in the underlying mechanism of formation between the two models.
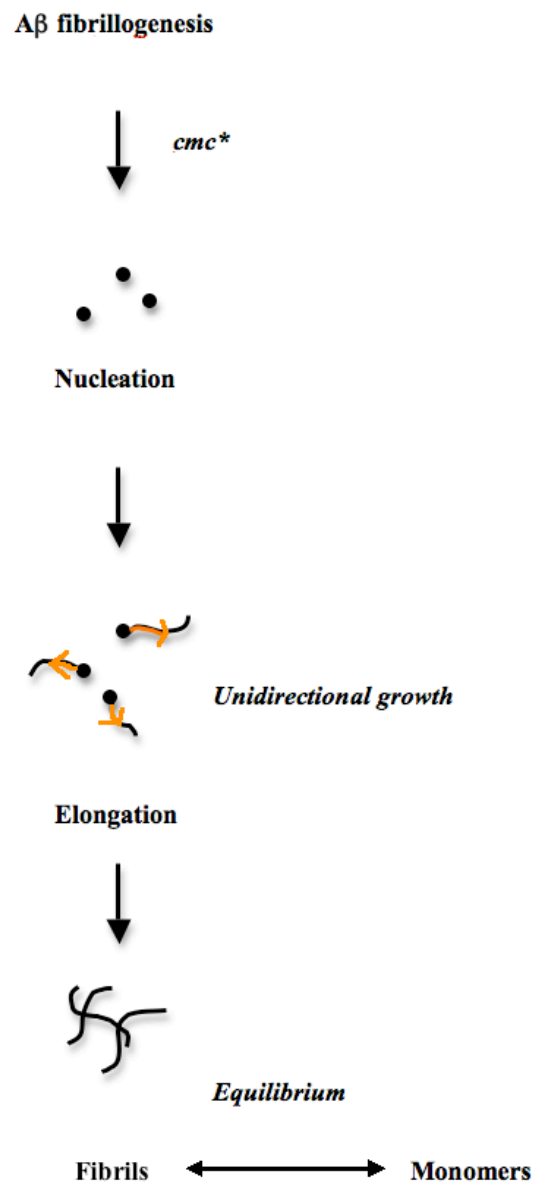
*Figure 2- 19 Schematic representation of Aβ fibrillogenesis. * Means critical monomer concentration.*

If a similar mechanism takes place in FF nanotube formation it is proposed that the difference in the FF tubes revolves primarily around the effect of HFIP (HFIP/water method) and heat (water method) on environmental conditions and solubility of the FF peptide which impacts on nucleation and growth kinetics. Firstly, it should be noted that the prepared peptide concentration is the same for both methods, although the solubility of the peptide in HFIP/water may be different than that in water at 65°C. As both samples display tubes, the achieved concentration of solubilised FF must be above the critical level required to achieve nucleation in the different solvents, or to continue elongation on preformed small tubes. However, the absolute value of this critical concentration is likely to be different in HFIP/water and water alone. The dilution with water of the HFIP may lead to ordering of the peptide at the HFIP-water interface with hydrophobic moieties oriented away from the aqueous phase providing an energetically favourable environment for the nucleation stage. This proposal is consistent with previous work in which it was suggested that the formation of the tubes (prepared by HFIP/water method) may be at the surface of the peptide solution [162]. The water-only method omits HFIP and involves heat. Since FF peptide is sparingly soluble in water at room temperature, heat is required to increase the solubility of the monomers to trigger nucleation. Although it should be noted that at 65°C insoluble particulates of FF could still be observed in the solution, it has nevertheless exceeded the critical concentration of FF to facilitate nucleation. Hence nucleation may be proceeding via a homogeneous nucleation route unaided by

a liquid-liquid interface or the insoluble aggregates may be playing a role in initiating nucleation.

The lower concentration of peptide in the water alone method (as indicated by the insoluble material) may favour the growth of a smaller number of tubes at a slower rate, but to an eventual greater length due to reduced crowding of the tubes as suggested by the SEM imaging of the HFIP/water samples. The increased time for growth may also allow a greater order in the molecular structure of the tubes and hence greater rigidity. However, it should be noted that the Raman Spectroscopy and XRPD data did not differentiate the tubes based upon internal molecular organization. Hence the assembled structure at the molecular scale level is identical.

The Raman Spectroscopy and XRPD results for FF nanotubes prepared by both methods are in good agreement with previous theoretical data and work where the unit cell was shown to be comprised of six FF molecules per turn that orient with the aromatic rings arranged outwards [96, 98]. π-π Interactions between adjacent aromatic rings and hydrogen bonding between peptide back bones were proposed to be the main forces that stabilize the tubular structure. In addition, the C=O bonds are perpendicular to the C-N bond and are aligned along the nanotube axis [85].

2.5 Conclusions

The studies in this chapter presented a comparative analysis of the structural properties of FF nanotubes prepared by the two established methods. FF peptide undergoes rapid self-assembly *in vitro* in both methods and the nanotubes produced present subtle differences in morphology. In general, FF nanotubes prepared in HFIP/water mixture are smaller in dimension and display bend features. Some nucleation centres were seen in these samples, with nanotubes projecting outwards from a core. The second method that involves only warm water as a solvent produced longer, discrete, and straight nanotubes with larger dimension. Raman spectroscopy and XRPD data have shown these nanotubes are indistinguishable by these techniques in terms of their molecular organization. The precise mechanism of growth for each type of nanotube is yet to be determined although comparison can be drawn with models related to the growth of amyloid fibrils. The role of the solvent HFIP appears critical in promoting significant nucleation and the consequent differences between the two types of tubes.

Chapter 3 Studies on Diphenylalanine Nanotube-Cell Interactions

3.1 Introduction

To date, applications of diphenylalanine (FF) nanotubes have focused on the area of nanoelectronics [76, 80, 93, 100, 101]. The physico-chemical properties of the tubes such as surface, thermo-mechanical and optical properties have been intensively studied [79, 85, 106], leaving the potential of FF nanotubes for pharmaceutical applications relatively unexplored. On the other hand, the cytotoxicity and biological potentials of carbon nanotubes, which were discovered approximately 30 years ahead of FF nanotubes have been assessed intensively [169-172]. Various cell lines and *in vivo* tests have been used to investigate the biocompatibility of carbon nanotubes. *In vitro* tests involve a number of cultured human cell lines, for example, cultured human blood cells, A549 lung cells, HeLa cells, and dermal fibroblasts [173-180]. *In vivo* tests include animal testing, for instance, subcutaneous tissue of rats [181-183]. Cell viabilities have been assessed using various indicator dyes, for example, Coomassie Blue, Alamar Blue, Neutral Red, MTT and WST-1, which evaluate the total protein content of cells, metabolic, lysosomal and mitochondrial activity respectively [174, 184-190]. Different factors that affect the cytotoxicity properties of carbon nanotubes have also been investigated, such as the type of carbon nanotubes (multi-walled vs. single-walled), the length,

specific surface area, and functionalization of carbon nanotubes, the choice of dye and possible interaction with nanotubes, and the interaction between serum in test medium and nanotubes [184, 188, 191-202]. A number of drug compounds have been successfully linked to the surface and to the end of carbon nanotubes [203, 204], examples include anticancer drugs such as methotrexate [205] and antitumor drugs such as 10-hydroxycamptothecin [206]. The anticancer activity/antitumor activity of the incorporated drugs had been proven to be enhanced from both *in vitro* and *in vivo* studies. For example, methotrexate when conjugated with multi-walled carbon nanotubes was shown to have an enhanced anticancer activity on a human breast cancer cell line [205]. Furthermore, *in vivo* single photon emission computed tomography imaging showed that 10-hydroxycamptothecin combined multiwalled carbon nanotubes had relatively long blood circulation and high drug conjugation in the tumour site [206]. Taken together, the research on carbon nanotube - drug complexes has indicated possible advantages of carbon nanotubes over conventional drug carriers (such as liposomes) due to their unique electrical properties, tubular shapes, and mechanical strength [207-211].

Compared with conventional drug carriers, FF nanotubes present several advantages: they self-assemble under mild conditions, so the manufacture is inherently scalable, simple and cost-effective; chemical modification and functionalization are easily achievable [78, 79, 162]. In contrast to carbon nanotubes, FF nanotubes are peptide based thus the biocompatibility problems of carbon nanotubes, such as debatable cytotoxicities raised from various

cytotoxicity assays with different cell lines [191], and poor excretion observed from *in vivo* studies [171], are less likely to occur with FF nanotubes.

Despite the apparent advantages FF nanotubes can offer in drug delivery, there are limited publications on FF nanotube-based drug delivery systems. Recently, a study investigated the cytotoxicity of FF-based hydrogel formed by a FF analogue comprising an-α, β-dihydrophenylalanine residue (ΔPhe) containing dipeptide H-Phe-ΔPhe-OH. The cytotoxicity was assessed on HeLa and L929 cells after exposure to the hydrogels using a MTT 3-(4,5-dimethylthiazol-2-yl)-2,5-diphenyltetrazolium bromide) assay. FF-based hydrogels showed no influence on the cells *in vitro*; the cell metabolic activity was maintained over 90% after 18 hours of incubation with the hydrogel [212].

The work presented here aims to provide more information regarding the biological properties of FF nanotubes by assessing the cytotoxicity of FF nanotubes on a HeLa cell line via a MTT 3-(4,5-dimethylthiazol-2-yl)-2,5-diphenyltetrazolium bromide) assay. The cytotoxic results were compared with that of the peptide alone. Furthermore, the effect of starting peptide concentration, the presence of serum in cell culture medium, and the presence of HFIP used in one of the preparation methods on the cytotoxicity of the nanotubes were also investigated. The stability of nanotubes in cell culture medium was assessed using SEM and nanotube-cell interactions were studied using total internal reflection microscopy (TIRM). Taken together, these studies provided knowledge of the biological properties of FF nanotubes.

3.2 Materials and Methods

3.2.1 Materials

HeLa cells were purchased from the European Animal Cell Culture Collection. All cell culture reagents such as Dulbecco's modified Eagle's medium (DMEM), Phosphate buffered saline (PBS), sodium dodecyl sulfate (SDS), N,N-dimethylforamide (DMF), 3-(4,5-Dimethylthiazol-2-yl)-2,5-diphenyltetrazolium bromide (MTT), and Mass spectroscopy materials including formic acid and acetonitrile were purchased from Sigma Aldrich.

3.2.2 Methods

3.2.2.1 Cell culture

HeLa cells were cultivated on 75 cm^2 flasks in Dulbecco's modified Eagle's medium (DMEM) supplemented with 10 % foetal bovine serum (FBS), 2 mM L-glutamine, 100 IU/ml penicillin, and 100 μg/ml streptomycin. Flasks were incubated at 37 °C and in an atmosphere of 5% CO_2. Cells were trypsinized every 3 days. The medium was first aspirated out, and then cells were rinsed with 10 ml of PBS. Trypsin-EDTA (5 ml, 0.25%, composed of 2.5 g porcine, trypsin and 0.2 g EDTA, 4Na/L HBSS) was applied to dissociate cells from the flask. The flask was incubated for approximately 5 minutes until cells were detached from the flask and suspended in trypsin. Medium (10 ml) containing 10 % of serum was added to the flask to stop the reaction of trypsin.

The cell suspension was transferred to a centrifuge tube and centrifuged for 5 minutes at a speed of 13,000 rpm. The supernatant was pipetted out and cells were left at the bottom of the tube. Medium (10 ml) containing 10 % serum was applied into the tube and the cell pellet was re-suspended several times to ensure a good mixing. Cell suspension (1 ml) was then transferred into a new flask, along with 9 ml of pure medium containing 10 % serum.

3.2.2.2 Cytotoxicity assay

3.2.2.2.1 Determination of Optimal number of cells per well

Cells were trypsinized as described above. After the cell suspension had been centrifuged, cells were diluted in 3 ml of medium containing 10 % serum. Cell suspension (100 μl) was placed in a microcentrifuge tube, followed by addition of 100 μl of trypan blue and thorough mixing. Trypan blue is a vital dye. The reactivity of trypan blue is based on the fact that the chromophore is negatively charged and does not interact with the cell unless the membrane is damaged. Therefore, living cells are excluded from staining.

A hemocytometer was used for cell counting. A Pasteur pipette was used to transfer a small volume of the trypan blue-cell suspension to a chamber on the hemocytometer (This was done by carefully touching the edge of the cover-slip with the pipette tip and allowing the chamber to fill by capillary action).

All the living cells were counted (non-viable cells stain blue, viable cells will remain opaque) in the four squares of the chamber. Cell counting was repeated on the other chamber of the hemocytometer.

The subsequent cell number per ml of cell suspension was determined using the following equation (Equation 3.1) and diluted to obtain 500,000 cells/ml or 200,000 cells/ml.

$$Cells\ /\ ml = no.\ of\ cells\ (per\ square) \times dilution\ factor \times 10^4 \quad (3.1)$$

Medium containing 2% serum (100 μl) was added to each well from column 3 to 10 of a flat bottom 96 well plate (Corning, NY). Cell suspension (200 μl) was added to each well in column 2. Dilutions were made by transferring 100 μl of cell suspension from a previous column to the next column using a multi-channel pipette (Fisherbrand, UK). Thus a 1:2 dilution was achieved, with cell number per well starting from 50,000 and 20,000. Pure medium was added to column 11 as a control.

Plates were incubated (37°C, 5% CO_2) for 24 hours before the cell culture medium was removed from each well. Fresh medium containing 10% serum (100 μl) and 50 μl of MTT (0.5mg/ml in PBS) added into each well. Cells were incubated at 37 ºC and stirred on an orbital shaker (Memmert, Germany).

Solution was removed after a 4-hour exposure, and rinsed with 100 μl of PBS. One hundred micro litre of SDS (10 %, in 50 % DDH_2O and 50 % DMF) was added to each well, and plates were left in an oven on the orbital shaker (approximate 20-24 hours) until all formazan crystals had been dissolved. The

absorbance of each well was determined in a Spectra Max automatic multi-plate reader (Dynex, USA) at 570 nm. The determination of optimal number of cells/well was done on three different occasions, with two plates (6 wells/plate) for each occasion.

3.2.2.2.2 3-(4,5-Dimethylthiazol-2-yl)-2,5-diphenyltetrazolium bromide (MTT) assay

The cytotoxicity of different concentrations of FF nanotubes prepared by both methods in presence or absence of serum in the medium was evaluated on HeLa cells (passage number: from 25 to 41) using the colorimetric MTT assay. MTT assay measures the activity of reductase enzymes that reduce MTT dyes (yellow colour) to formazan dyes (purple colour). Such enzymes are only active in living cells' mitochondria, therefore the conversion can be used to measure cellular metabolic activity [189].

Medium was removed after 24 hours. FF nanotubes were prepared according the method described in Section 2.221 and 2.222 of Chapter 2. FF nanotube suspensions were dried overnight at 65°C in an oven, then re-hydrated with DMEM (4 ml) with or without serum at room temperature and stored at 4 °C. Free FF peptide solutions were made by dissolving FF powder in medium with or without serum, then left to dissolve at room temperature and stored at 4 °C.

Cell suspension was prepared by diluting cells in medium containing 2 % serum to obtain 100,000 cells/ml. Cell suspension (100 µl per well) was plated

in a 96 well plate from column 2-11. Plates were incubated (37 °C, 5 % CO_2) for 24 hours to allow the cells to attach to the wells.

The medium was removed as described previously and cells were exposed to 100 μl of different concentrations of FF nanotubes or free FF peptide in medium with or without serum (suspensions were pre-heated to 37 °C in a water bath). Nanotube suspensions (100 μl) with a starting FF concentration of 1000 μg/ml were seeded to the first column of 96 well plate, subsequent dilution of the tube suspension by a factor of 2 were added to the next columns. Different controls were used. Firstly, the cell culture medium was used as a negative control representing 100 % metabolic activity. Secondly, 2% w/v of SDS in medium was used as a positive control representing 0% metabolic activity. Thirdly, HFIP (1 % in DDH_2O, i.e. same concentration as used in the preparation of the nanotubes) after evaporation overnight at 65 °C and re-suspension of the residue in cell culture medium was used to evaluate the cytotoxicity of the residue solvent in FF nanotubes prepared in HFIP/water mixture. Plates were incubated at 37 °C in the incubator.

Nanotube suspensions were removed from each well after 20 hours of exposure. Medium (100 μl) containing 2% serum and 50 μl of MTT solution was added on to each well. Plates were incubated at 37 °C on the shaker for 4 hours. Solution was then removed and each well was rinsed with 100 μl of PBS. SDS (100 μl, 10%) was added to each well, and plates were then stirred at 37 °C until all the formazan crystals had dissolved. Absorbance was read at a wavelength of 570 nm.

The percentage metabolic activity was calculated by subtracting the absorbance of the positive control (dead cells) then dividing each value by the negative control (100 % metabolic activity) x 100 %. Each cytotoxicity assay was performed on two cell passage numbers (2 plates, 6 wells per plate).

3.2.2.3 Scanning electron microscopy (SEM) characterization of FF tubes in cell culture medium

Pre-prepared FF nanotube suspensions (For methods of preparation, please refer to Section 2.221 and 2.222 of Chapter 2) were dried overnight at 65 °C in an oven. DMEM with 5 % serum was then added to the vial containing dried nanotubes. The DMEM-nanotube suspension was stored for 24 hours at 4 °C. Aliquots (20 µl) of the suspension (pre-heated to 37 °C in a water bath) were placed onto freshly cleaved mica substrates (Agar Scientific Ltd., Stansted, UK), and gently dried in a stream of nitrogen gas. The mica substrates were then mounted onto 12 mm aluminium sample stubs (Agar Scientific Ltd.) using carbon tabs (12 mm diameter, Agar Scientific Ltd.) The samples were then coated with a thin layer of gold to facilitate imaging (argon gas with an ion current of 30 mA). SEM images were recorded using a JSM JEOL 6060 SEM (JEOL, Tokyo, Japan) operating at 10 kV.

3.2.2.4 Mass spectroscopy

FF nanotubes were prepared in HFIP/water mixture using the standard protocol (please refer to Section 2.221), dried at 65°C overnight and re-hydrated with

double distilled water (DDH$_2$O) to the same concentration. The mass spectrometer used was a 2795 spectrometer with electrospray ionization (Waters, UK).

Positive mode

Sample suspension (10 µl) was transferred into a sample vial using a pipette. Formic acid (200 µl, 0.1 %, Sigma Aldrich) in DDH$_2$O and 200 µl of 0.1 % formic acid in acetonitrile (Sigma Aldrich) were added to the suspension

Negative mode

Sample suspension (10 µl) was transferred into a sample vial using a pipette. DDH$_2$O (200 µl) and 200 µl of acetonitrile were added to the suspension.

3.2.2.5 Total internal reflection microscopy (TIRM)

DMEM-nanotube suspension was prepared according to the method described earlier in Section 3.222 of this chapter. HeLa cells (100,000 cells/ml) in 1 ml of DMEM (containing 2 % serum) were seeded on a glass cover slip (Sigma and Aldrich) coated with polystyrene (Sigma and Aldrich) and placed inside of a cell culture disc for 24 hours. The glass cover slip was then transferred into the sample holder of the microscope with the addition of 1 ml of fresh DMEM (10% serum) and 100 µl of DMEM-nanotube suspension.

All studies were performed using a custom-built widefield high-resolution inverted microscope. TIRM imaging of living cells was achieved with a light

emitting from a HeNe laser with the wavelength of 633 nm (LXHL-ML1D Luxeon Star, Lumileds, CA). The beam was expanded to fill the back aperture of the objective (Nikon, CFI Apochromat x60, NA1.49, oil immersion) for high spatial resolution. A rotating ground glass diffuser was placed at the conjugate plane of the back focal plane of the objective in order to achieve a spatial incoherence Koehler illumination. The camera utilized to acquire images was a monochromatic CCD (Sony XCD-SX910) with 1280 (H) x 960 (V) resolution. For video imaging, frames were streamed to a kinetic image disc on a PC and then saved to hard disc. Analysis of still images and video sequences was performed with ImageJ.

3.2.2.6 Statistical analysis

All results are expressed as the mean ± standard error of the mean (SEM).

The GraphPad Prism (GraphPad Software, USA) for Windows was used for statistical evaluations. Differences between treatment and control groups were tested by standard T-test (one-tailed, two samples assuming equal variance); effect of peptide dilution was tested by one-way analysis of variance (one-way ANOVA), effect of serum combined with peptide dilution was tested by two-way ANOVA without replication, followed by multi-comparisons between groups using Tukey-Kramer's test. Differences at $p < 0.05$ were considered significant.

3.3 Results

3.3.1 Cytotoxicity study

3.3.1.1 Determination of Optimal number of cells per well

As mentioned earlier, in the MTT assay, the absorbance of each well is dependent upon the amount of formazan formed, which is proportional to the number of metabolically active cells only over a limited range of cell densities for a fixed MTT concentration. The optimal number of cells per well needed therefore to be determined prior to undertaking the cytotoxicity tests.

As seen on Figure 3-1, a linear relationship between cell number and absorbance was obtained up to 12500 cells/well. The absorbance leveled off at higher cell density. To further investigate the linear region, a third MTT assay was conducted, starting with a number of cells/well of 20,000 instead of 50,000. As seen on Figure 3-2, a consistent linear relationship between absorbance and the number of metabolically active cells was shown over the range of 0-20,000 cells/well. The mid-point on the line (i.e. 10,000) was chosen as the optimal number of cell per well.
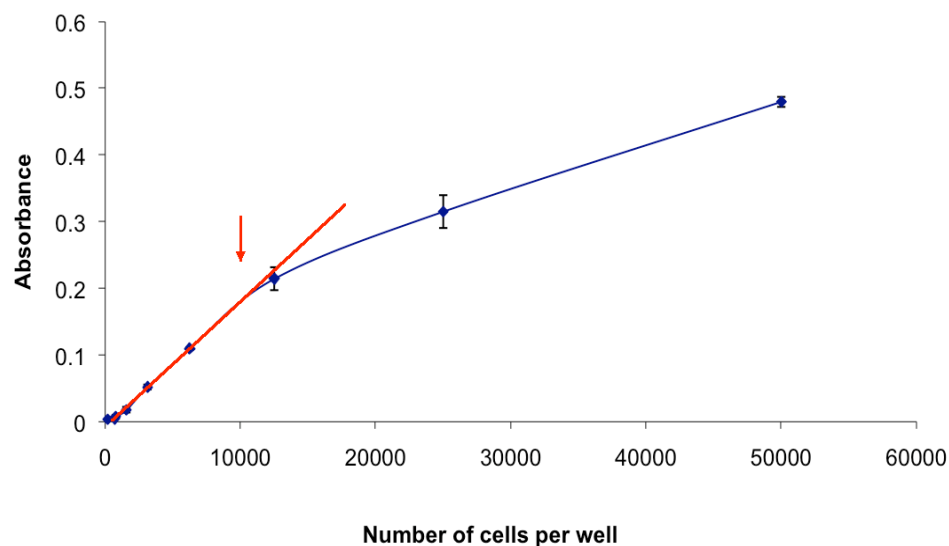
Figure 3- 1 Relationship between cell number and absorbance. Red line shows the linear relationship between number of cells (up to 12500) and absorbance. Arrow shows cell number (10,000/well) that would be used in future cytotoxicity experiments. Data are presented as mean ± SEM (n = 2 plates, 6 replicates per plate).
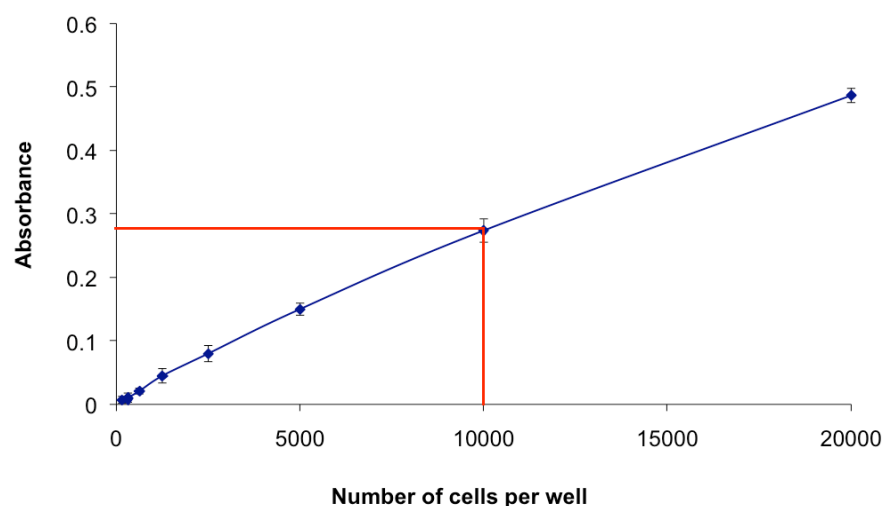
Figure 3- 2 Relationship between cell number and absorbance. Starting cell number was 20,000 per well and diluted in the ratio of 1:2. Data are presented as mean ± SEM (n = 2 plates, 6 wells per plate).

3.3.1.2 MTT assay

Once the optimal number of cells per well had been decided, a series of cytotoxicity experiments with FF nanotubes were carried out. The effects of concentrations of FF peptide, methods of FF nanotubes preparation and the presence of serum in the medium were tested.

From previous published papers, it is known that the peptide monomer concentration can affect the size and the morphology of the nanotube assemblies [105]. For the study presented here, a starting peptide concentration of 1000 μg/ml was selected as it was the standard concentration for all other experiments presented in this thesis. A series of nanotube suspension dilutions were made according to the method described in section 3.2.2.2.2. Furthermore, nanotubes were also prepared by different methods and re-suspended in DMEM with or without serum to investigate the effect of preparation method and presence of serum on the metabolic activity of HeLa cells.

3.3.1.2.1 Cytotoxicity of FF nanotubes prepared in HFIP/water mixture

Figure 3-3 is a representation of the HeLa cell mitochondrial activity variation caused by FF nanotubes prepared in HFIP/water mixture at a starting concentration of 1000 μg/ml. The tube suspension was gradually diluted by a factor of 2 to make up a series of nanotube suspensions at different concentrations ranging from 1000 μg/ml to 31.25 μg/ml. As presented, the average percentage MTT metabolism of HeLa cells after a 24h exposure to nanotubes remained above 80% of that of untreated cells both in DMEM with /

without serum. The statistical analysis showed that none of these data was significantly different from the control.
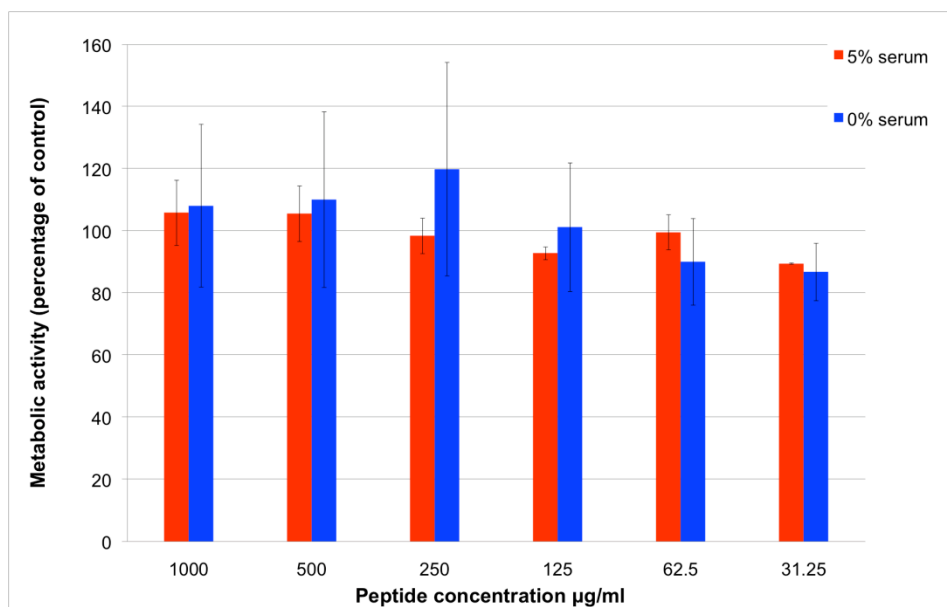
Figure 3- 3 Effect of dilution on the cytotoxicity of FF nanotubes made in HFIP/water mixture using a FF starting concentration of 1000 μg/ml. Red columns represent the nanotubes re-suspended in medium containing 5% serum and blue columns represent nanotubes re-suspended in medium without serum. Data are presented as mean ± SEM (n = 2 plates, 6 wells per plate).

3.3.1.2.2 Cytotoxicity of FF nanotubes prepared in water alone

To evaluate the effects of tube preparation on cellular metabolic activity, FF nanotubes were prepared in water alone and incubated with HeLa cells in DMEM with/without serum. As shown in Figure 3-4, an overall cellular metabolic rate above 80% was achieved for both tubes suspended in medium

with/without serum. There was no significant difference between treated cells and untreated controls.
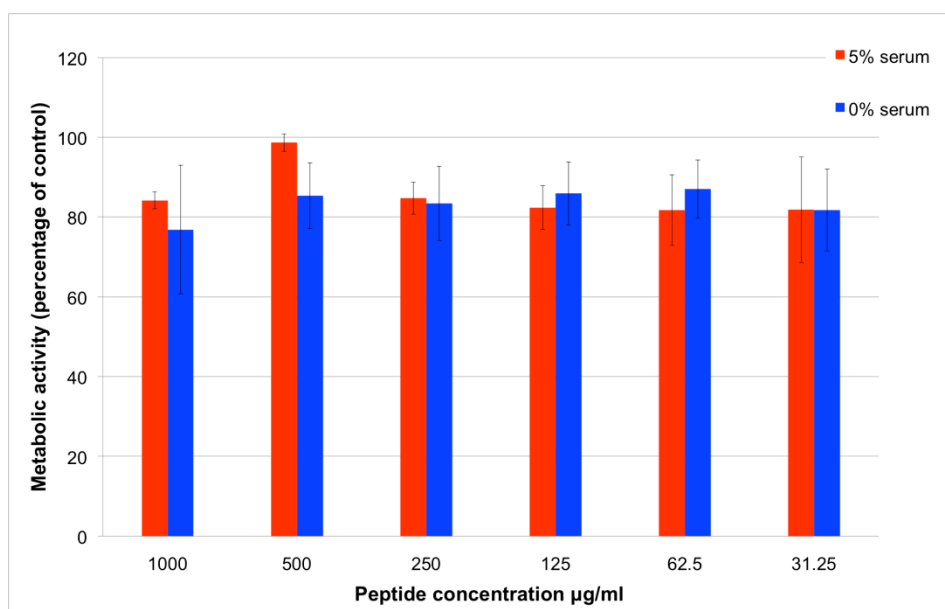
Figure 3- 4 Effect of dilution on the cytotoxicity of FF nanotubes made in water alone using a FF starting concentration of 1000 μg/ml. Red columns represent the nanotubes re-suspended in medium containing 5% serum and blue columns represent nanotubes re-suspended in medium without serum. Data are presented as mean ± SEM (n = 2 plates, 6 wells per plate).

3.3.1.2.3 Cytotoxicity of FF peptide

For comparison, MTT assay of HeLa cells exposed to FF peptide was also conducted and the results are presented in Figure 3-5. Cells exposed to the peptide in DMEM in presence or without serum retained a high mitochondrial

metabolism above 80%. There was no significant difference found between treatment groups and controls.
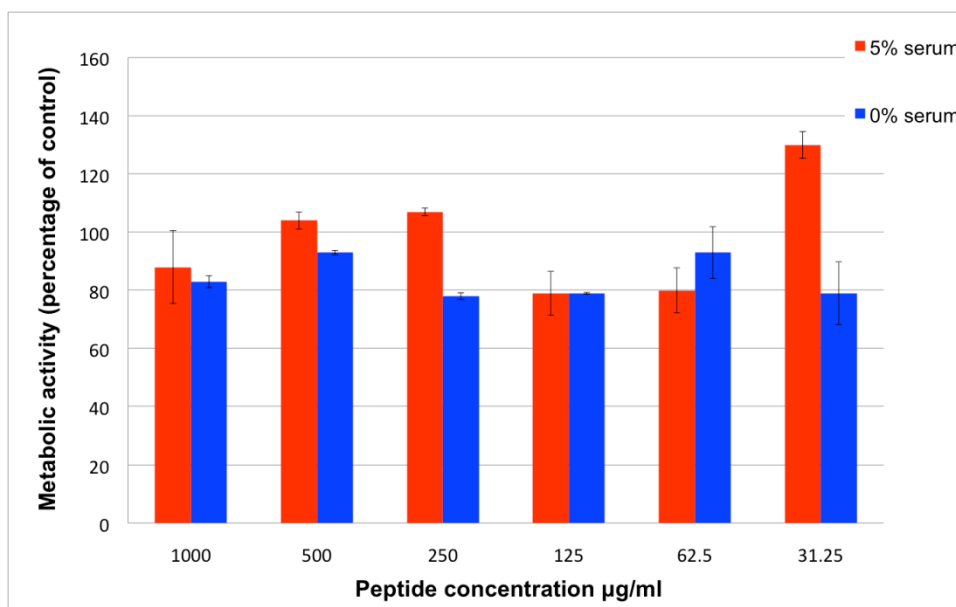
Figure 3- 5 Effect of dilution on the cytotoxicity of FF peptide. Red columns represent the peptide suspended in medium containing 5% serum and blue columns represent peptide suspended in medium without serum. Data are presented as mean ± SEM (n = 2 plates, 6 wells per plate).

3.3.1.2.4 Cytotoxicity of 1,1,1,3,3,3- hexafluoropropan-2-ol (HFIP)

As previously mentioned, HFIP is known to cause destruction of the mucous membrane in the upper respiratory tract and eyes [94] and is expected to be cytotoxic. The cytotoxicity of HFIP was examined on cells exposed to HFIP/DMEM mixture. As presented in Figure 3-6, clearly HFIP does have a toxic effect; there is significant toxicity in HeLa cells caused by HFIP at concentrations of 1%, 0.5% and 0.25% v/v HFIP/DMEM in presence of 5%

serum (p values <0.0001), and at all concentrations from 1% to 0.0625% v/v HFIP/DMEM without serum (p values of top four concentrations are <0.0001 and of the lowest concentration is 0.009). The percentage cellular metabolic activity gradually increased with further dilution of HFIP/DMEM mixture and at concentrations of 0.125% and 0.0625% v/v, there was no observed cytotoxicity to HeLa cells in presence of serum. Moreover, significant difference of cellular metabolic activity was found between cells with/without serum ($p = 0.01$).
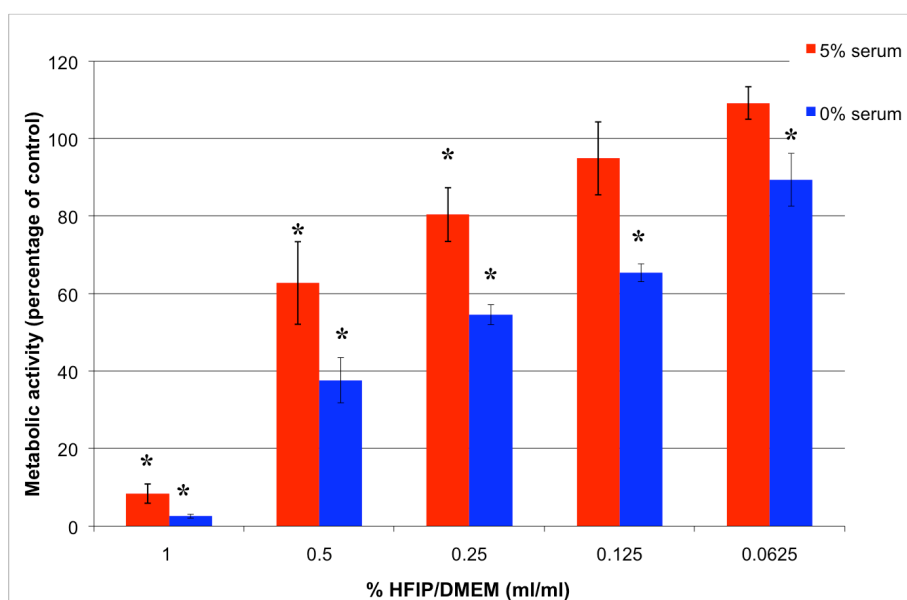
*Figure 3- 6 Effect of diluting HFIP on the metabolic activity of HeLa cells. The starting concentration is 1%v/v HFIP/DMEM, same solvent concentration as in the 1000 μg/ml FF peptide solution used to prepare the nanotubes. Red columns represent HFIP diluted in DMEM containing 5% and blue columns represent HFIP diluted in DMEM containing 0% serum. Data are presented as mean ± SEM (n = 2 plates, 6 wells per plate). * Means significantly different from the corresponding control.*

3.3.2 Scanning electron microscopy characterization of FF tubes in cell culture medium

The serum used in the MTT assays was fetal bovine serum (FBS), which is a complex matrix containing proteins (bovine serum albumin is the major constituent), hormones, vitamins and some other substances [213]. As a control, it is essential to ascertain the stability of FF tubes in culture medium containing FBS. After overnight re-suspension of FF tubes prepared by both methods in DMEM with 5% serum, the stability of FF nanotubes was investigated by scanning electron microscopy characterization.

Figure 3-7 represents a selection of SEM images taken from FF tubes (as prepared by both methods) in DMEM with 5% serum. Figure 3-7a is a low-resolution SEM image of FF nanotubes prepared in HFIP/water mixture. Similar to previous images of nanotubes made by this type of preparation, close association between the tubes and projection from a common nucleation centre were observed. Figure 3-7b and 3-7c are high-resolution images chosen from different areas from Figure 3-7a. The selected nanotube portions are straight with a diameter that is within the normal range (427 ± 39 nm, n = 45). These tubes, however, were not discrete. Branching was observed as shown in Figure 3-7b and some thin tube-like connections between each individual tubes were also seen in Figure 3-7c. Figure 3-7d represents SEM image of FF tubes prepared in water alone. Tubes were straight, long and unbranched with no significant difference in morphology as compared to the previous SEM images of tubes prepared by this type of method (683 ± 55 nm, n = 45). The

background solution, i.e. DMEM with 5 % serum without nanotubes was also imaged, as shown in Figure 3-7e. Crystalline features were observed.
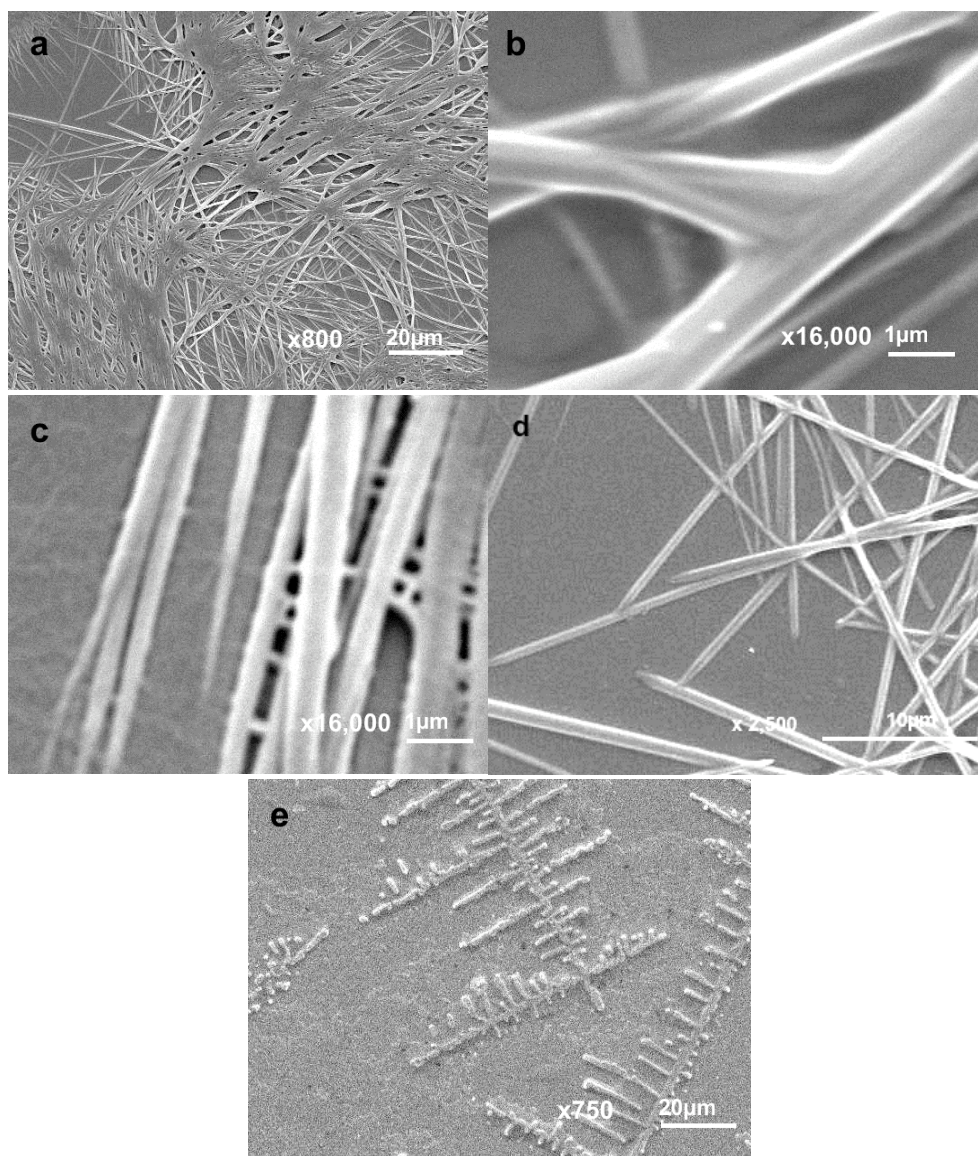
Figure 3- 7 SEM micrographs of FF nanotube re-suspended with DMEM with 5% serum. Figure 3-7a, 3-7b and 3-7c represent FF nanotubes prepared in HFIP/water mixture. Figure 3-7d represents FF nanotubes prepared in water alone. Figure 3-7e represents the background medium (i.e. DMEM with 5% serum alone).

3.3.3 Mass spectrometry

As shown in Figure 3-3, the metabolic activity of HeLa cells exposed to FF tubes prepared in HFIP/water at 1000 μg/ml was observed to be above 80 %. On the other hand, HeLa cells exposed to 1 % v/v HFIP/DMEM (i.e. the same concentration of HFIP used in tube preparation) clearly had a toxic response, with over 90 % reduction in MTT conversion. This paradox might indicate that the HFIP content was somehow reduced by the evaporation process (65 °C overnight) involved in sample preparation. To confirm the conjecture made, mass spectrometry was performed on the samples prepared after the evaporation process (dried residues were re-hydrated with equal volume of DDH_2O.).

The mass spectra presented in Figure 3-8 were obtained under negative ion mode. No peaks were detected under positive ion mode, which suggested the detected ions were all negatively charged. The top spectrum of Figure 3-8 represents the mass spectrum of HFIP as a control (the volume used was the same as the amount of HFIP used in FF tube preparation). The molecular ion peak of interest is 166.9828. The bottom spectrum shows the spectrum of the residue left after evaporation of nanotube suspension and re-hydrated with equal amount of DDH_2O. The molecular ion peaks of interest are 311.1371 and 166.9794, respectively.

Figure 3- 8 Mass spectra of (a) pure HFIP and (b) nanotubes prepared in HFIP/water mixture (dried and re-suspended with equal volume of DDH$_2$O).

3.3.4 Total internal reflection microscopy

Total internal reflection microscopy (TIRM) is an important technique for investigating biological samples. The principle of TIRM relies on the total internal reflection of the incident light, which only happens when the incident angle is equal or greater than the critical angle. Because the refractive index is lower on the substrate side of the boundary, light will be completely reflected

[214, 215]. Comparing with normal brightfield microscopy, TIRM offers advantages not only in increased image contrast, but also in depth discrimination due to the feature of the evanescent wave generated as a result of the total internal reflection [214, 215]. Substances that are closely adhered to the substrate surface can be easily discriminated in TIRM since the light beam comes from the bottom of the sample, propagating through the substrate (i.e. glass cover slip for this experiment) then the cell media. Figure 3-9 represents image of a HeLa cell captured using brightfield microscopy and TIRM using the same objective lens and same camera. Figure 3-9a represents the brightfield microscopy image of a HeLa cell with size in the range of 20-30 μm. A line plot of the region across the cell and polystyrene coated glass surface (as highlighted in Figure 3-9a) is illustrated in Figure 3-9b. The intensity of the region is indicated by the grey value on the y-axis, and as seen from the plot the intensity of the cell surface and that of the glass surface do not have much difference with highest grey value of 165. Figure 3-9c represents the TIRM image of the same cell. It can be seen that TIRM image appears darker compared to the brightfield image, which reveals that TIRM offers better contrast of the same object. The same region was analyzed by line plot shown in Figure 3-9d. A typical distribution plot is seen that starts from low grey value of around 150 (the glass surface) to a broad distribution of high grey value at around 190 (the cell surface) and then levels off again (the glass surface).

Nanotube suspension in DMEM with 10 % serum was added to the sample with HeLa cells attached. A time-lapse investigation was performed and TIRM

images were captured every 10 seconds for a time course up to 12 hours. Representative images are presented in Figure 3-10. Figure 3-10a is a selected HeLa cell (the same cell as shown in Figure 3-9) before adding nanotube suspension. Figure 3-10b represents the image of the same cell captured with nanotubes suspension added after 300 seconds. The appearance of nanotubes were observed, both found approaching the cell and inside of the cell (as indicated by the arrows). The size of the nanotubes inside the cell is around 2 μm in length and few nanometers in width which is in the range of tube dimension found earlier (Chapter 2 Results, section 2.3.1.2). Figure 3-10c is another example of a HeLa cell with smaller dimension (around 20 μm in length and 5 μm in width) before adding nanotubes. The location of nanotubes of lengths around 2 μm inside of the cell can be seen in Figure 3-10d at time = 300 s (as shown by the arrows). Figure 3-10e was captured after 12 hours of adding nanotube suspension. No cells can be seen, i.e. no attachment of cells to the substrate, which is an indication of cell death. A large number of nanotubes with different dimensions (lengths are around few micro meters and widths are nanoscaled) were observed.
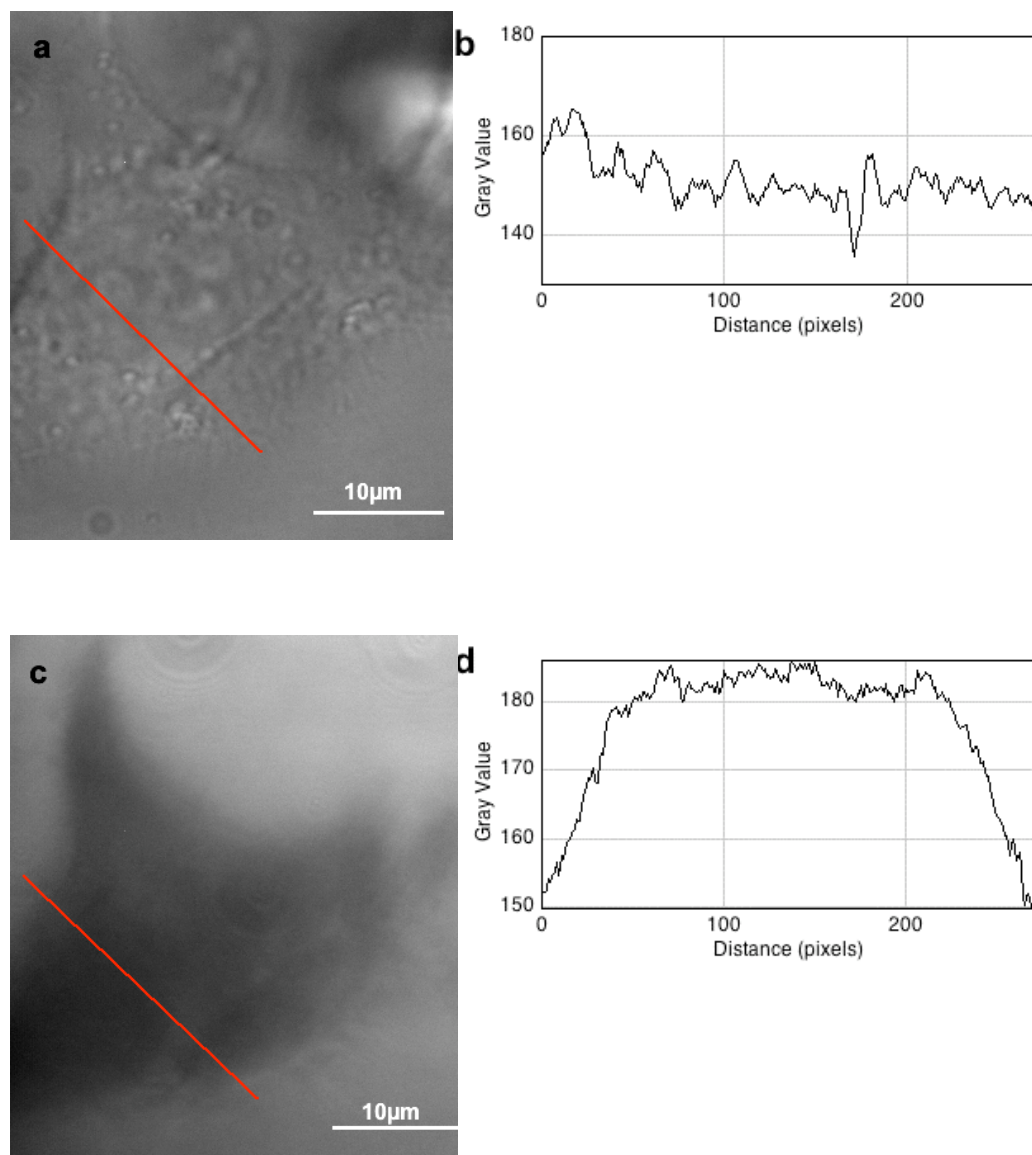
Figure 3- 9 Brightfield and TIRM images of HeLa cells. Figure 3-9a represents a brightfield image of HeLa cell obtained using transmitted imaging modality. Figure 3-9b is a line plot of the region illustrated in a. Figure 3-9c represents the corresponding TIRM image of the same cell. Figure 3-9d is a line plot of region illustrated in c.
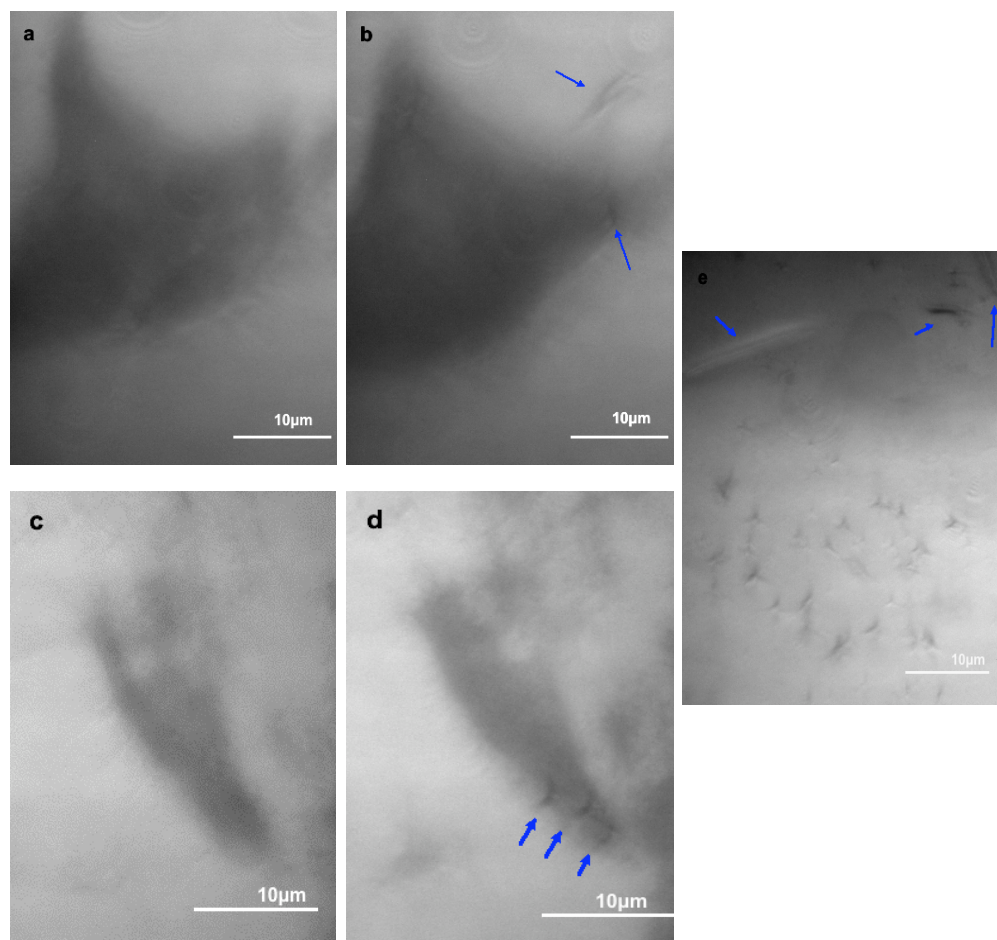
Figure 3- 10 Image selections from typical time-lapse TIRM movie of HeLa cells on a polystyrene coated coverslip with nanotube-DMEM suspension added. Figure 3-10a is a selected HeLa cell, Figure 3-10b represents the same cell surrounded by nanotubes at t = 300s (highlighted by arrows). Figure 3-10c and 3-10d represent another cell with intracellular nanotubes (highlighted by arrows) at t = 300s. Figure 3-10e is an image captured after cells were dead (t = 12h, a number of small nanotubes were observed at the bottom of the image, with few large tubes seen at the top (shown by arrows).

3.4 Discussion

3.4.1 Effect of diphenylalanine peptide and nanotube on HeLa cell cytotoxicity

The cytotoxicity of FF nanotubes prepared in the HFIP/water mixture and in water alone and FF peptide was assessed on HeLa cells using an MTT assay. The conversion of the yellow MTT dye into purple formazan crystals was used to quantify cell mitochondrial activity. The results of MTT conversion presented in Figure 3-3, Figure 3-4 and Figure 3-5 in general are above 80%, which suggests the peptide-based nanotubes and the peptide itself do not cause any significant decrease in the cellular mitochondrial metabolism. It is known that the morphology of the assemblies can be altered from long tubular structures to other shaped nanostructures with smaller dimensions by tuning peptide solution parameters such as the peptide concentration, pH and temperature of the solvent, and the type of solvents [105, 106, 108]. The SEM characterization investigations in Chapter 2 (section 2.3.1.2) have shown that by changing the solvent type and temperature (one preparation involves HFIP/water mixture and the other one involves water, plus the addition of heat) the morphology of assembled tube is diverse (from long, discrete tubular structures to branched structures with nucleation centres); furthermore, as previously discussed in Chapter 2 section 2.3.1.4, the distribution of FF nanotube dimension is different by different preparations; the water-alone method produces slightly larger tubes with diameters mainly in the range of 600 – 700 nm, whereas the tube diameter of the ones prepared in HFIP/water mixture mainly scaled from 200-300 nm. The high cellular metabolic activities

indicate that despite the differences in nanotube morphology and tube sizes, the cellular responses to FF tubes are similar. This finding is consistent with previous studies on carbon nanotubes which had shown that there was no variation in the observed *in vitro* toxicity/response of cell lines exposed to carbon nanotubes with different sizes [183].

As proven by the SEM study (Figure 3-7), FF tubes are shown to be stable after DMEM re-suspension (with and without serum); moreover, the tubes are seen in solution when submerged in DMEM from the FTIR images (Figure 3-10). The maintenance of the tube morphology may be of value in possible applications involving drug delivery, where maintenance of tube aspect ratio may improve cellular uptake [216, 217], and their incorporation into tissue engineering scaffolds where mechanical properties can be critical in maintaining structural integrity and in determining cell differentiation pathways [218, 219].

The tubes made in water alone are preferred for drug delivery applications, as there will be a need to ensure complete removal of the toxic HFIP from tubes prepared by the solvent-method. In addition, the long, discrete and unbranched morphology (as shown Figure 3-7) may present a better value in biological applications. Although nanotubes prepared by both methods show encouraging results in the MTT assays, it should be noted that these were only preliminary studies and as mentioned earlier, more cytotoxicity assays, such as neutral red uptake and lactate dehydrogenase release assay with different cell lines are required in order to fully understand the cytotoxicity of FF nanotubes.

3.4.2 Cytotoxicity of HFIP

HeLa cells were exposed to HFIP at the same concentration (1% v/v) as in a preparation of the nanotube suspension at 1000 μg/ml. HFIP showed significant cytotoxicity to HeLa cells at concentrations of 1% to 0.25% v/v HFIP/DMEM in presence of serum, and at concentrations of 1% to 0.00625% v/v HFIP/DMEM without serum, respectively (Figure 3-6). As HFIP is diluted, there was significant increase in cellular metabolic activity. The negligible reduction in cell metabolic activity of the nanotubes (Figure 3-3) suggested there was little/no HFIP residue left by this method of preparation due to the overnight evaporation. This hypothesis is qualitatively confirmed by the mass spectroscopy study (Figure 3-8). The peak at 166.9828 in Figure 3-8a indicates the molecular ion peak of HFIP (molecular weight 168). It is one less than the molecular weight of HFIP due to the loss of one hydrogen atom. Six fluorine atoms act as electron-withdrawing groups, pulling electrons away from the central carbon. Oxygen is also an electron-withdrawing atom, which makes the hydrogen attached to oxygen easily to be removed, as shown in Figure 3-11.
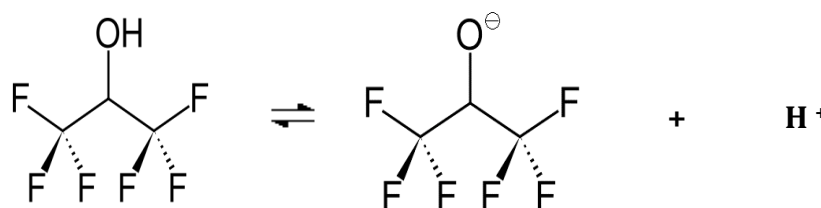
Figure 3- 11 Schematic equation of ionization of HFIP

The ion peak of HFIP is also detected in the nanotube sample as shown in Figure 3-8b (mass to charge ratio = 166.9794). Another interesting reading from the nanotubes rehydrated with DDH_2O sample is at 311.1371, which is a predominated peak of almost 100% in the sample spectrum. The number is one less than the molecular weight of diphenylalanine (molecular weight 312). This result shows that there was trace of FF peptide in the nanotube suspension, which may be the starting material that has not self-assembled into nanotubes. This finding is consistent with the percentage yield of FF tubes calculated for both method of preparation (please refer to the supportive document), which showed that the yield is approximately 70.3 % for the solvent method, and approximately 77.2 % for the water method.

The addition of serum in cell culture medium does not have an influence on cell survival rate in presence of nanotubes prepared by different methods and FF peptide (Figure 3-3 to Figure 3-5). One obvious explanation could be the tubes and peptides are naturally non-toxic to the cells in terms of metabolic activity. The serum, however, does have an effect on cellular metabolic activity when cells were incubated with HFIP (Figure 3-8). The percentage celluar metabolic activity of HeLa cells with serum was in general higher than that of the cells without serum; a significant difference was found between these two treatment groups ($p = 0.01$). Clearly serum plays a vital role in protecting cells from toxic HFIP. One possible explanation could be that serum proteins (e.g. albumin) have the ability to entrap toxic HFIP molecules via possible interactions such as hydrophobic interactions. Furthermore, HFIP exhibits a strong hydrogen bonding capacity and will associate with most molecules with

receptive sites such as oxygen, double bonds, or amine groups. Proteins could be very susceptible to bind HFIP since they have extensive amounts of carboxyl and amine groups. Although there is no published work on the interaction between HFIP and serum proteins such as albumin, some work has proven that bovine serum albumin has the ability to entrap other small alcohol molecules such as ethanol [220]. If there is binding between the serum components and HFIP, a reduction in toxicity would be expected, which is consistent with the MTT results (Figure 3-8). This finding is consistent with results found in cytotoxicity experiments with carbon nanotubes. After exposure to cells, it was found that a greater toxicity was demonstrated with carbon nanotubes/nanoparticles in the absence of serum, indicating a protective effect of serum on cells and significant interaction between serum and carbon nanotubes/nanoparticles [195, 197].

3.4.3 HeLa cell characterization by total internal reflection microscopy (TIRM)

The aim behind this study was to investigate HeLa cell behaviour when surrounded by an extracellular environment occupied with FF nanotubes. Cellular behaviour at interfaces is important for many applications including drug delivery. The ability of cells to uptake liposomes or biodegradable nanostructures such as peptide nanotubes [221] or to be used as cages for monodispersed nano-sized drug delivery system [222] offers the opportunity for targeted delivery. In order to access these delivery systems, the interaction

between cells and drug carriers has to be studied to assure structural stability and successful delivery.

The technique adopted in this investigation is total internal reflection microscopy (TIRM) which is known as a high resolution live cell imaging technique that has been utilized for studying cells at interface [223]. The major advantages of TIRM over other microscopic or spectroscopic techniques include the allowance of free motion of cell/particle under the influence of all forces acting on them, increased image contrast, and the fact there is no need to label particles/cellular structures [223].

The images presented in Figure 3-9 were captured of the same HeLa cell using different imaging techniques, i.e. brightfield imaging using the transmitted light function of camera (Figure 3-9a) and TIRM (Figure 3-9c), respectively. Clearly from the comparison between these images, TIRM offers a more in depth characterization due to the nature of evanescent illumination. One thing that needs to be taken into consideration when choosing TIRM as the technique to study cells adhered to a substrate is the substrate thickness and roughness. The substrate thickness needs to be within the range of the evanescent wave penetration depth (which is normally around 100-200 nm) otherwise it will not be visible by TIRM [215]. Roughness of the substrate is another key parameter in TIRM imaging as scattering of the evanescent field will occur if the substrate surface is too rough [214]. Based on these considerations poly-lysine was therefore the chosen polymer to be coated onto the glass cover slip to promote cell adhesion in this study because of two reasons: firstly, poly-lysine has a molecular weight in the range of 75,000 – 100,000 and can be

homogenously distributed on glass cover slip with a coating thickness of a few nanometers; and secondly it exhibits a low surface roughness (root mean square value = 0.35 nm), which clearly is an order of magnitude smaller than the evanescent wave penetration depth [224]. Nevertheless, despite the drawbacks of TIRM, it still presents the advantage of a more in depth discrimination compared to normal brightfield images (as shown in Figure 3-9); the image quality and resolution in terms of intensity variation of the images (Figure 3-9a and Figure 3-9c) are evidently presented in Figure 3-9b and Figure 3-9d.

Dynamic information of cells with influences of all forces and on the interaction between cells and the surrounding extracellular environment can also be achieved using TIRM with high-speed time-lapse imaging. Video-rate imaging was applied on HeLa cells in presence of nanotube suspension (please refer to supporting documents). Clearly from the videos, nanotubes underwent free diffusion in extracellular bulk medium; The HeLa cell membrane reorganized with retraction and expansion motions in response to nanotube approaches. This result is consistent with previous experiments done on fibroblast cells with TIRM imaging after exposure to sub-micron sized polymeric particles [225]. The cell membranes were found to be re-organized and lamella protrusion and retraction also played a key role in fibroblast locomotion from the TIRM time-lapse imaging.

The series of images presented in Figure 3-10 are representative images taken from a time-lapse investigation of HeLa cells immersed in FF nanotube suspension; the images of cells with nanotubes presented were taken at time =

300 s after adding nanotube suspension (Figure 3-10b and Figure 3-10d). Nanotubes with dimensions that were less than 20 μm in length and few nanometers in width were seen outside of the cells. Moreover, short nanotubes with length of about 2-3 μm were appeared to be uptaken by the cells (Figure 3-10c and 3-10d). According to the physicochemical characteristics of the nano-carriers, there are several cellular uptake pathways in general, and depending on the nature of the target cell and different mediators, they can be classified into clathrin-mediated endocytosis, caveolae-mediated endocytosis, macropinocytosis, and phagocytosis [226]. The cell of interest in this study, i.e. HeLa cell is human cervical cancer cell and therefore it is not phagocytotic since this process is only accomplished by specialized cells such as macrophages, monocytes and neutrophils. A key factor in determining cell uptake pathway, besides the nature of the cell, is the size of drug carrier [226]. Caveolae are small flask-shape pits of approximately 50 nm in diameter; clathrins form vesicles of approximately 100 nm in diameter [227]; macropinocytosis is the process by which molecules of the largest size are internalized, the diameter range of the vesicles formed is from 0.5 − 5 μm [228]. The tubes found inside of HeLa cells in Figure 3-10 were about 2 μm in length and few nanometers in width. Macropinocytosis may be the cellular uptake pathway of these small FF tubes. Nevertheless, the dimension of FF nanotubes is very diverse; the length ranged from few micrometers to more than 1000 μm. Only tubes with lengths shorter than 5 μm may qualify for this process and larger tubes (as for the ones shown in Figure 3-10c and 3-10d) were only observed outside the cells. It should be pointed that the TIRM

experiments presented here were only preliminary, in order to fully understand the celluar uptake mechanism, a large quantity of experiments are required.

Cell death was observed after 12 hours of nanotube exposure (Figure 3-10e). This was considered to be a result of the experimental conditions for several reasons. Firstly, cells are unlikely to survive at room temperature (~ 20 °C), atmospheric N_2/O_2 ratio ($\sim 78 : 21$), and presence of debris for a long period. Secondly, the MTT assays applied on HeLa cells have shown high cell viability after 24 hours nanotube incubation. Finally, cell death was also observed in untreated cells after 12 hours.

It is an important finding that small FF tubes were found inside of living cells in respect of the potential in drug delivery as drug carrier. Although small molecules can pass through cell membrane easily via simple diffusion, there is a number of therapeutic drugs that may need carriers in order to be taken up by cells, one example is nucleic acids which are unable to cross the cell membrane [229]. FF nanotubes are non-toxic in terms of cell metabolic activity and can be taken up by living cells, which are important findings for their future pharmaceutical applications.

3.5 Conclusions

The studies presented in this chapter focused on the investigation of the cytotoxicity of FF nanotubes prepared either in HFIP/water mixture, or in water alone. In general, the performed MTT assays have revealed that the nanotubes and FF peptide did not cause any mitochondrial related damage to

HeLa cells. Interestingly, cells were observed to uptake short tubes with a length around 2 μm through a suggested macropinocytosis pathway. Moreover, the toxic HFIP used in the sample preparation was found removed by the evaporation process. HFIP on its own has shown a highly toxic effect on HeLa cells with over 90% decrease in cell metabolic activity. Although FF tubes prepared by both methods present encouraging results from these studies, more cytotoxicity assays with different cell lines are needed to evaluate the cytotoxic property of FF nanotubes. Nevertheless, these observations clearly do not rule out potential applications of FF nanotubes in the pharmaceutical and biomedical areas.

Chapter 4 Evaluation of the Potential of Diphenylalanine Nanotubes as a Drug Carrier

4.1 Introduction

In previous chapters, detailed characterization of FF peptide nanotubes using a variety of microscopic and spectroscopic techniques such as AFM, SEM, and Raman, plus cell-based investigations such as the MTT assay and TIRM imaging have been presented. Based on the knowledge obtained, the work presented in this chapter focuses on the investigation of the potential of FF nanotubes as a carrier in drug delivery.

As mentioned in Chapter 1, many efforts have been made to investigate the biological potential of FF-based nanostructures [78, 118, 136, 141, 212]. Due to their physical and chemical properties, research into FF-based assemblies has grown at an accelerating pace in recent years [138, 145]. A number of published studies have demonstrated their potential, including for cell growth support in 3D cell culture [230], as part of a novel biosensing platform for enzyme-biosensor applications [131], and to enhance the performance of carbon nanotube-based nano-electronic devices [164].

In order to evaluate a FF nanotube-based drug delivery system, several criteria need to be understood: first, the physical, chemical properties of the carrier; second, the biocompatibility of the carrier; third, the stability of the drug-

loaded FF nanotube whilst *in vitro* and *in vivo*; and important parameters regarding the pharmacodynamic and pharmacokinetic profile of the release *in vivo*. There is little information published on peptide nanotube-based drug delivery system despite the apparent advantages it can offer, such as biocompatibility, biodegradability, ease to fabricate and low cost. The aim of the work presented in this chapter is to synthesize and characterize drug-loaded FF nanotubes and evaluate their potential in drug delivery applications by conducting *in vitro* dissolution experiments.

4.2 Experimental

4.2.1 Materials

Agents used in drug/tube synthesis and dissolution study were purchased from Sigma-Aldrich including diphenylalanine peptide (FF), 1,1,1,3,3,3- hexafluoro-2-propanol (HFIP), salicylic acid (SA), 5-fluorouracil (5FU), ethanol, dimethyl sulfoxide (DMSO), and phosphate buffered saline (PBS).

4.2.2 Method

4.2.2.1 FF tube synthesis

As mentioned earlier, FF tubes prepared in water alone are perferred for biological and pharmaceutical applications because of the absence of HFIP as well as the maintainance of structural integrity in presence of buffers, such as PBS. FF tubes were synthesized as previously described: lyophilized FF

peptide was mixed with ddH$_2$O at 65 °C for thirty minutes, suspensions were then left to cool to room temperature.

4.2.2.1.1 SA-FF tube synthesis

For investigation of the effect of salicylic acid concentration on tube formation: SA powder was dissolved in a mixture of 1:9 ethanol/ddH$_2$O with different quantities to make up a series of concentrations: 2mM, 1mM, 0.5mM, and 0.2 mM. One part of SA solution was mixed with one part of FF tube suspension with 30 seconds vortex mixing and 24 hours incubation.

To study the effect of solvent on tube formation: SA powder was dissolved a mixture of ethanol: ddH$_2$O with varied ethanol content, ranging from pure ethanol, 1:1 ethanol/water, 2:3 ethanol/water, 1:4 ethanol/water and 1:9 ethanol/water. The concentration of SA was fixed at 0.2 mM. Again, equal volumes of SA solution were mixed with FF tube suspension and vortex mixed for 30 seconds and then incubated for 24 hours.

For the dissolution test and other characterization analysis including XRPD and UV-Visible spectroscopy experiments, SA solution used in sample preparation was 0.2mM and the solvent was 1:9 ethanol/water.

4.2.2.1.2 5FU-FF tube synthesis

To investigate the effect of 5FU concentration on tube assembly, 5FU was dissolved in 1:9 DMSO/ddH$_2$O with different quantities to make a final solution of 1mM, 0.4 mM, 0.2 mM and 0.1 mM. Next, equal volumes of 5FU solution were mixed with freshly prepared FF tube suspension and vortex mixed for 30 seconds. Samples were kept for 24 hours at room temperature.

For other experiments including dissolution testing, XRPD and UV-Visible spectroscopy, 0.1mM was chosen to be the optimal concentration for 5FU solution.

4.2.2.2 SEM characterization

Samples of drug-mixed, drug-free nanotube and pure drug dissolved in corresponding solvents were placed on freshly cleaved mica substrates (Agar Scientific Ltd., Stansted, UK), and gently air-dried. The mica substrates were then mounted onto 12 mm aluminium sample stubs (Agar Scientific Ltd.) using carbon tabs (12 mm diameter, Agar Scientific Ltd.). The samples were then coated with a thin layer of gold to facilitate imaging (argon gas with an ion current of 30 mA). SEM images were recorded using a JSM JEOL 6060 SEM (JEOL, Tokyo, Japan) operating at 10 kV. The size of the tubes was measured using SM-35080 SMILE VIEW software.

4.2.2.3 UV-Visible spectroscopy

The UV-Vis spectra of both pure drug sample and drug/tube mixtures were obtained on a Cary 50 UV-Vis spectrophotometer (Varian Inc.). In order to find the wavelength of maximum absorbance, a whole wavelength scan was performed on both drug samples (3 ml) at a wavelength range from 200 nm to 400 nm.

4.2.2.4 Powder X-ray diffraction

XRPD measurements were recorded on a Bruker D8 (Bruker, Coventry, UK). Dried samples of drug-free FF tubes and drug/FF tubes mixtures were loaded into glass capillaries (0.7 mm, Capillary Tube Supplies Ltd.). Data were collected in step scan mode between 2.0° and 90° (2θ) with a step size of 1° and a counting time of 10 s/step. The working conditions were 10 kV and 30 mA. All peak positions were used for the determination of micro structural parameters.

4.2.2.5 Percentage drug loading

After being incubated for 24 hours, drug/FF tubes mixtures were centrifuged at 10,000 rpm for 5 minutes. The concentration of drug remaining in the supernatant after centrifugation was measured at 296 nm and 266 nm, which are the maximum absorbance wavelengths as determined by previous UV-Vis spectroscopy study for SA and 5FU, respectively. The percentage drug loading

was calculated by subtracting the amount of drug in the supernatant from the total amount used, and then dividing by the total amount of drug used.

4.2.2.6 Dissolution study

The *in vitro* release of SA and 5FU from FF nanotubes was determined by the dialysis method. Samples of drug/tube mixtures and free drug powder were loaded into hard gelatin capsules (100 mg) with glass beads. 3 cm of dialysis tube (MWCO 2000, Sigma-Aldrich) was cut-off and placed under ddH_2O for 24 hours. Both the inside and outside of the membrane were washed several times to remove impurities. Both ends of the membrane were closed with tied knots, and then this was placed in PBS (0.1M, pH 7.4) for 1 hour. The prepared drug samples were enveloped in the pre-treated dialysis membrane and air bubbles were removed before sealing the dialysis bag. The dialysis membrane was then immersed in a 200 ml beaker containing 100 ml of PBS (0.1 M, pH 7.4) and with a stir bar placed at the bottom. The beaker was placed in a water tank with a set temperature at 37 °C. The dissolution experiment was performed for 2 hours; aliquots of samples (3 ml) were taken out at predetermined time points; the same amount of fresh medium was replaced into the beaker immediately at each time. Samples were analyzed using the UV-Vis spectrophotometer at an appropriate wavelength (296 nm for SA and 266 nm for 5FU). For comparison, the release of pure drug from hard gelatin capsule loaded with glass beads was also conducted. All of the experimental conditions were kept the same for parallel comparison.

4.3 Results

4.3.1 Background: choosing a drug candidate

Choosing an appropriate drug is the first step to study the potential of FF nanotubes as drug-carrying vehicle. The candidate should have a molecular structure that is capable of forming interactions with FF nanotubes and ideally a well-characterized drug so that the *in vitro* release profile can be compared with previous delivery systems. A molecular representation of FF nanotubes is shown in Figure 4-1 [97]. As presented in the figure, the nanotube consists of extensive π-π interactions and H-bonding between each adjacent peptide; therefore an ideal drug should have an aromatic ring and a hydrogen donor/acceptor group that is capable of forming π-π interactions and H-bonding with the FF tube. Based on these considerations, two drug candidates were selected: salicylic acid and 5-fluorouracil (Figure 4-2). These two drug molecules have a planar structure with an aromatic ring and polar groups such as hydroxyl, carbonyl and cyclic amide groups that perfectly fit into the expected structure of an 'ideal drug' for FF tube. Furthermore, these drugs are well known molecules that have been studied for many years; salicylic acid (SA), is the precursor for aspirin, and is widely used in organic chemistry and in small quantities it can be used in acne treatment and as a food preservative [231]; 5-fluorouracil (5FU) is an anti-cancer drug that was discovered and synthesized by Charles Heidelberger in 1957, and is a clinically important drug in treatment of colon cancer and pancreatic cancer [232]. These drug candidates have been studied with a variety of delivery system, including

polymer-based matrix/films/microspheres/microfibers, peptide and lipid hydrogels, and tablets [233-237].
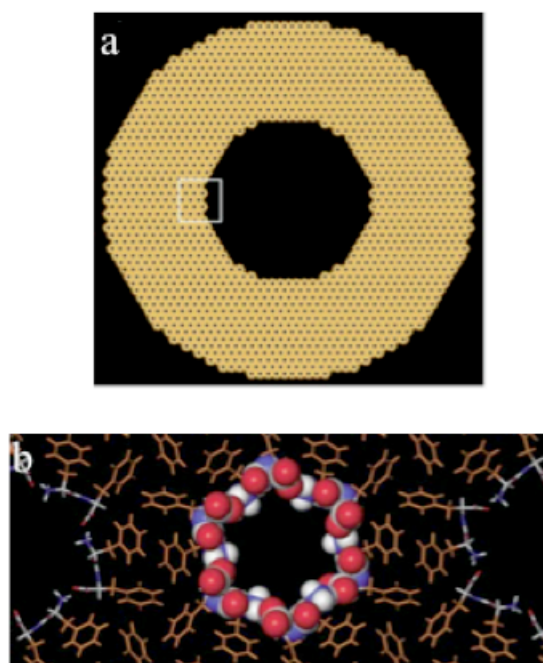
Figure 4- 1 Molecular model of FF nanotube. Figure 4-1a is a constructed model of a FF nanotube with a 110 nm outer diameter and a 50 nm inner diameter; Figure 4-1b is an enlarged section as highlighted by the rectangle shown in (a). The atoms constituting the pore are presented using a space-filling illustration. As shown by the detailed view, the pores of the FF tube are composed of peptide bonds with H-bonding between adjacent peptide backbone, the aromatic rings orientate outside forming extensive π-π interactions [97].
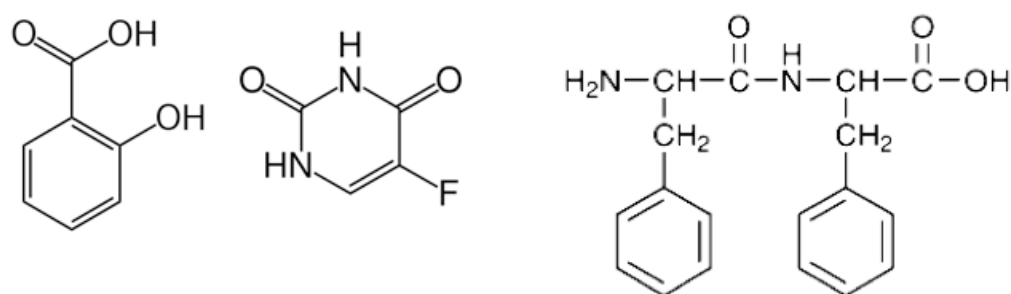
Figure 4- 2 Molecular structures of salicylic acid (left), 5-fluorouracil (middle), and diphenylalanine comprising the L-isomer of phenylalanine (right).

4.3.2 Characterization of salicylic acid/diphenylalanine nanotube mixtures

Samples of FF nanotubes mixed with SA were characterized using SEM, UV-Visible spectroscopy, and XRPD.

4.3.2.1 SEM

As mentioned in previous sections, several factors are known to have influence on the formation of self-assembled FF nanotubes [105, 106]. The investigation presented here focuses on the effect of solute concentration and choice of solvent on the formation of FF tubes. The morphology of FF nanotube mixed with SA at various concentrations and percentages of ethanol content was observed under a scanning electron microscopy. Apart from the two variables, other experimental parameters were kept constant, such as FF peptide concentration (1 mg/ml), and SEM instrument parameters.

4.3.2.1.1 Different salicylic acid concentrations

The SEM micrographs presented in Figure 4-3 are images of samples prepared by mixing freshly prepared FF nanotubes solution with SA solution (dissolved in 1:9 ethanol/water) with different concentrations, ranging from 2 mM to 0.2 mM (Figure 4-3a to Figure 4-3d), and aged for 1 day before being air-dried. The morphology of the self-assemblies varies with different SA content; few needle-like formations were found at the highest SA ratio (Figure 4-3a) with

length around 20 µm. As SA content was reduced by an order of magnitude of 2, fibril-like structures were observed in Figure 4-3b with length of more than 100 micrometers and widths less than a micron. As SA concentration was further reduced, a network of tubes and fine fibrils were found (Figure 4-3c) with the diameter of the tubes around 1 µm. Finally, the sample formed by mixing FF tubes with 0.2 mM SA solution presenting long, uniformed and discrete tubes of similar dimension and morphology to bare FF tubes (Figure 4-3d and 4-3f), the average diameter is 1.8 ± 0.3 µm and lengths are up to several hundred of microns (n = 35). Pure SA crystals were also prepared and presented in Figure 4-3e. The needle-like morphology is consistent with previous published studies on the crystal morphology of SA [238]. Because of the obtained size uniformity and lack of excessive SA crystals, 0.2 mM SA solution was therefore used in the all sample preparations for the dissolution study and other characterization analysis (unless indicated) presented in this chapter.

4.3.2.1.2 FF assembled in different ethanol percentages

SEM micrographs of FF nanotubes mixed with 0.2 mM salicylic acid solution of various ethanol content are illustrated in Figure 4-4. Five different proportions were chosen by varying the ratio between ethanol and water, ranging from pure ethanol (i.e. FF peptide was dissolved in HFIP with ethanol dilution in absence of water) to ethanol/water = 1: 9. Since the amount of SA used in preparing these samples was the same, any differences in tube

morphology observed in Figure 4-4 were solely as a result of the change of the solvent. A network of gel-like structures and drug crystals were observed at 100 % and 1:1 ethanol/water (Figure 4-4a and 4-4b). No tubes were observed, and compared with the needle-shaped pure SA crystals presented in Figure 4-3e, it was found that the presence of FF peptide and water strongly influences the morphologies of the resultant SA crystals. While increasing the water content to ethanol/water = 2:3 (Figure 4-4c), leaf-like SA crystals appeared with an average width of 8.7 ± 0.8 µm and an average length of 103 ± 5.1 µm (n = 35). FF fibrils/tubes were only observed at ethanol/water = 1:4 or below (Figure 4-4d and 4-4e). Fine fibrils with a feather-like morphology were present at ethanol/water = 1:4, with average width 320 ± 18 nm and the lengths up to hundreds of micrometers (n = 35). When the water content was the highest (ethanol/water = 1:9), well-formed tubes with diameters around 1.4 ± 0.8 µm and micrometer lengths were present (n = 35).
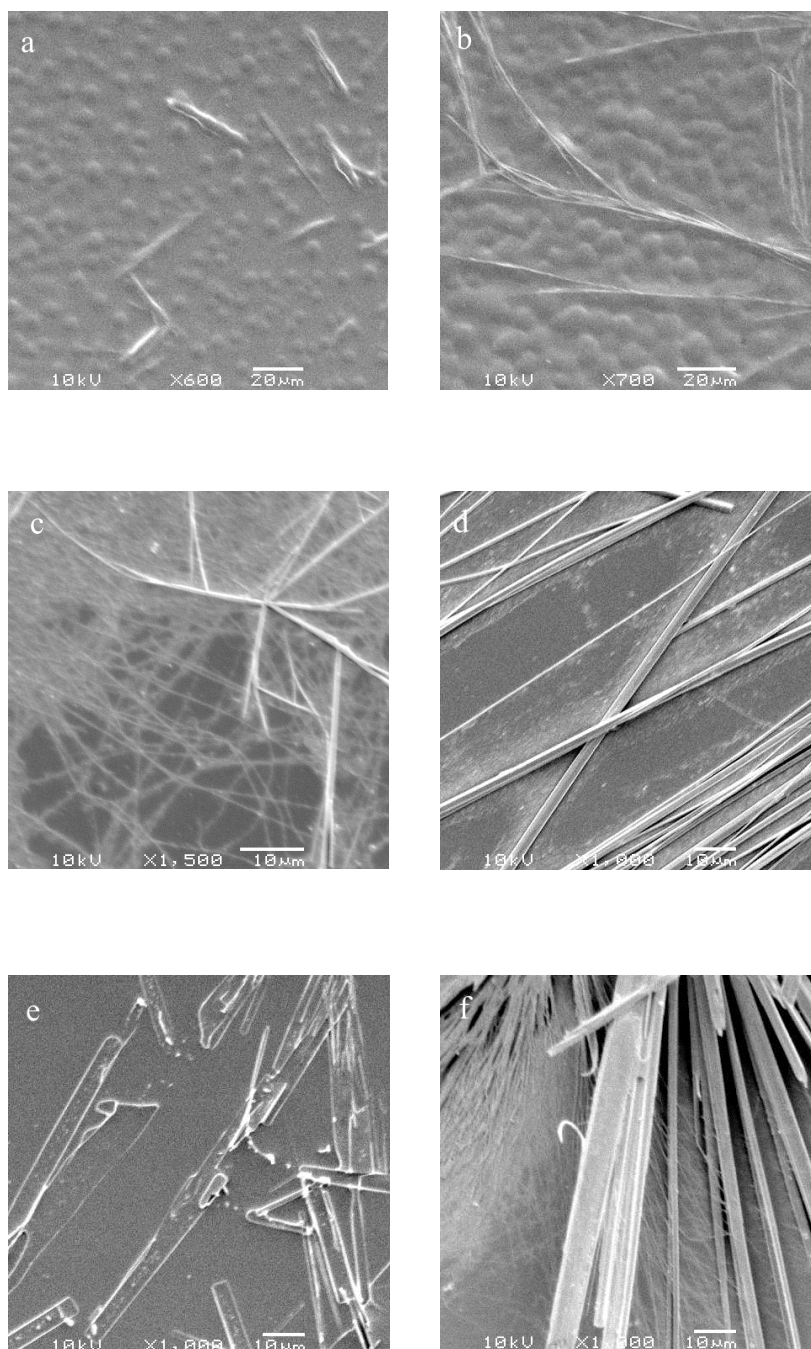
Figure 4- 3 SEM micrographs of FF nanotubes mixed with SA. SA is dissolved in a mixture of ethanol to water = 1:9 with various concentrations (a) 2mM, (b) 1mM, (c) 0.5mM, (d) 0.2mM; SA crystals (dissolved in ethanol) are presented in 4.3e; bare FF nanotubes in ethanol/water =1:9 without SA loaded is presented in 4.3f.
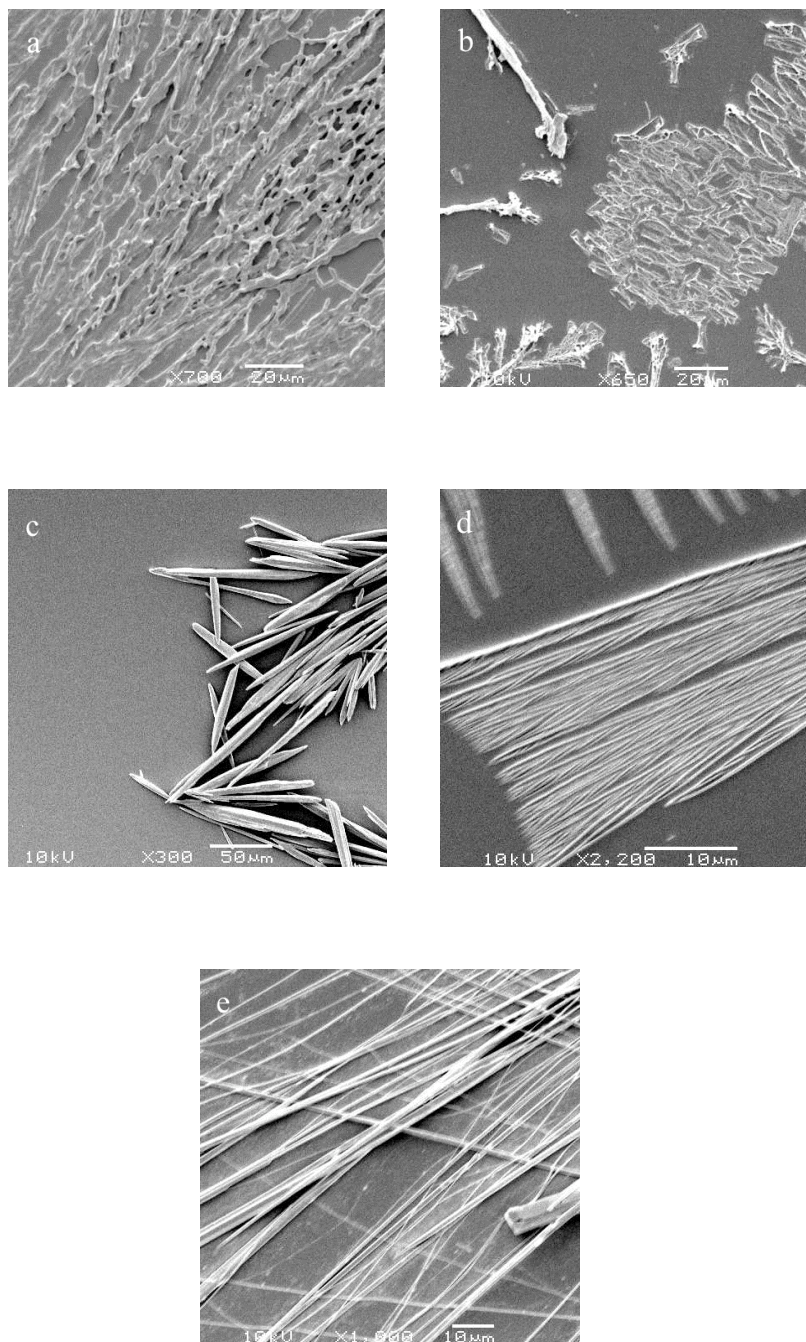
Figure 4- 4 SEM micrographs of FF nanotube/SA mixtures formed in different ethanol percentage. Ethanol to water content is varied from (a) pure ethanol (b) 1:1, (c) 2:3, (d) 1:4 and (e) 1:9. The SA solution used to prepare these samples was 0.2mM.

4.3.2.2 UV-Visible spectroscopy

UV-Vis spectra of FF nanotubes mixed with SA, and of free SA are presented in Figure 4-5. As shown in the spectra, the peaks associated with SA are shown at 297.2 (Figure 4-5a) and 294.9 nm (Figure 4-5b). Both values are close to the reference value of SA (296 nm) showing a good accuracy [238]. The peak at wavelength 255.1 nm was attributed phenylalanine. The peak at 229.9 nm was another peak related to SA, which is missing in Figure 4-5a, probably due to the broadening of the phenylalanine peak. For the drug release experiment, dissolution samples were analyzed using the standard wavelength of SA, which is 296nm.
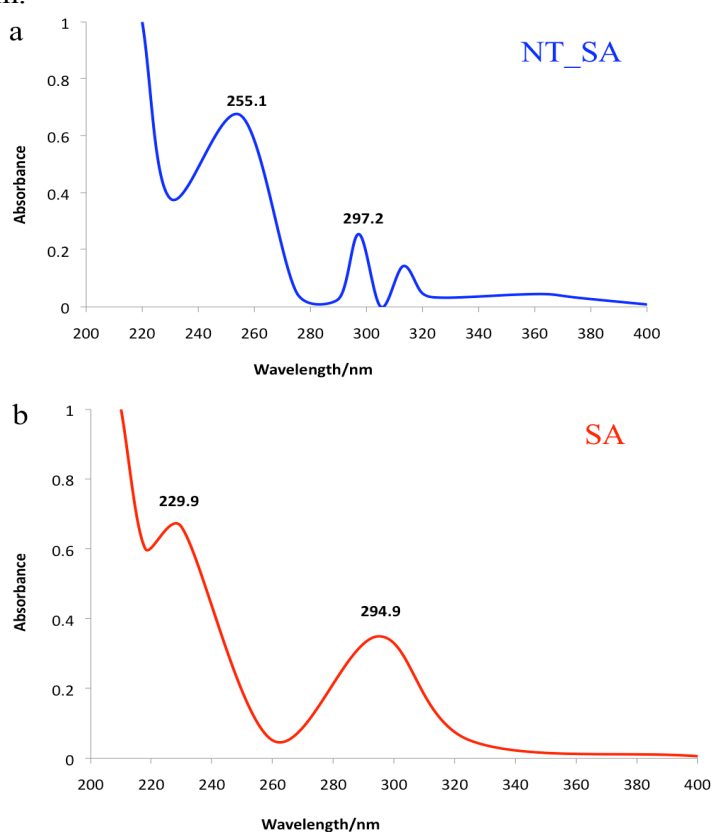
Figure 4- 5 UV-Vis spectra of FF nanotube/SA and free SA. (a) FF tubes mixed with SA (0.2mM), and (b) SA alone. Peaks of interest are labelled.

4.3.2.3 Powder X-ray diffraction

To further characterize SA/FF nanotubes mixtures, XRPD was performed on dried samples of the mixtures. The patterns presented in Figure 4-6 were obtained from FF nanotubes (Figutr 4-6a) and nanotubes with SA (Figure 4-6b). There is little/no difference observed between the two patterns.
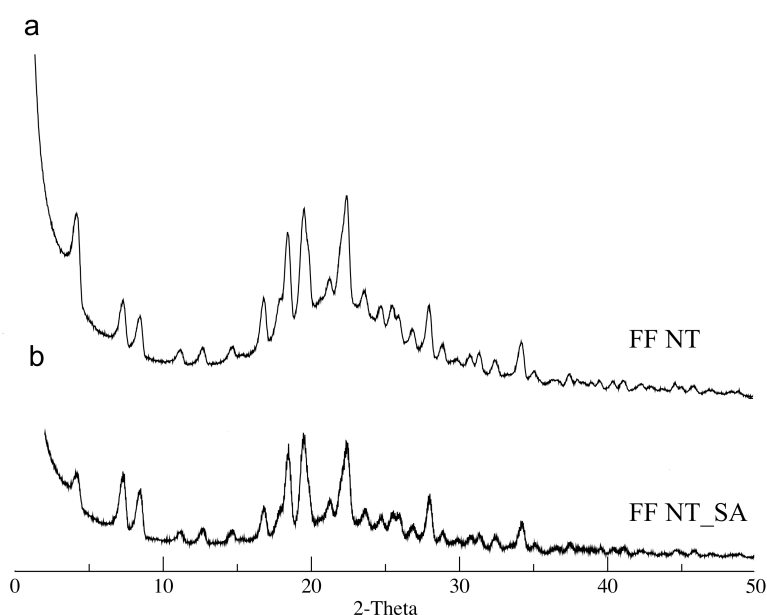
Figure 4- 6 XRPD patterns of FF nanotubes with and without SA. (a) drug-free FF tubes, and (b) SA-mixed FF tubes (0.2mM).

4.3.2.4 Salicylic acid loading capacity

The observed relationship between SA loading capacity and the concentration of SA solution is presented in Figure 4-7. FF solution of a fixed concentration (1mg/ml) was mixed with SA dissolved in ethanol: water (1:9) mixture with 4

different concentrations. After 24 hours incubation, the drug content was shown to increase rapidly from 0.41 % to 3.67 % as the concentration of SA solution is increased from 0.1 mM to 0.5 mM; further increase in concentration from 0.5 mM to 1 mM has little effect on % loading (drug content is 4.00% at 1 mM), which indicated a possible SA loading limit for FF tubes. This suggestion is supported by SEM analysis (Figure 4-3); the morphology of FF tubes changed from tubular to fibillar as SA concentration was increased with eventually no tubes being formed, which may indicate a possible influence of SA on FF tube self-assembly.
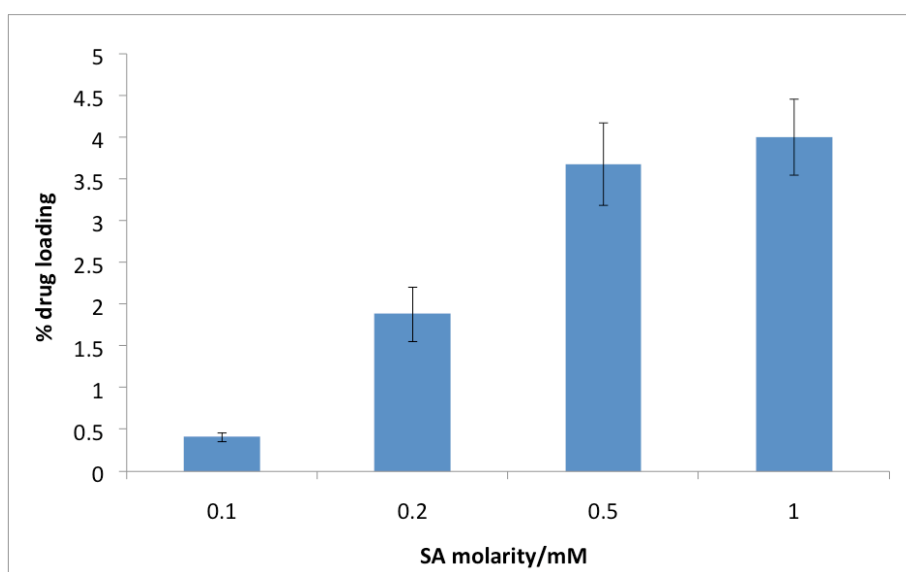
Figure 4- 7 Loading capacity of FF nanotubes as a function of SA concentration.

4.3.3 *In vitro* release of salicylic acid from diphenylalanine nanotubes

SA-loaded FF nanotubes were prepared in hard gelatin capsules for *in vitro* dissolution experiment, the weight of the drug-loaded capsule was 100 mg

±3.8. The bulk medium used was 0.1 M PBS (pH 7.4) at 37 ºC. Calibration of the UV to SA concentration was performed prior to the dissolution experiment. Five consecutive points of concentration were chosen and the data is plotted in Figure 4-8. The linear relationship presented between the concentration and the absorbance indicates a good level of linearity of the measurement (correlation coefficient = 0.999). During the dissolution, aliquots of the sample solution (3 ml) were taken at regular time interval (fresh medium was replaced into the beaker) and analyzed by UV-Vis spectroscopy at a wavelength of 296nm (as mentioned earlier, 296nm was used as the standard wavelength for SA). The experiment was repeated three times. The cumulative percentage release of SA from FF nanotube was studied and compared with that of free SA. Figure 4-9 represents the release curve of both free SA and tube-bound SA over a period of 2 hours. For free SA an initial rapid release was completed within a short-time period of about 10 minutes rapidly reaching over 80% release. FF tubes with SA showed a slight extended release with 77% released after 40 minutes.
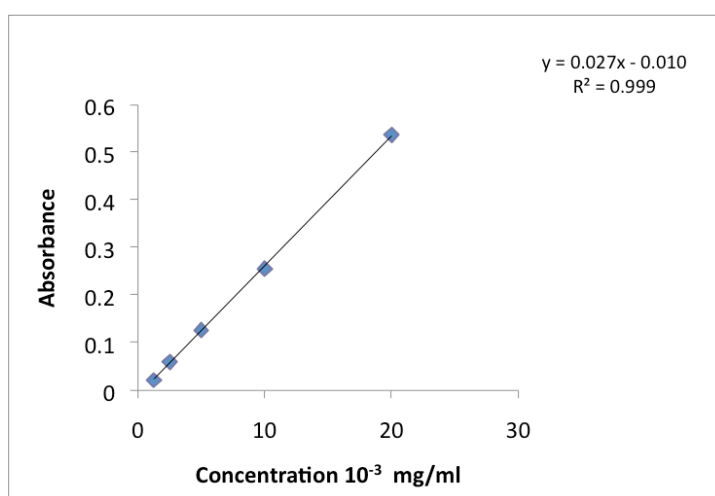
Figure 4- 8 Calibration line of SA
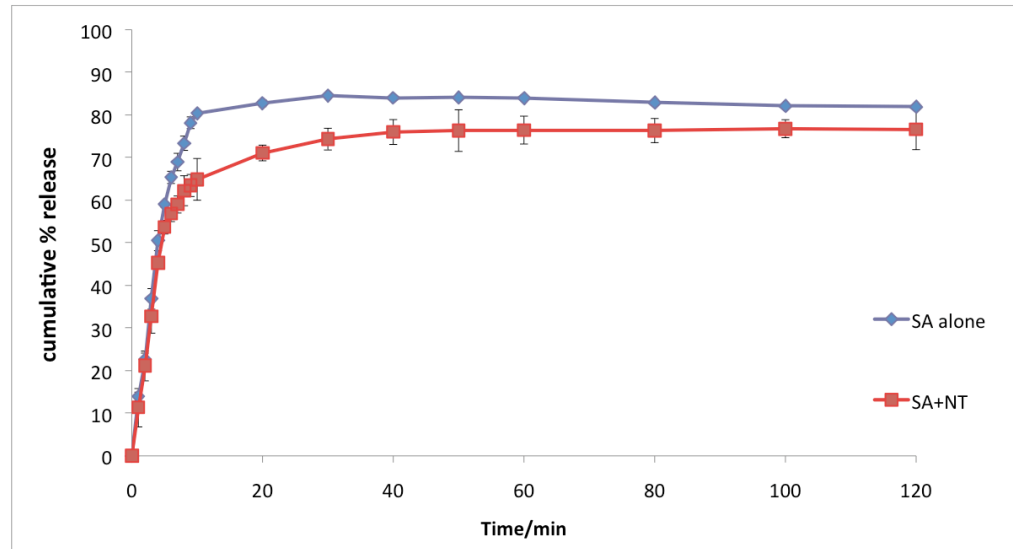
Figure 4- 9 Cumulative percentage release of salicylic acid with and without incorporation of FF nanotubes. The blue curve represents free SA release; the red curve represents FF tube-bound SA release. Data is presented as mean ± SEM (n=3).

4.3.3.1 Release model

Various models were applied to interpret the release process of salicylic acid from FF nanotube, including zero-order kinetic model, first-order kinetic model, Higuchi model and Korsmeyer - Peppas model [239].

The zero-order rate (Equation 4.1) describes a system where the drug release rate is independent of its concentration, where Q is the amount of drug released in time t, Q_o is the amount of drug present at t = 0, and k_o is zero-order rate constant expressed in units of concentration/time [239]. The kinetic is plotted as a function of cumulative percentage release of drug against time (Figure 4-10).

$$Q = Q_o + k_o t \qquad\qquad (4.1)$$

As presented, when describing the release of SA from FF tubes using zero order model, the release shows a two-phased pattern: the first 50% SA release shows a good linear relationship with a correlation coefficient (R^2) of 0.988. As more SA is being released, the slope of the line changed; the second part of the release can no longer be best described as zero order kinetics as the R^2 value drops to 0.844 which is relatively low.
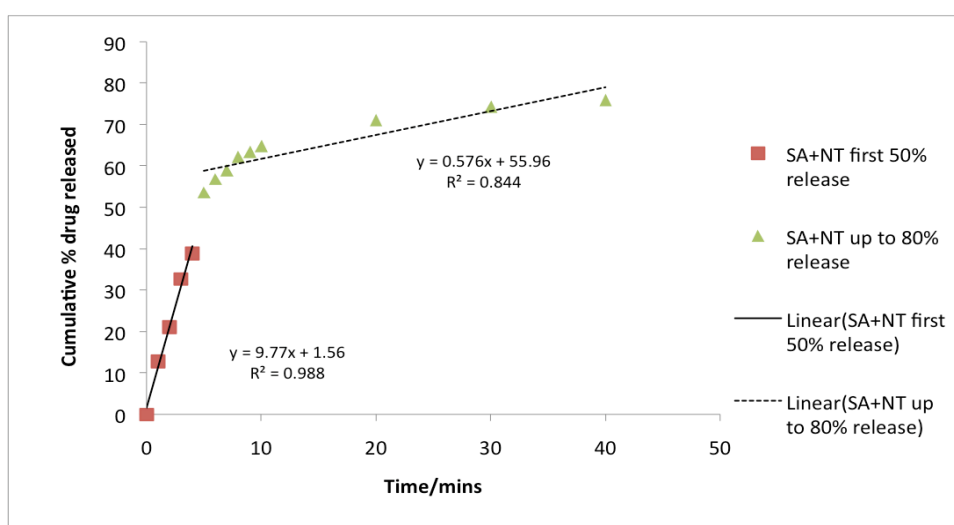
Figure 4- 10 Zero order release model of SA/FF nanotube.

The first-order model describes release from a system where release rate is concentration dependent (Equation 4.2), where Q_∞ is the total amount of drug in the matrix initial concentration of drug and k_1 is a first order constant [239]. By rearranging Equation 4.2, it can be expressed as the natural logarithm of the cumulative percentage of drug remaining versus time, i.e. Ln (Q_∞ - Q)=k_1t,

where Q_∞ - Q is the amount of drug remaining (Figure 4-11). Similar to the previous model, the figure still presents two distinct sections; one starts from t = 0 to t = 4 mins with a drug release up to 50 %, followed by a second phase with a different calculated equation and rate constant as the dissolution progresses. Compared to the data obtained from the zero order release, the first order model gives a slightly higher R^2 value of 0.995 for the first 50 % release, but a better R^2 value of 0.901 for the release from 50% to 80%.

$$Q = Q_\infty \left(1 + e^{-k_1 t}\right) \qquad\qquad (4.2)$$
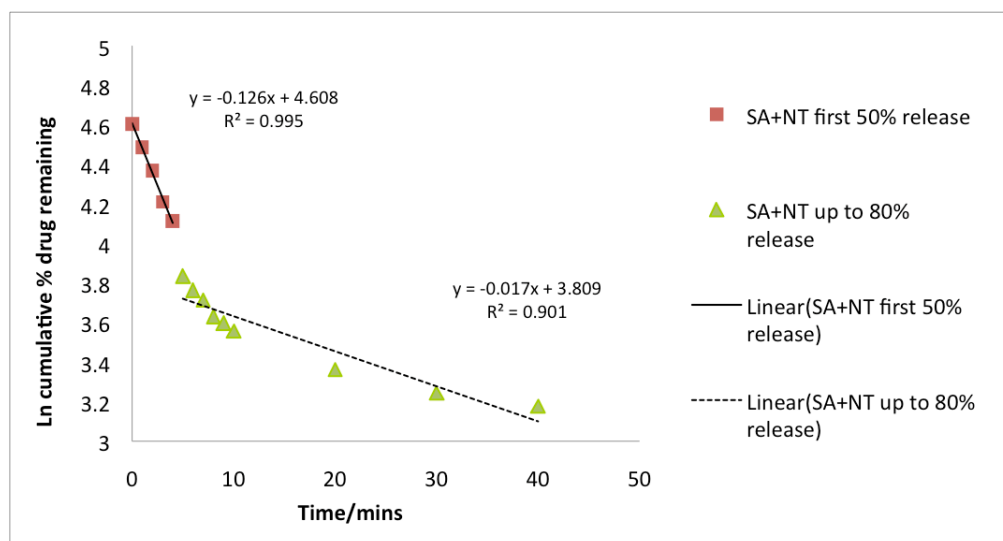
Figure 4- 11 First order release model of SA/FF nanotube.

Figure 4-12 represents the data presented using the Higuchi model which describes the release of a drug from an insoluble matrix as a square root of time dependent process based on Fickian diffusion (Equation 4.3), where k_H is the Higuchi rate constant [239]. The R^2 values of the two-phased drug release

pattern are 0.939 and 0.912, respectively.

$$Q = k_H t^{1/2} \qquad\qquad (4.3)$$
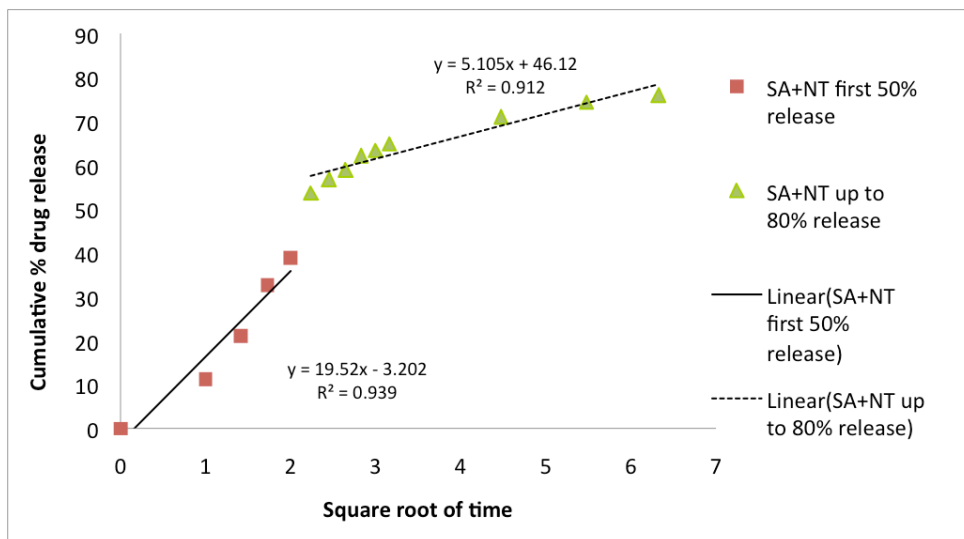
Figure 4- 12 Higuchi release model of SA/FF nanotube.

The final model used to study the release kinetics was Korsmeyer - Peppas model which describes drug release from a polymeric system (Equation 4.4) [239]. The first 60% of drug release data was fitted in Korsmeyer – Peppas model (Figure 4-13).

$$Q / Q_\infty = kt^n \qquad\qquad (4.4)$$

Where Q / Q_∞ is fraction of drug released at time t, k is the rate constant and n is the release exponent. The n value is used to characterize different release mechanisms for cylindrical shaped matrices. For n = 0.45, the release kinetics

is controlled by Fickian diffusion mechanism; for n =0.89, the process is described as a case II transport; if 0.45 < n < 0.89, it is a non-Fickian diffusion (i.e. mixture of Fickian and Case II diffusion); and for n > 1, the process is considered as a super case II transport [239]. For the present study, the n values for the first 50% drug release is 0.914, indicating the mechanism of release starts as a non-Fickian diffusion. The second phase drug release has an n = 0.282, which is beyond the theoretical lowest value of n (0.45). The possible reasons for this will be discussed in the discussion section.
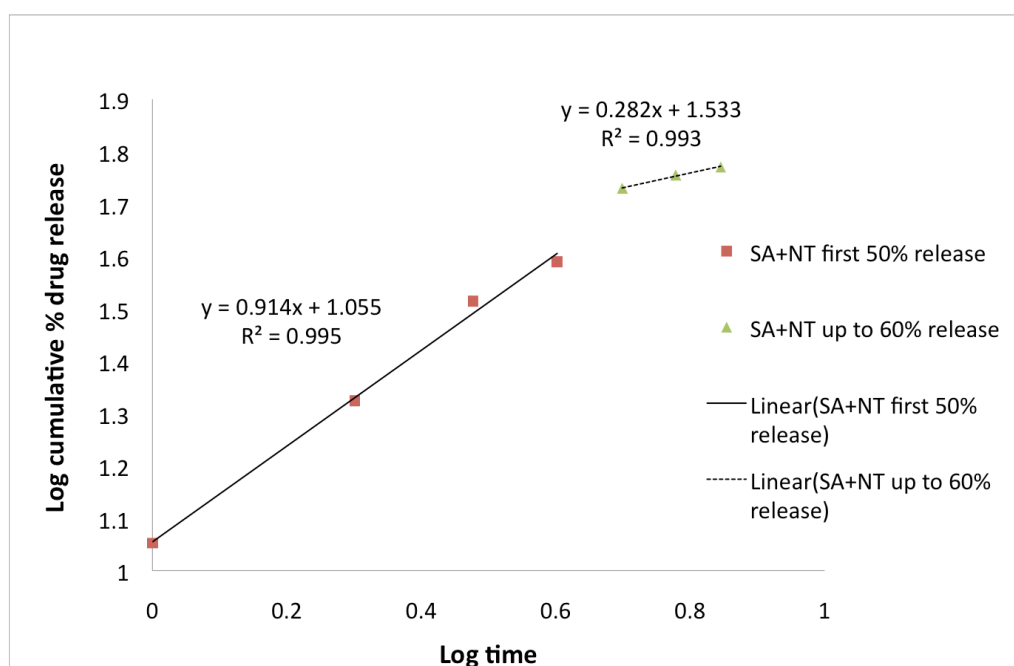
Figure 4- 13 Korsmeyer - Peppas release model of SA/FF nanotube.

A detailed discussion regarding the release mechanisms will be presented in later sections. A summary of all models with calculated equations and corresponding R^2 values is presented in Table 4.1.

Table 4. 1 Release models and parameters of SA/FF nanotubes.

	Sample: SA incorporated with FF nanotubes		
Kinetic Model	**Mathematical equation**	**Calculated equation**	**Correlation coefficient**
Zero-order	$Q = Q_o + k_0 t$	$Q = 9.77\ t + 1.56$ $Q = 0.576\ t + 55.96$	0.988 0.844
First-order	$Q = Q_\infty\ (1 + e^{-k_1 t})$	$\text{Ln}(1 - Q/Q_\infty) = -0.126t + 4.608$ $\text{Ln}(1 - Q/Q_\infty) = -0.017t + 3.809$	0.995 0.901
Higuchi	$Q = k_H t^{1/2}$	$Q = 19.52t^{1/2} - 3.202$ $Q = 5.105t^{1/2} + 46.12$	0.939 0.912
Korsmeyer -Peppas	$Q / Q_\infty = kt^n$	$\text{Log}Q = 0.914\text{Log}t + 1.055$ $\text{Log}Q = 0.282\text{Log}t + 1.533$	0.995 0.993

4.3.4 Characterization of 5FU-loaded diphenylalanine nanotube

Similar to the experiments performed on SA-loaded FF tubes, samples of FF nanotube with 5FU were characterized using SEM, UV-Visible spectroscopy, and XRPD.

4.3.4.1 SEM characterization of diphenylalanine nanotube with different 5- fluorouracil concentrations

Samples of 5FU-loaded FF nanotubes were prepared by mixing freshly prepared FF nanotube suspension with 5FU (dissolved in DMSO/water = 1:9) solution of different concentrations ranging from 0.1mM to 1mM. All characterization analysis was performed on air-dried samples (aged for 1 day) and the SEM micrographs of 5FU-loaded nanotubes are presented in Figure 4-14. Two controls were performed: SEM imaging of 5FU alone (Figure 4-14e) and FF tubes formed in the solvent without 5FU (Figure 4-14f). The image shown on the top left (Figure 4-14a) presents samples of FF tubes incorporated with 5FU at highest concentration: 1mM. Incomplete tubes were observed with pieces lined up. Figure 4-14b shows FF tubes with a reduced concentration of 5FU (0.4mM); fewer fragments were presented as compared with the higher concentration, nevertheless there were still portions of tubes observed. As the concentration of 5FU solution was further reduced to 0.2mM, more and more intact tubes were observed (Figure 4-14c). The circled highlights show the few broken tube pieces observed. Finally, at 0.1mM, the 5FU-loaded tubes appear to be long and intact with a diameter of 1-2 μm and a length up to hundreds of

micrometers (size measurement was performed on large number of tubes, n = 90. The experimental procedure was referred to the method listed in Chapter 2). For latter experiments, unless otherwise indicated, 0.1mM was chosen to be the fixed concentration of 5FU solution in all sample preparations.
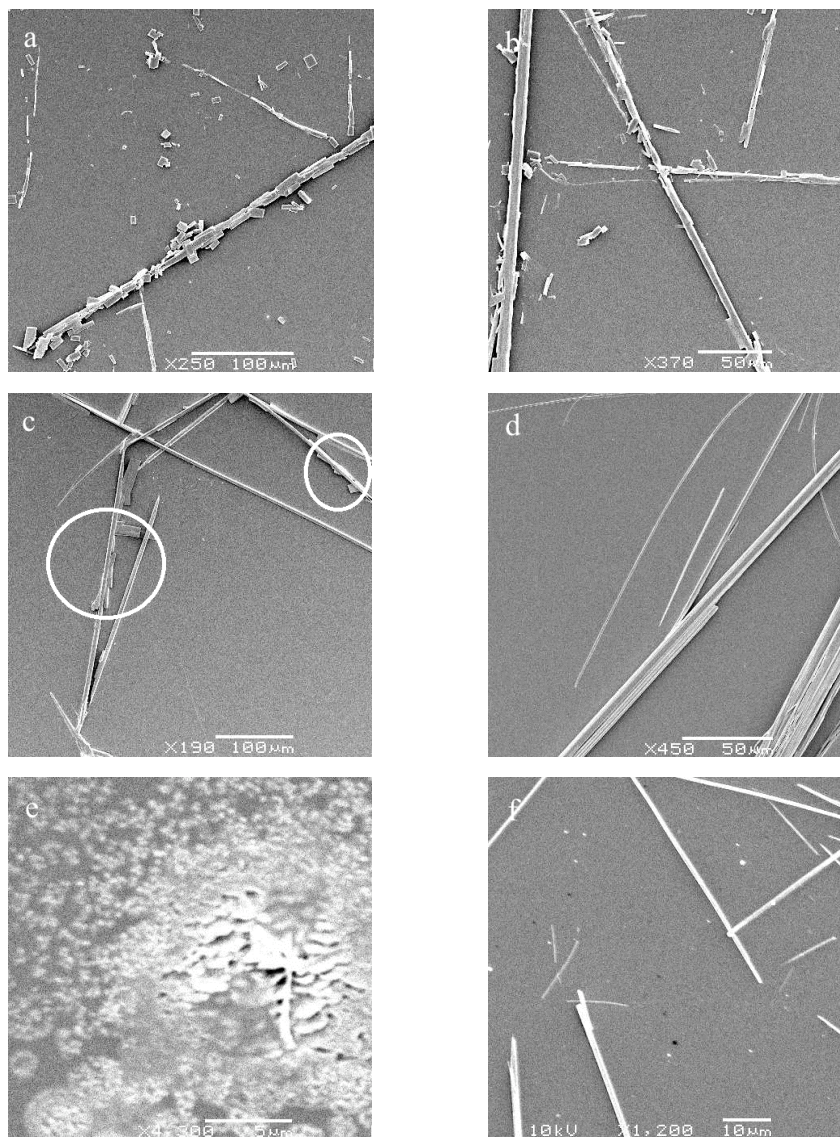
Figure 4- 14 SEM micrographs of FF nanotubes loaded with 5FU. 5FU is dissolved in a mixture of DMSO in water with a ratio of 1:9 with various concentrations (a) 1mM, (b) 0.4mM, (c) 0.2mM, (d) 0.1mM; image of 5FU alone is presented in 4-14e; bare FF nanotubes in DMSO/water = 1:9 without 5FU loaded is presented in 4-14f.

4.3.4.2 UV-Visible spectroscopy

UV-Vis spectroscopy was applied to samples of 5FU-loaded nanotubes and pure 5FU over a wavelength from 200 nm to 400 nm. As shown in Figure 4-15, a broad peak at 266 nm was observed for the spectrum of 5FU (Figure 4-15b), which is consistent with the published UV-Vis spectrum of 5FU [240]. On the other hand, the spectrum of 5FU-loaded FF tubes presents two characteristic peaks, one observed at 254 nm which was also found in the spectrum of SA-loaded FF tubes; and the other one was shown at 267 nm. For the 5FU release experiment, dissolution samples were analyzed at 266 nm.
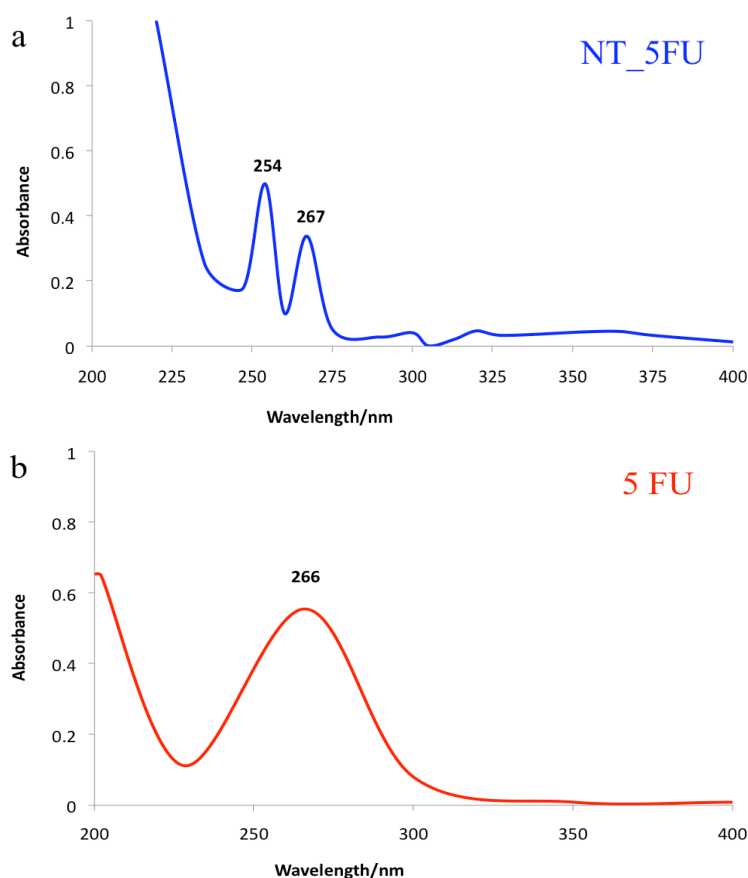
Figure 4- 15 UV-Vis spectra of FF nanotube/5FU and free 5FU. (a) FF tubes loaded with 5FU, and (b) spectrum of 5FU alone. Peaks of interest are presented.

4.3.4.3 Powder X-ray diffraction

Similar to the previous XRPD experiment applied on FF tubes and FF tube/SA mixture, samples of FF tubes with and without 5FU loaded were analyzed by XRPD to identify differences regarding the molecular arrangement of FF tubes. The patterns are presented in Figure 4-16 with the spectrum representing 5FU-loaded tubes shown in 4-16a and the spectrum representing tubes alone shown in 4-16b. The two patterns show little or no difference with good alignment, indicating that the molecular packing of the tubes with or without drug was similar.
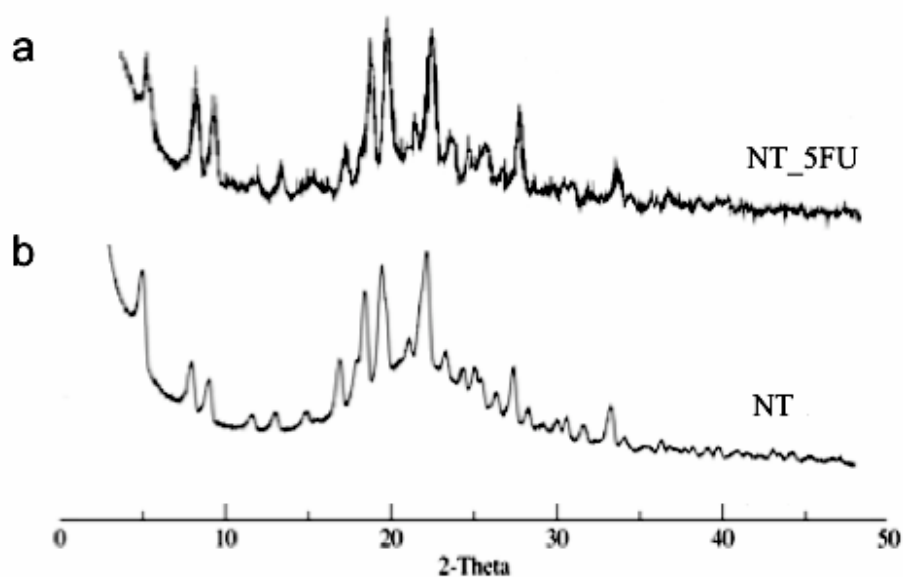
Figure 4- 16 XRPD patterns of FF nanotubes with and without 5FU loaded. (a) drug-free FF tubes, and (b) 5FU-loaded FF tubes.

4.3.4.4 5-fluorouracil loading capacity

In order to search for the influence of 5FU concentration on the drug loading capacity of FF tubes, samples of tube suspensions were mixed with 5FU solution with different concentrations ranging from 0.1mM to 1mM. As shown in Figure 4-17, when the concentrations of 5FU solution increases from 0.1 to 0.4mM, the drug content increases rapidly from 0.82 % to 3.34 % after 24 hours incubation time. The percentage rise in drug loading slows down with further increase in 5FU concentration; at 1 mM the drug content is 3.59 %. This finding is consistent with that of the SA loading capacity (Figure 4-7), which may indicate a possible saturation loading of the FF tubes before their assembly is unduly affected. Again, the SEM imaging of FF tubes loaded with 5FU with different concentration confirms this suggestion; FF tubes appeared to be disassembled at high 5FU content (Figure 4-14).
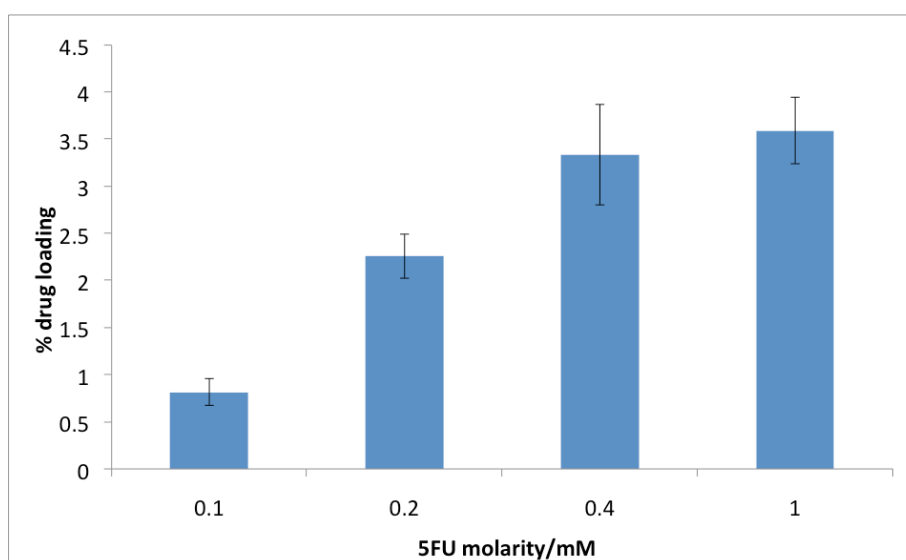
Figure 4- 17 The loading capacity of FF nanotubes as a function of 5FU concentration.

4.3.5 *In vitro* release of 5- fluorouracil from diphenylalanine nanotubes

A dissolution study was carried out with FF tubes loaded with 5FU; dried samples of drug-loaded tubes were prepared in hard gelatin capsule (weight of the drug-loaded capsule is 100 mg ±5.7). The medium used was PBS (0.1 M, pH 7.4) at 37 °C and the experiment was repeated three times. Samples of pure 5FU loaded capsules were also prepared and their release was compared with that of the tube-drug mixture. Calibration of 5FU was performed prior to the experiment and is shown in Figure 4-18. Five points of concentration were chosen and the corresponding absorbance was measured at 266 nm (i.e. the max. absorbance wavelength as determined from the previous UV-Vis spectroscopy spectrum of 5FU). The calibration appears linear with a correlation coefficient of 0.999. The *in vitro* dissolution of 5FU released from FF tubes was compared with that of the free drug. Cumulative percentage release of 5FU over a period of 2 hours is presented in Figure 4-19. The release of free drug appears to be rapid; it reaches over 80% within first 10 minutes and remains around 80 %. In contrast, the release of drug from FF tubes presents a delayed profile; the whole curve is shifted down and to the right, indicating a slower drug release with a lower overall percentage release in the time studied. It appears to be a quick release from the beginning up to 10 minutes reaching almost 50 %, and gradually slows down. The release is completed at around 80 minutes with an overall 62 % drug release.
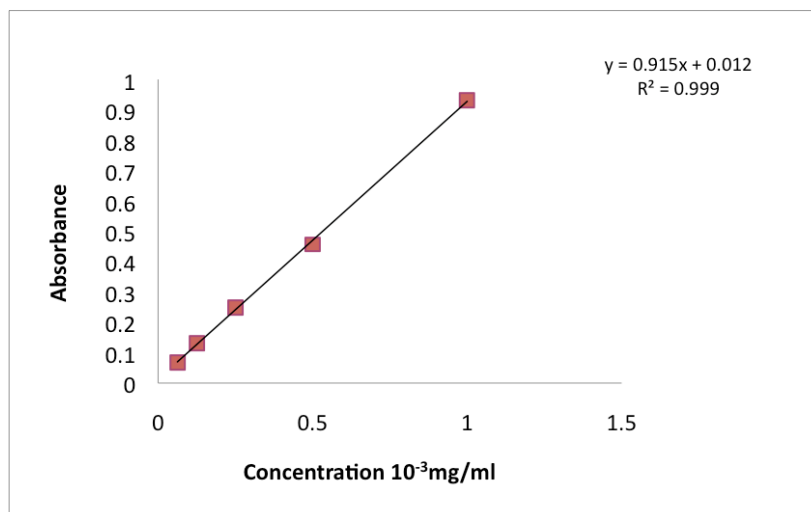
Figure 4- 18 Calibration of 5FU
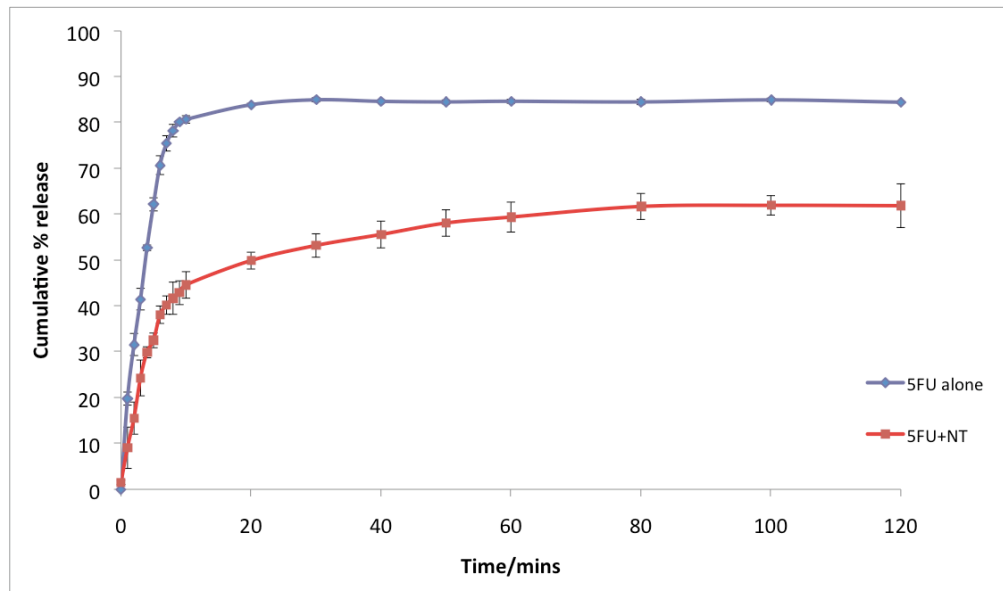
Figure 4- 19 Cumulative percentage release of 5FU with and without incorporation of FF nanotubes. The blue curve represents free drug release; the red curve represents FF tube-bound 5FU release. Data is presented as mean ± SEM (n=3).

4.3.5.1 Release model

As for the mathematical evaluation applied to SA release from FF tubes, kinetic models were used to analyze the release profile of 5FU from FF tubes.

The zero order kinetic model of 5FU release from FF tubes is shown in Figure 4-20. Since the drug release appeared to be completed at t = 80 minutes, all data obtained within 80 minutes was used to generate the fit. A two-phased drug release behaviour is apparent in Figure 4-20; the first linear part (red dots) is up to 50 % drug release (R^2 = 0.987), and the second part (blue points) comprises the remaining release up to a final 60 % (R^2 = 0.908). The figure appears similar to that of the SA release, which also showed a two-phased release pattern.
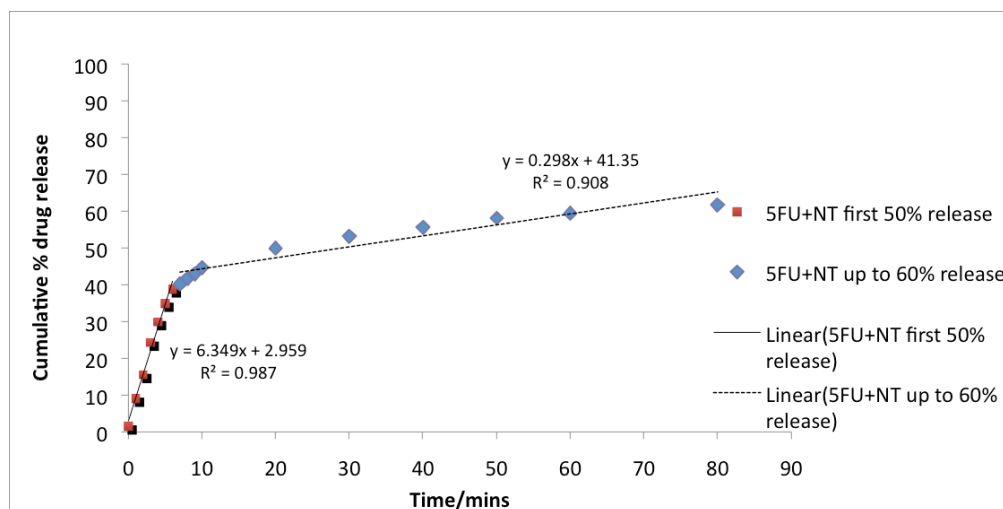
Figure 4- 20 Zero order release model of 5FU from FF tubes.

The first order release model of 5FU released from FF tubes is presented in Figure 4-21. The release as described using first order model generates better

fit than the zero order model with correlation coefficients of 0.995 and 0.937 for the two phases, respectively.
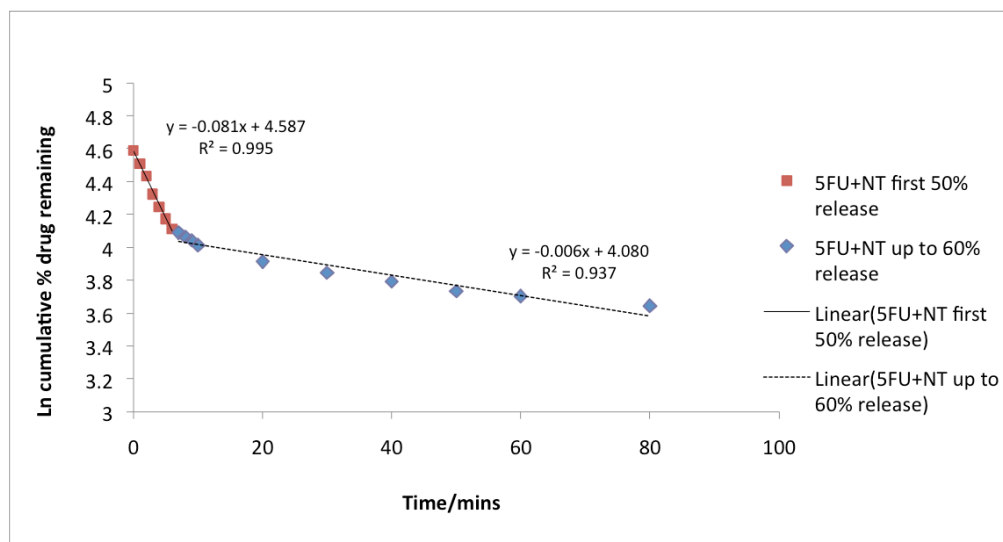
Figure 4- 21 First order release model of 5FU from FF nanotubes.

The release data is also applied to Higuchi model (Figure 4-22). Linear progression of the plotted data shows a correlations values of 0.943 for the first 50 % release and 0.973 for the release between 50 – 60 %.

Finally, the Korsmeyer-Peppas model is presented in Figure 4-23. The drug release is considered to be best described using this model as indicated by the highest R^2 value; linear regression analysis of the data yields the equations of best line as y = 0.834x + 0.959 and R^2 = 0.993 and y = 0.177x + 1.463 and R^2 = 0.993, where y = LogQ, and x = Logt (Equation 4.4). According to the equation, the slope of the line corresponds to the exponent n. Therefore, n = 0.834 indicates a mixture of Fickian and Case II diffusion kinetics for the first

50% drug release; and a second value of n = 0.177 indicating a diffusion that may not be described as Fickian.
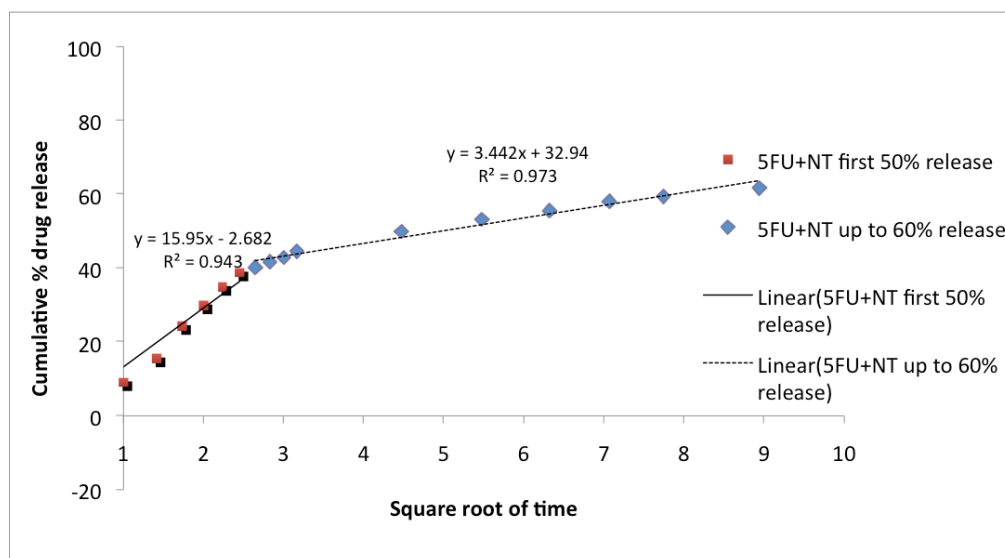
*Figure 4- 22 Higuchi model of 5FU released from FF tubes.*
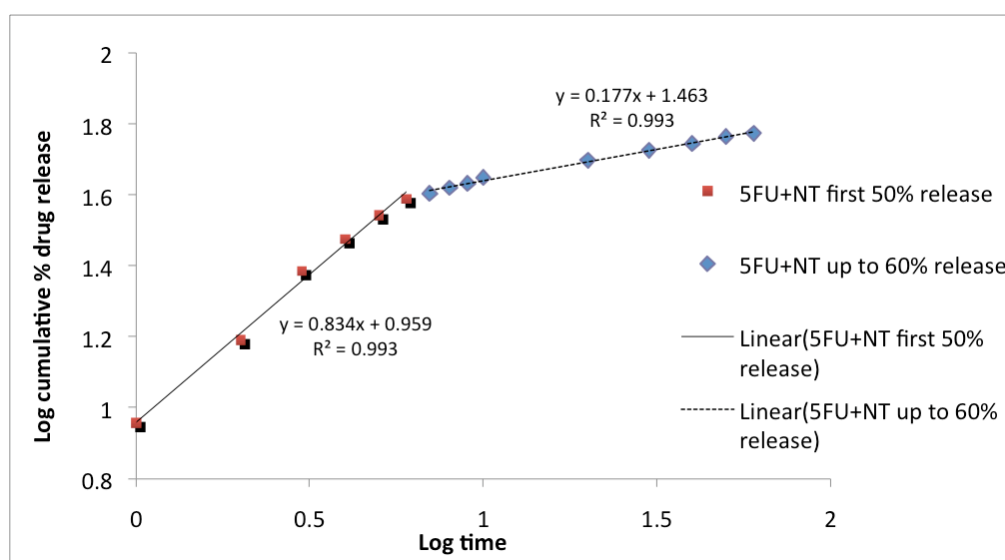
Figure 4- 23 Korsmeyer-Peppas model of 5FU released from FF tubes.

A detailed discussion regarding the release mechanisms will be presented later in section 4.44. A summary of all models with calculated equation and corresponding R^2 values is presented in Table 4.2.

Table 4. 2 Release models and parameters of 5FU/FF nanotubes.

Sample: 5FU incorporated with FF nanotubes			
Kinetic Model	**Mathematical equation**	**Calculated equation**	**Correlation coefficient**
Zero-order	$Q = Q_o + k_o t$	$Q = 6.349\ t + 2.959$ $Q = 0.298\ t + 41.35$	0.987 0.908
First-order	$Q = Q_\infty\ (1 + e^{-k_1 t})$	$\ln(1 - Q/Q_\infty) = -0.081t + 4.587$ $\ln(1 - Q/Q_\infty) = -0.006t + 4.080$	0.995 0.937
Higuchi	$Q = k_H t^{1/2}$	$Q = 15.95t^{1/2} - 2.682$ $Q = 3.442t^{1/2} + 32.94$	0.943 0.973
Korsmeyer -Peppas	$Q/Q_\infty = kt^n$	$LogQ = 0.834 Logt + 0.959$ $LogQ = 0.177 Logt + 1.463$	0.993 0.993

4.4 Discussion

The work presented in this chapter focuses on the investigation of drug-loaded diphenylalanine peptide nanotube and the evaluation of its potential as drug carrier for two model drugs: SA and 5FU. The first section deals with the successful preparation of drug-nanotube mixtures; different drug concentrations and solvents were chosen and SEM characterization was performed. The SEM images presented of drug-FF tube samples prepared with various drug concentrations and solvents suggest the possible influence of these two factors on FF tube self assembly as evident from the change of tube morphology with the corresponding change of factors (Figure 4-3, 4-4, and 4-14). Drug loading analysis was also applied to study the relationship between drug loading capacity of FF tube and drug concentration. From the figures presented it can be seen that the drug content rapidly increases with initial increase of drug concentration, and then stays at the same percentage; further concentration increase does not affect the drug loading capacity, which suggests a possible saturation loading for each drug (Figure 4-7 and 4-17). Furthermore, the UV-Vis spectroscopy spectra of the drug/FF tube (after centrifugation, so all loose drugs were removed) show the appearance of both a phenylalanine peak at 255/254 nm and peaks of the corresponding drug, which again indicate successful drug incorporation (Figure 4-5 and 4-15).

In vitro release study of the chosen drugs from drug-tube complex using a dialysis method was performed in the second section of this chapter; free drug release was also conducted for comparison. As presented in the cumulative

percentage release figures, both drugs released from the tube show a delayed profile and a lowered overall release percentage as compared with the free drug release (Figure 4-9 and 4-19). To investigate the kinetics involved in the release of each system, four different models were applied and the most suited one was Korsmeyer-Papps model for both drugs (as indicated by the highest R^2 value). It is suggested that there might be two different kinetics involved in the release of both drugs with the first 50% drug release is governed by a mixture of case II transport and Fickian diffusion. A detailed discussion regarding drug release mechanism will be presented in a later section (section 4.44).

4.4.1 Influence of drug concentration on diphenylalanine tube formation

The effect of drug concentration on FF tube formation was investigated for both SA and 5FU. It should be noted that 'drug concentration' does not equate to 'drug loading'. The result obtained from the drug loading experiment has shown that it is a non-linear relationship between drug loading capacity and drug concentration.

The SEM images of FF tubes formed in drug solutions of different concentrations suggest an inverse relationship between the tube formation and drug concentration; as the drug concentration is increased, fewer tubes are observed. This observation may be explained in such a way: If we consider FF tube self-assembly process as a nucleation-dependent process [241, 242]; after reaching the critical peptide monomer concentration, nanotube self-assembly

occurs, the growth of the tube continues until it reaches equilibrium with free peptide in solution. Since the equilibrium between peptide monomers and tubes is influenced by a number of factors, such as temperature, pH, solvent, addition of other ions [105, 106, 114, 243], it is not surprising that the addition of drug molecules would disturb the delicate balance between nanotubes and peptide monomers (Figure 4-24).

The precise reason why increased drug concentration would disfavour FF tube assembly is not yet understood. As mentioned earlier, it is probably due to altering the equilibrium between peptide monomer and assembled nanotube. From our data only tentative suggestions can be made based on knowledge of the tube structure. It is known that the assembled tubes have a molecular structure that comprise 6 FF molecules per turn, which arrange to form an inner core composed of hydrophilic peptide bonds and an outer shell composed of hydrophobic aromatic groups. The tubes are hence stabilized by a number of molecular interactions including π-π interactions between the aromatic groups of FF of adjacent β-sheet and inter / intramolecular H-bonding [96]. Therefore, any change that disrupts the balance of hydrophobic and electrostatic interactions would have an effect on tube structure, directing the equilibrium towards the monomer state. SA and 5FU both contain an aromatic ring and polar groups such as hydroxyl groups. They are hence good candidates for drug incorporation, but also may act as competitors of tube assembly. FF, SA and 5FU molecules are comparable in terms of molecular weight (i.e. 138, 312 and 130 g/mol, respectively); all three have flat molecular structures with similar functional groups. Although the specific location of binding of these two drug

molecules is not known; whether most of them bind to the inner hydrophilic channels of the tube or intercalate into the hydrophobic shell remains unclear. Nevertheless, it is reasonable to propose that these molecules may interrupt tube assembly via a replacement process if present in sufficient quantity. A tentative model of drug/FF tube binding is shown in Figure 4-25. Moreover, based on this assumption, the difference between the concentration limits found for 5FU (0.2mM) and for SA (1mM) may be explained. 5FU molecule contains two cyclic amide bonds, which are more polar than the two hydroxyl groups presented in the SA molecule. Hence, 5FU would be a better competitor against FF in terms of tube formation; tubes are less stable in presence of 5FU than SA at the same drug concentration. More investigations are required to investigate this model, such as further structural and spectroscopic characterization of the tube/drug complex and construction of a thermodynamic model of drug loading based on various energy terms are needed.
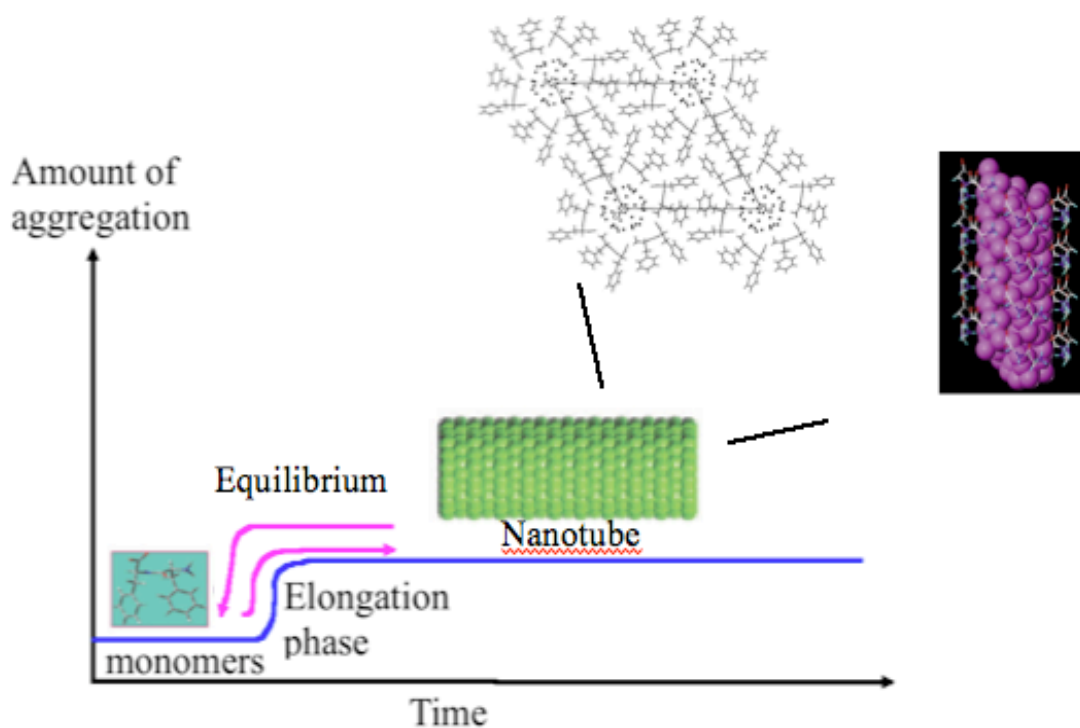
Figure 4- 24 Schematic representation of the nucleation-dependent FF tube formation. The molecular packing of the tube is shown on the top and a side-view of the tube is shown on the right. The black dots and the purple cluster represent the water molecules inside of the tube. (The molecular arrangement and tube model are adapted from ref. [96]).
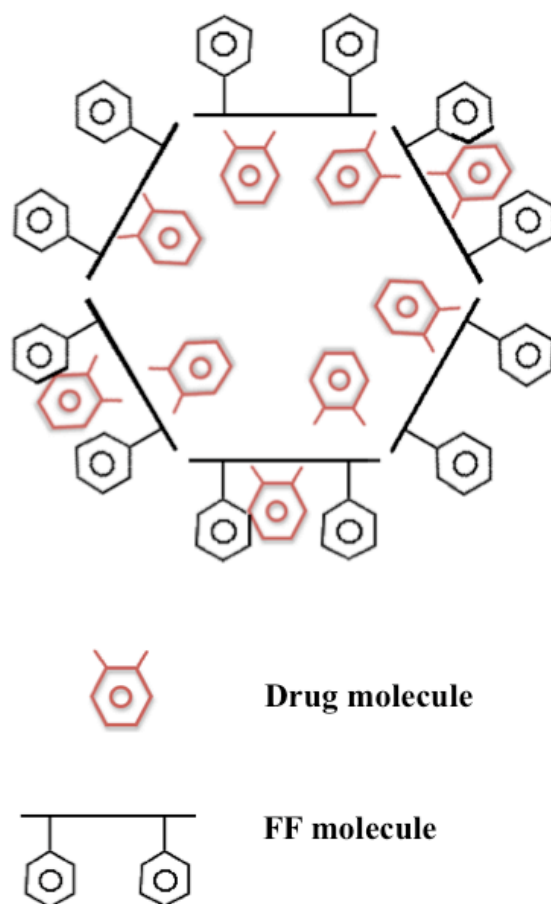
Figure 4- 25 Schematic representation of drug-loaded diphenylalanine nanotube. The drug molecule shown in the figure represents the class of molecules with an aromatic ring attached to hydrophilic groups (SA and 5FU both fall into this class). The straight lines for simplicity represent peptide bonds and other hydrophilic groups. The nanotube is viewed from the top.

4.4.2 Influence of solvent on diphenylalanine tube formation

Ethanol is less polar than water with a dielectric constant of 24.3 at 25 °C [244]. A number of workers have investigated the effect of ethanol on protein folding, showing the ability of ethanol as a disrupting agent through its changing of hydration forces and promotion of protein unfolding and consequent fibrillization [245-248]. Ethanol has also been applied to pre-formed amyloid fibrils and shown that high ethanol concentrations at around 30% can disassemble pre-formed fibrils [249]. Another study performed on pre-formed FF peptide nanotubes showed that after the addition of few aliquots of pure ethanol, FF tubes disappeared under optical microscopy. This disappearance was accompanied by an increase of FF peptide concentration suggesting dissolution of the FF nanotubes [250]. The work presented in this chapter is consistent with these findings. The introduction of ethanol as a co-solvent affects the tube formation as reflected in the SEM images; at 40% v/v (i.e. ethanol/water = 2:3) or above, no tubes were observed. Furthermore, the percentage of ethanol/water seems to play an important role regarding the morphology of the assembled structures. SEM images of the samples prepared in different proportions of ethanol, show that the morphology of the assemblies changes from thin fibrils to tubes with a wider diameter and longer length. This further supports previous published results: introducing ethanol to FF tube suspension as a co-solvent reduces the polarity of the solution. As a result, this weakens hydrophobic interactions and hydrogen bonding, leading to reduced tube formation. If substantial amounts of ethanol are applied, this may destabilize tube formation. Less ethanol may not be sufficient to dissolve pre-

formed tubes, but still affect the morphology of the assemblies resulting in thinner and shorter fibrils are formed compared to the native FF nanotubes (as presented in Figure 4-4).

4.4.3 Relationship between drug loading capacity and drug concentration

The drug loading capacity of FF tube was investigated as a function of drug concentration. It is found that the drug content increases with increased concentration for both SA and 5FU. The relationship is not directly proportional; when SA concentration increases from 0.5mM to 1mM, the drug loading varies little from 3.67% to 4.00%; when 5FU concentration increases from 0.4mM to 1mM, the drug loading changes from 3.34% to 3.59%. The nonlinear increase of drug content with concentration for both drug models may be attributed to the spontaneous deposition of drug molecules into/onto FF tubes. As previously mentioned in the result section (section 4.3.1), the rationale behind choosing SA and 5FU as candidate drug molecules was because of their capability of forming hydrogen bonding and π-π interactions with FF nanotubes. The non-proportional drug loading may reflect the spontaneous nature of drug-tube interactions. As the drug concentration increases, the chance of drug molecules to attach onto/into FF tube is increased, but the exact percentage loading content is random. As a result, the drug loading percentage may vary from batch to batch even if the concentration is kept constant. It is therefore essential to calculate drug loading

for each experiment for accuracy. The random drug loading found here is indeed supported by a number of published studies on other carrier-based delivery systems for drugs such as 5FU [251]. For the case of 5FU, a study was performed poly (L-glutamic acid) / chitosan microcapsules containing 5FU. The percentage drug content was also found to increase nonlinearly with increased drug concentration, and spontaneous drug accumulation was suggested to be a result of the random hydrogen bonding interactions between the drug molecule and the carrier [251].

4.4.4 Drug release from FF nanotube

The cumulative percentage release of both SA and 5FU from FF nanotubes shows a delayed behaviour as compared with that of the free drug. To further analyze the release kinetics, different models were employed. As presented from the results, both drug/tube complexes exhibit a biphasic release behaviour; the first segment appears to be from the beginning up to ~50% drug release (between t = 0 to t = 4 mins for SA, and between t = 0 to t = 6 mins for 5FU release) and the second phase follows from ~50% to the end of the release. The distinct two-phased release pattern displays an apparent break point in which the slope clearly changes in all cases; evidently there are two separate release kinetics involved in drug/FF tube *in vitro* dissolution process.

The biphasic release kinetics observed may result from the complicated nature of FF nanotube as drug carrier; it is unlike the common matrix systems such as hydrogels as apparent polymer swelling does not occur; it is also different from

the non-swelling matrices, because it may present some degrees of polymer relaxation during dissolution. Considering a system of drug molecules presented in a dry nanotube, three factors need to be taken into consideration: firstly, free drug molecules that were not bound to FF tubes have been removed by centrifugation (assuming complete removal); secondly, the location of drug-FF binding is unknown (could be intercalated with the tube or inside of the core), and thirdly, the loading is spontaneous as previously discussed. Upon contact with the release medium (PBS), the self-assembled FF chains may experience some level of microscopic rearrangement and drug dissolution can take place. The time required for the rearrangement (t_r) and for the drug to diffuse out (t_d) may vary according to different delivery systems. For a system with t_r that is similar to t_d, the solvent adsorption does not follow Fick's law of diffusion, thus the release becomes anomalous and is generally considered as a mixture of Fickian diffusion and case II transport [252, 253]. From the results presented here, anomalous diffusion with a first ordered rate kinetics modulates the initial release of both SA and 5FU from FF tubes (as indicated by the highest correlation coefficient); from 0 % to ~ 50 %, the diffusion of drug molecules and the relaxation rates of FF chains are comparable. The second phase presented suggests that the mechanism clearly changes during the course of delivery for both drugs. It is difficult to find the best model that fits the second phase release; the correlation coefficient values of all models applied are low. The Korsmeyer model shows that the exponent value n are less than 0.45 for both systems (0.282 for SA and 0.177 for 5FU), indicating the release is an almost-Fickian diffusion as the lowest n value for a Fickian diffusion is

0.45 in theory. Various drug delivery systems with a diffusion exponent value that is less than 0.45 are found to be common and have been largely reported to date [254, 255]. The release is generally described as 'quasi Fickian diffusion'. The suggestive causes are varied according to different systems but usually comprise unavoidable experimental errors. Nevertheless, Fikian and quasi-Fickian diffusions are considered to be similar in nature, the rationale behind these processes are treated as identical. In the present study, the second phase release is sustained as compared to the first phase and is found to be a quasi-Fickian diffusion. The change of release mechanism could be resultant from tube stabilization, i.e. the microscopic rearrangement of FF chains may slow down after a period of relaxation, so the time it takes for further chain rearrangement is longer. In which case, t_r becomes greater than t_d from 50% to 60% drug release, which indicates FF chain relaxation outweighs the drug diffusion, therefore drug release is slowed down the solvent adsorption with a constant diffusitivity takes place.

The 'biphasic release behaviour' has been observed in various delivery systems from published papers [256-258]. The exact cause of the study presented here is unknown. It could be due to a number of factors, such as the random drug distribution, which is well known to heavily affect drug release kinetics for other delivery systems [259-261]. Additionally, drug molecules that bound to the tube surface may diffuse at a faster rate than those bind to the interior core of the tube, which may give rise to a burst effect in the release profile followed by a slower release.

4.5 Conclusions

The work presented in this chapter is an evaluation of the potential of diphenylalanine peptide (FF) nanotube in drug delivery as a drug carrier. Successful synthesis of two model drug, salicylic acid (SA) and 5-fluorouracil (5FU) loaded FF tubes in various drug concentration and solvents has been demonstrated and characterized by SEM imaging, which has shown FF nanotube self-assembly is a drug concentration and solvent type dependent process. Other characterizations using a combination of UV-Vis spectroscopy and XRPD have shown similar molecular packing arrangement between drug-loaded and native FF tubes. The drug loading capacity of FF tubes showed an indirect relationship with the drug concentration, which has indicated a spontaneous random binding between FF tube and drug molecules. Finally, *in vitro* release experiment of both drugs from FF tubes were performed and compared to that of the bare drug. Extended release profiles have been achieved in both cases with an initial phase controlled by a mixture of Fickian and case II diffusions.

Chapter 5 General Conclusions and Future Directions

The work presented in this thesis has focussed on a dipeptide, diphenylalanine (FF), which is the core-recognition motif of β–amyloid polypeptide. Beside the key role it plays in β–amyloidogenesis, FF has attracted interest in nanotechnology due to the physical and chemical stability and mechanical rigidity of the self-assembled nanotube form of the peptide. A number of promising applications of FF nanotubes have been previously explored. However, the work presented here has provided new insights to this area: a comparative characterization of FF nanotubes prepared by different methods has shown the diversity in tube morphology observed, which has led to the suggestion of the mechanism of FF tube self-assembly. Furthermore, successful synthesis has been applied to form drug-loaded nanotubes. The investigation of the potential of FF tubes as a drug carrier in drug delivery has shown promising result of extended drug release, particularly for 5FU dissolution. Taken together, pivotal to this work is to provide more knowledge of FF peptide nanotubes from both physical and biological prospects.

In the introductory chapter of this work, an overview of the current understanding of FF assembly, characterization and properties has been presented. The assembled FF-based nanostructures, together with applications in the areas of both non-biological and biological have been introduced. The closing of the first chapter has presented the aim and objectives of this thesis.

The first experimental study presented in Chapter 2 addressed the self-assembled FF nanotubes by different methods of preparation. Although this dipeptide has been extensively studied for its chemical and physical properties, no such parallel comparative investigations have been carried out on the formed tubes prepared using different methods. The work presented here for the first time evaluated the differences found regarding the physicochemical properties of FF tubes of different types of preparation utilizing a number of techniques such as atomic force microscopy (AFM), scanning electron microscopy (SEM), Raman spectroscopy and x-ray powder diffraction (XRPD). The tubes assembled in water alone at 65 °C displayed long, straight and unbranched morphologies that are in agreement with those previously observed by SEM; the ones formed in the mixture of 1,1,1,3,3,3-hexafluoropropan-2-ol and water appeared differently. Apart from the dissimilarities in morphology observed, variation of the size distribution performed on large number of tubes was also revealed. These findings led to the suggestion of the differences in the mechanisms of tube growth under different conditions, but that the endpoint in terms of molecular architecture is the same as revealed by XRPD. To further investigate the nucleation and growth of FF nanotube self-assembly in the future, selective photosensitizer molecules (e.g. 4-acetylbiphenyl and benzophenone) and lanthanide ions (which are luminescent materials widely used in optoelectronics such as laser) could be chosen to incorporate into the tube assembly. The formation and growth of the tubes could be studied by time lapse optical microscopy with a filtered UV illumination. Indeed, a recent study has successfully incorporated

lanthanide ions such as terbium and europium with FF tube and produced photoluminescent peptide nanotubes [131, 132, 134].

Some of the criteria that must be fulfilled before evaluating the applications of FF nanotube in the pharmaceutical field are biocompatibility and biodegradability. Other material-based drug delivery systems, such as many types of synthetic polymer-based materials have restricted applications because of the immunogenic reactions from the body as a result of the questionable biodegradability. FF-based nanostructures present several advantages such as ease to fabricate with low cost, and biocompatibility and biodegradability. Studies have shown that FF nanotubes can easily be degraded by proteolytic enzymes such as proteinase K, which is also an essential step in metal nanowire fabrication. The expected biocompatibility of FF nanotubes, however, has little published information; limited cell-based work has been carried out to investigate the biological properties of FF nanotubes. Therefore it is crucial to have an improved understanding of FF nanotube cytotoxicity.

The experiments within Chapter 3 have focused on the biological properties of FF nanotubes; the cytotoxicity has been assessed on a HeLa cell line using a MTT colorimetric assay. Different factors that may influence the cytotoxicity have also been investigated, including different methods of preparation, peptide concentration, nanotube solution concentration, presence of HFIP that is known to be a cytotoxic solvent, and presence of serum in cell culture medium. The results have shown that the tubes prepared by both methods did not cause toxicity related damage to HeLa cells at different peptide concentration (10 μg/ml and 1000 μg/ml), and at different dilution of pre-

formed tube suspension (from 1000 μg/ml to 31.65 μg/ml). The toxic HFIP was removed by evaporation of HFIP/water mixture at 65 °C overnight. HFIP on its own has shown a highly toxic effect on HeLa cells with over a 90 % decrease in cell metabolic activity. Finally, serum was found to have a protective effect on the cells. Cells had a greater metabolic activity and the toxicity caused by HFIP was reduced when in presence of serum. Moreover, cells in a nanotube-culture medium suspension were studied by total internal reflection microscopy and successful images of time-lapse study were captured to show the presence of nanotubes inside the cells. Although the specific cellular uptake pathway is yet to be determined, based on the size of the tubes found, macropinocytosis is the suggested uptake pathway. Whilst cell-based studies cannot necessarily be extended to the *in vivo* case, these observations clearly do not rule out the potential applications of FF nanotubes to the pharmaceutical and biomedical areas. In the future, more cell lines and more cytotoxicity assays (such as neutral red uptake and lactate dehydrogenase release assay) could be performed to fully evaluate the cytotoxic property of FF nanotubes. Moreover, considering the size of an average cell that ranges from few microns to around 100 microns, nanotubes with lengths that are less than 100 μm are particularly of interest for applications such as potential drug carriers (as presented in Figure 3-10, small tubes inside of HeLa cells were also observed from TIRM images; furthermore the time lapse TIRM video provided in the Appendix B also showed the movement of short tubes acrossing HeLa cell membrane). Based on these considerations, more knowledge regarding the

cytotoxicity property of short tubes is needed to further explore the potential of FF tubes in biological and pharmaceutical applications.

Based on the results obtained from the previous two chapters, which have provided improved knowledge in terms of the physicochemical and cytotoxicity of FF nanotubes, Chapter 4 investigated FF nanotubes as carriers in drug delivery. The studies presented in Chapter 4 can be categorized into two sections: first involves the synthesis and characterization of drug-loaded FF tube complex, next is the evaluation of drug release from nanotubes utilizing an *in vitro* dissolution experiment.

Two model drugs were selected based on careful considerations: salicylic acid (SA) and 5-fluorouracil (5FU); both of which have been well studied and have a structure of a planar aromatic ring linked with functional groups such as hydroxyl and amide groups that are capable to form hydrogen bonding and aromatic interactions with FF nanotube. The preparation was simply achieved by mixing pre-formed FF tube solution with drug solution. The relatively stratight forward synthesis presents the advantage of FF nanotube-based drug delivery system in terms of ease production with low cost. Characterization of drug-loaded FF nanotubes using SEM has revealed a morphological change of the assemblies as a consequence of varying drug concentrations and solvent mixtures. Conjecture of the rationale behind it was made, in which FF self-assembly is considered as a dedicate equilibrium process between monomer concentration and tube formation. Factors that disturb the interactions involved in tube assembly may influence the tube formation and also the stability of the formed tubes. This suggestion is consistent with published work on FF

nanotubes. To further study the physical properties of drug-loaded FF tubes, more characterizations are needed. For example, FIB-SEM could be applied to cut drug-loaded FF tubes in cross sections. Chemical/elemental characterization such as energy-dispersive X-ray spectroscopy could be performed to analyze the location of drug molecules.

In the final experiment discussed in this thesis the potential to utilize FF nanotube as drug carrier was evaluated. *In vitro* drug release studies of drug-loaded FF were carried out; the release profile was compared with that of the bare drug. Controlled drug release with a good overall release reaching over 60 % was observed for both models. Different kinetic models were applied to analyze the release kinetics and the best release mechanism was found by fitting the experimental data into different mathematical equations of each model. The results have shown that the release of both drugs exhibited a two-phased release pattern which clearly indicated a change of kinetics during the course of delivery. The biphasic release behaviour has been previously reported for a number of drug delivery systems. The results analysed using the Korsmeyer-Peppas model have revealed that the system follows a first order release that was modulated by a mixture of Fickian diffusion and case II transport; the latter phase could not be summarized using any existing knowledge due to the experimental exponent value lower than the theoretical value. Nevertheless, this phenomenon has also been reported for a number of drug delivery systems. In the future, more release studies are needed in order to fully understand FF nanotube based drug delivery systems. As previously discussed, different sized tubes could be introduced to study the effect of tube

length on drug release. Furthermore, different pH could also be applied. The pH used in the present study was neural (pH = 7.4); it would be interesting to investigate the release of drug in a simulated gastric acid medium.

In conclusion, the results presented throughout this thesis have provided information of the physicochemical and biological properties of self-assembling FF nanotubes; with the addition of the potential of FF nanotubes as drug carrier. Based on the knowledge presented in this thesis FF nanotubes offered promising potentials in the applications of nanofabrication and drug delivery as novel drug carriers.

References

1. Clamp, M., Fry, B., Kamal, M., Xie, X., Cuff, J., Lin, M. F., Kellis, M., Lindblad-Toh, K., and Lander, E. S., *Distinguishing protein-coding and noncoding genes in the human genome.* Proc Natl Acad Sci U S A, 2007. **104**(49): p. 19428-33.

2. Dobson, C. M., *Principles of protein folding, misfolding and aggregation.* Semin Cell Dev Biol, 2004. **15**(1): p. 3-16.

3. Hess, G. P. and Rupley, J. A., *Structure and function of proteins.* Snell, Esmond E. 1971. 1013-1044.

4. Klotz, I. M., Langerman, N. R., and Darnall, D. W., *Quaternary structure of proteins.* Snell, Esmond E. Annual Review of Biochemistry, Vol. 39. Vii + 1136p. Illus. Annual Reviews, Inc.: Palo Alto, Calif., U.S.A. 1970. 25-62.

5. Branden, C. and Tooze, J., *Introduction to protein structure.* 1991, New York, N.Y.: Garland Publishing. 302p.

6. Levintha.C, *Are there pathways for protein folding.* Journal De Chimie Physique Et De Physico-Chimie Biologique, 1968. **65**(1): p. 44-&.

7. Dill, K. A., Fiebig, K. M., and Chan, H. S., *Cooperativity in protein-folding kinetics.* Proceedings of the National Academy of Sciences of the United States of America, 1993. **90**(5): p. 1942-1946.

8. Faisca, P. F. N. and Plaxco, K. W., *Cooperativity and the origins of rapid, single-exponential kinetics in protein folding.* Protein Science, 2006. **15**(7): p. 1608-1618.

9. Weikl, T. R., Palassini, M., and Dill, K. A., *Cooperativity in two-state protein folding kinetics.* Protein Science, 2004. **13**(3): p. 822-829.

10. Faisca, P. F., *The nucleation mechanism of protein folding: a survey of computer simulation studies.* J Phys Condens Matter, 2009. **21**(37): p. 373102.

11.   Fersht, A. R., *Optimization of rates of protein folding: the nucleation-condensation mechanism and its implications.* Proc Natl Acad Sci U S A, 1995. **92**(24): p. 10869-73.

12.   Nagano, K., *Logical analysis of the mechanism of protein folding II. The nucleation process.* J Mol Biol, 1974. **84**(2): p. 337-72.

13.   Karplus, M., *The Levinthal paradox: yesterday and today.* Fold Des, 1997. **2**(4): p. S69-75.

14.   Baldwin, R. L., *Protein folding. Matching speed and stability.* Nature, 1994. **369**(6477): p. 183-4.

15.   Wolynes, P. G., Onuchic, J. N., and Thirumalai, D., *Navigating the folding routes.* Science, 1995. **267**(5204): p. 1619-20.

16.   Dinner, A. R., Sali, A., Smith, L. J., Dobson, C. M., and Karplus, M., *Understanding protein folding via free-energy surfaces from theory and experiment.* Trends Biochem Sci, 2000. **25**(7): p. 331-9.

17.   Fersht, A., *Structure and mechanism in protein science : a guide to enzyme catalysis and protein folding.* 1999, New York ; Basingstoke: W.H. Freeman. xxi, 631 p.

18.   Matouschek, A., Kellis, J. T., Jr., Serrano, L., and Fersht, A. R., *Mapping the transition state and pathway of protein folding by protein engineering.* Nature, 1989. **340**(6229): p. 122-6.

19.   Julian, P., Konevega, A. L., Scheres, S. H., Lazaro, M., Gil, D., Wintermeyer, W., Rodnina, M. V., and Valle, M., *Structure of ratcheted ribosomes with tRNAs in hybrid states.* Proc Natl Acad Sci U S A, 2008. **105**(44): p. 16924-7.

20.   Suzuka, I. and Kaji, A., *Studies on diphenylalanine synthesis.* Biochim Biophys Acta, 1967. **149**(2): p. 540-52.

21.   Fewell, S. W. and Brodsky, J. L., *Entry into the Endoplasmic Reticulum: Protein Translocation, Folding and Quality Control.* Trafficking Inside Cells: Pathways, Mechanisms and Regulation. 2009. 119-142.

22.   Ellis, R. J. and Minton, A. P., *Cell biology: join the crowd.* Nature, 2003. **425**(6953): p. 27-8.

23.   Ellis, R. J., *The molecular chaperone concept.* Semin Cell Biol, 1990. **1**(1): p. 1-9.

24.   Hartl, F. U., *Molecular chaperones in cellular protein folding.* Nature, 1996. **381**(6583): p. 571-9.

25.   Hartl, F. U. and Hayer-Hartl, M., *Molecular chaperones in the cytosol: from nascent chain to folded protein.* Science, 2002. **295**(5561): p. 1852-8.

26.   Schlieker, C., Bukau, B., and Mogk, A., *Prevention and reversion of protein aggregation by molecular chaperones in the E. coli cytosol: implications for their applicability in biotechnology.* J Biotechnol, 2002. **96**(1): p. 13-21.

27.   Walter, S. and Buchner, J., *Molecular chaperones--cellular machines for protein folding.* Angew Chem Int Ed Engl, 2002. **41**(7): p. 1098-113.

28.   Martin, J. and Hartl, F. U., *Molecular chaperones in cellular protein folding.* Bioessays, 1994. **16**(9): p. 689-92.

29.   Hershko, A. and Ciechanover, A., *The ubiquitin system.* Annu Rev Biochem, 1998. **67**: p. 425-79.

30.   Hershko, A. and Ciechanover, A., *The ubiquitin system for protein degradation.* Annu Rev Biochem, 1992. **61**: p. 761-807.

31.   Chakraborty, C., Nandi, S., and Jana, S., *Prion disease: a deadly disease for protein misfolding.* Curr Pharm Biotechnol, 2005. **6**(2): p. 167-77.

32.   Chiti, F. and Dobson, C. M., *Protein misfolding, functional amyloid, and human disease.* Annu Rev Biochem, 2006. **75**: p. 333-66.

33.   Dobson, C. M., *Protein misfolding, evolution and disease.* Trends Biochem Sci, 1999. **24**(9): p. 329-32.

34.   Fadiel, A., Eichenbaum, K. D., Hamza, A., Tuncalp, O., Luk, J., and Naftolin, F., *Protein misfolding and misprocessing in complex disease.* Protein Pept Lett, 2005. **12**(6): p. 499-506.

35.   Forloni, G., Terreni, L., Bertani, I., Fogliarino, S., Invernizzi, R., Assini, A., Ribizzi, G., Negro, A., Calabrese, E., Volonte, M. A.,

Mariani, C., Franceschi, M., Tabaton, M., and Bertoli, A., *Protein misfolding in Alzheimer's and Parkinson's disease: genetics and molecular mechanisms.* Neurobiol Aging, 2002. **23**(5): p. 957-76.

36. Greene, C. M. and McElvaney, N. G., *Protein misfolding and obstructive lung disease.* Proc Am Thorac Soc, 2010. **7**(6): p. 346-55.

37. Gregersen, N., Bolund, L., and Bross, P., *Protein misfolding, aggregation, and degradation in disease.* Mol Biotechnol, 2005. **31**(2): p. 141-50.

38. Gregersen, N., Bross, P., Vang, S., and Christensen, J. H., *Protein misfolding and human disease.* Annu Rev Genomics Hum Genet, 2006. **7**: p. 103-24.

39. Johansson, B. B., Torsvik, J., Gundersen, L., Vesterhus, M., Ragvin, A., Tjora, E., Fjeld, K., Hoem, D., Johansson, S., Rader, H., Lindquist, S., Hernell, O., Cnop, M., Saraste, J., Flatmark, T., Molven, A., and Njolstad, P. R., *Diabetes and pancreatic exocrine dysfunction due to mutations in the carboxyl-ester lipase gene (CEL-MODY): a protein misfolding disease.* J Biol Chem, 2011.

40. Luheshi, L. M., Crowther, D. C., and Dobson, C. M., *Protein misfolding and disease: from the test tube to the organism.* Curr Opin Chem Biol, 2008. **12**(1): p. 25-31.

41. Pattison, J. S. and Robbins, J., *Protein misfolding and cardiac disease: establishing cause and effect.* Autophagy, 2008. **4**(6): p. 821-3.

42. Soto, C., *Protein misfolding and disease; protein refolding and therapy.* FEBS Lett, 2001. **498**(2-3): p. 204-7.

43. Tan, J. M., Wong, E. S., and Lim, K. L., *Protein misfolding and aggregation in Parkinson's disease.* Antioxid Redox Signal, 2009. **11**(9): p. 2119-34.

44. Ursini, F., Davies, K. J., Maiorino, M., Parasassi, T., and Sevanian, A., *Atherosclerosis: another protein misfolding disease?* Trends Mol Med, 2002. **8**(8): p. 370-4.

45. Drummond, D. A. and Wilke, C. O., *Mistranslation-induced protein misfolding as a dominant constraint on coding-sequence evolution.* Cell, 2008. **134**(2): p. 341-52.

46. Dukan, S., Farewell, A., Ballesteros, M., Taddei, F., Radman, M., and Nystrom, T., *Protein oxidation in response to increased transcriptional or translational errors.* Proc Natl Acad Sci U S A, 2000. **97**(11): p. 5746-9.

47. Rajan, R. S. and Kopito, R. R., *Role of protein misfolding in retinal degeneration caused by a mutation in rhodopsin.* Abstracts of Papers of the American Chemical Society, 2004. **227**: p. U220-U220.

48. Trotter, E. W., Berenfeld, L., Krause, S. A., Petsko, G. A., and Gray, J. V., *Protein misfolding and temperature up-shift cause G1 arrest via a common mechanism dependent on heat shock factor in Saccharomycescerevisiae.* Proc Natl Acad Sci U S A, 2001. **98**(13): p. 7313-8.

49. DeMarco, M. L. and Daggett, V., *Molecular mechanism for low pH triggered misfolding of the human prion protein.* Biochemistry, 2007. **46**(11): p. 3045-54.

50. van der Kamp, M. W. and Daggett, V., *Influence of pH on the human prion protein: insights into the early steps of misfolding.* Biophys J, 2010. **99**(7): p. 2289-98.

51. Bieschke, J., Zhang, Q., Bosco, D. A., Lerner, R. A., Powers, E. T., Wentworth, P., Jr., and Kelly, J. W., *Small molecule oxidation products trigger disease-associated protein misfolding.* Acc Chem Res, 2006. **39**(9): p. 611-9.

52. Malolepsza, E. B., *Modeling of protein misfolding in disease.* Methods Mol Biol, 2008. **443**: p. 297-330.

53. Dobson, C. M., *The structural basis of protein folding and its links with human disease.* Philos Trans R Soc Lond B Biol Sci, 2001. **356**(1406): p. 133-45.

54. De Lorenzi, E., Giorgetti, S., Grossi, S., Merlini, G., Caccialanza, G., and Bellotti, V., *Pharmaceutical strategies against amyloidosis: old*

and new drugs in targeting a "protein misfolding disease". Curr Med Chem, 2004. **11**(8): p. 1065-84.

55.   Mazhul, V. M., Zaitseva, E. M., Shavlovskii, M. M., Povarova, O. I., Kuznetsova, I. M., and Turoverov, K. K., *[Room temperature phosphorescence of amorphous aggregates and amyloid fibrils resulting from protein misfolding].* Tsitologiia, 2005. **47**(11): p. 978-87.

56.   Benseny-Cases, N., Cocera, M., and Cladera, J., *Conversion of non-fibrillar beta-sheet oligomers into amyloid fibrils in Alzheimer's disease amyloid peptide aggregation.* Biochem Biophys Res Commun, 2007. **361**(4): p. 916-21.

57.   Coraci, I. S., Husemann, J., Berman, J. W., Hulette, C., Dufour, J. H., Campanella, G. K., Luster, A. D., Silverstein, S. C., and El-Khoury, J. B., *CD36, a class B scavenger receptor, is expressed on microglia in Alzheimer's disease brains and can mediate production of reactive oxygen species in response to beta-amyloid fibrils.* Am J Pathol, 2002. **160**(1): p. 101-12.

58.   Esler, W. P., Stimson, E. R., Jennings, J. M., Ghilardi, J. R., Mantyh, P. W., and Maggio, J. E., *Zinc-induced aggregation of human and rat beta-amyloid peptides in vitro.* J Neurochem, 1996. **66**(2): p. 723-32.

59.   Inoue, S. and Kisilevsky, R., *Beta-amyloid fibrils of Alzheimer's disease: pathologically altered, basement membrane-associated microfibrils?* Ital J Anat Embryol, 2001. **106**(2 Suppl 1): p. 93-102.

60.   Kajava, A. V., Baxa, U., and Steven, A. C., *Beta arcades: recurring motifs in naturally occurring and disease-related amyloid fibrils.* FASEB J, 2010. **24**(5): p. 1311-9.

61.   Westermark, P., Andersson, A., and Westermark, G. T., *Islet amyloid polypeptide, islet amyloid, and diabetes mellitus.* Physiol Rev, 2011. **91**(3): p. 795-826.

62.   Rezaei-Ghaleh, N., Andreetto, E., Yan, L. M., Kapurniotu, A., and Zweckstetter, M., *Interaction between amyloid beta peptide and an aggregation blocker peptide mimicking islet amyloid polypeptide.* PLoS One, 2011. **6**(5): p. e20289.

63. Wei, L., Jiang, P., Xu, W., Li, H., Zhang, H., Yan, L., Chan-Park, M. B., Liu, X. W., Tang, K., Mu, Y., and Pervushin, K., *The molecular basis of distinct aggregation pathways of islet amyloid polypeptide.* J Biol Chem, 2011. **286**(8): p. 6291-300.

64. Lechi, A., Tedeschi, F., Mancia, D., Pietrini, V., Tagliavini, F., Terzano, M. G., and Trabattoni, G., *Creutzfeld-Jakob disease: clinical, EEG and neuropathological findings in a cluster of eleven patients.* Ital J Neurol Sci, 1983. **4**(1): p. 47-59.

65. Saiz, A., Marin, C., Tolosa, E., and Graus, F., *[Diagnostic usefulness of the determination of protein 14-3-3 in cerebrospinal fluid in Creutzfeld-Jakob disease].* Neurologia, 1998. **13**(7): p. 324-8.

66. Chiti, F., Webster, P., Taddei, N., Clark, A., Stefani, M., Ramponi, G., and Dobson, C. M., *Designing conditions for in vitro formation of amyloid protofilaments and fibrils.* Proc Natl Acad Sci U S A, 1999. **96**(7): p. 3590-4.

67. Jimenez, J. L., Guijarro, J. I., Orlova, E., Zurdo, J., Dobson, C. M., Sunde, M., and Saibil, H. R., *Cryo-electron microscopy structure of an SH3 amyloid fibril and model of the molecular packing.* EMBO J, 1999. **18**(4): p. 815-21.

68. Fandrich, M., Fletcher, M. A., and Dobson, C. M., *Amyloid fibrils from muscle myoglobin.* Nature, 2001. **410**(6825): p. 165-6.

69. Fandrich, M. and Dobson, C. M., *The behaviour of polyamino acids reveals an inverse side chain effect in amyloid structure formation.* EMBO J, 2002. **21**(21): p. 5682-90.

70. Lopez De La Paz, M., Goldie, K., Zurdo, J., Lacroix, E., Dobson, C. M., Hoenger, A., and Serrano, L., *De novo designed peptide-based amyloid fibrils.* Proc Natl Acad Sci U S A, 2002. **99**(25): p. 16052-7.

71. Nettleton, E. J., Tito, P., Sunde, M., Bouchard, M., Dobson, C. M., and Robinson, C. V., *Characterization of the oligomeric states of insulin in self-assembly and amyloid fibril formation by mass spectrometry.* Biophys J, 2000. **79**(2): p. 1053-65.

72. Harper, J. D. and Lansbury, P. T., Jr., *Models of amyloid seeding in Alzheimer's disease and scrapie: mechanistic truths and physiological consequences of the time-dependent solubility of amyloid proteins.* Annu Rev Biochem, 1997. **66**: p. 385-407.

73. Maity, S., Kumar, P., and Haldar, D., *An amyloid-like fibril-forming supramolecular cross-beta-structure of a model peptide: a crystallographic insight.* Org Biomol Chem, 2011. **9**(10): p. 3787-91.

74. Chang, E. S., Liao, T. Y., Lim, T. S., Fann, W., and Chen, R. P., *A new amyloid-like beta-aggregate with amyloid characteristics, except fibril morphology.* J Mol Biol, 2009. **385**(4): p. 1257-65.

75. Sackewitz, M., von Einem, S., Hause, G., Wunderlich, M., Schmid, F. X., and Schwarz, E., *A folded and functional protein domain in an amyloid-like fibril.* Protein Sci, 2008. **17**(6): p. 1044-54.

76. Reches, M. and Gazit, E., *Casting metal nanowires within discrete self-assembled peptide nanotubes.* Science, 2003. **300**(5619): p. 625-7.

77. Shklovsky, J., Beker, P., Amdursky, N., Gazit, E., and Rosenman, G., *Bioinspired peptide nanotubes: Deposition technology and physical properties.* Materials Science and Engineering B-Advanced Functional Solid-State Materials, 2010. **169**(1-3): p. 62-66.

78. Kol, N., Adler-Abramovich, L., Barlam, D., Shneck, R. Z., Gazit, E., and Rousso, I., *Self-assembled peptide nanotubes are uniquely rigid bioinspired supramolecular structures.* Nano Lett, 2005. **5**(7): p. 1343-6.

79. Adler-Abramovich, L., Reches, M., Sedman, V. L., Allen, S., Tendler, S. J., and Gazit, E., *Thermal and chemical stability of diphenylalanine peptide nanotubes: implications for nanotechnological applications.* Langmuir, 2006. **22**(3): p. 1313-20.

80. Hill, R. J. A., Sedman, V. L., Allen, S., Williams, P. M., Paoli, M., Adler-Abramovich, L., Gazit, E., Eaves, L., and Tendler, S. J. B., *Alignment of aromatic peptide tubes in strong magnetic fields.* Advanced Materials, 2007. **19**(24): p. 4474-+.

81.   Niu, L., Chen, X., Allen, S., and Tendler, S. J., *Using the bending beam model to estimate the elasticity of diphenylalanine nanotubes.* Langmuir, 2007. **23**(14): p. 7443-6.

82.   Rao, S. N., Chan, M. F., Profeta, S. S., Jr., and Balaji, V. N., *Molecular mechanics studies on dipeptide models of diphenylalanine and its derivatives.* J Pept Res, 1997. **49**(2): p. 145-54.

83.   Reches, M. and Gazit, E., *Formation of closed-cage nanostructures by self-assembly of aromatic dipeptides.* Nano Letters, 2004. **4**(4): p. 581-585.

84.   Reches, M. and Gazit, E., *Molecular self-assembly of peptide nanostructures: mechanism of association and potential uses.* Current Nanoscience, 2006. **2**(2): p. 105-111.

85.   Lekprasert, B., Sedman, V., Roberts, C. J., Tedler, S. J. B., and Notingher, I., *Nondestructive Raman and atomic force microscopy measurement of molecular structure for individual diphenylalanine nanotubes.* Optics Letters, 2010. **35**(24): p. 4193-4195.

86.   Castillo, J., Tanzi, S., Dimaki, M., and Svendsen, W., *Manipulation of self-assembly amyloid peptide nanotubes by dielectrophoresis.* Electrophoresis, 2008. **29**(24): p. 5026-5032.

87.   Martins, T. D., de Souza, M. I., Cunha, B. B., Takahashi, P. M., Ferreira, F. F., Souza, J. A., Fileti, E. E., and Alves, W. A., *Influence of pH and Pyrenyl on the Structural and Morphological Control of Peptide Nanotubes.* Journal of Physical Chemistry C, 2011. **115**(16): p. 7906-7913.

88.   Ryu, J., Lim, S. Y., and Park, C. B., *Photoluminescent Peptide Nanotubles.* Advanced Materials, 2009. **21**(16): p. 1577-+.

89.   Song, Y., Challa, S. R., Medforth, C. J., Qiu, Y., Watt, R. K., Pena, D., Miller, J. E., van Swol, F., and Shelnutt, J. A., *Synthesis of peptide-nanotube platinum-nanoparticle composites.* Chem Commun (Camb), 2004(9): p. 1044-5.

90.   Smith, J. F., Knowles, T. P., Dobson, C. M., Macphee, C. E., and Welland, M. E., *Characterization of the nanoscale properties of*

individual amyloid fibrils. Proc Natl Acad Sci U S A, 2006. **103**(43): p. 15806-11.

91.   del Mercato, L. L., Maruccio, G., Pompa, P. P., Bochicchio, B., Tamburro, A. M., Cingolani, R., and Rinaldi, R., *Amyloid-like fibrils in elastin-related polypeptides: structural characterization and elastic properties.* Biomacromolecules, 2008. **9**(3): p. 796-803.

92.   Sedman, V. L., Adler-Abramovich, L., Allen, S., Gazit, E., and Tendler, S. J., *Direct observation of the release of phenylalanine from diphenylalanine nanotubes.* J Am Chem Soc, 2006. **128**(21): p. 6903-8.

93.   Sedman, V. L., Allen, S., Chen, X., Roberts, C. J., and Tendler, S. J., *Thermomechanical manipulation of aromatic peptide nanotubes.* Langmuir, 2009. **25**(13): p. 7256-9.

94.   HFIP safety datasheet, http://datasheets.scbt.com/sc-251540.pdf

95.   Makin, O. S., Atkins, E., Sikorski, P., Johansson, J., and Serpell, L. C., *Molecular basis for amyloid fibril formation and stability.* Proc Natl Acad Sci U S A, 2005. **102**(2): p. 315-20.

96.   Gorbitz, C. H., *Nanotube formation by hydrophobic dipeptides.* Chemistry, 2001. **7**(23): p. 5153-9.

97.   Gorbitz, C. H., *The structure of nanotubes formed by diphenylalanine, the core recognition motif of Alzheimer's beta-amyloid polypeptide.* Chem Commun (Camb), 2006(22): p. 2332-4.

98.   Gorbitz, C. H., *Microporous organic materials from hydrophobic dipeptides.* Chemistry-a European Journal, 2007. **13**(4): p. 1022-1031.

99.   Adler-Abramovich, L., Aronov, D., Beker, P., Yevnin, M., Stempler, S., Buzhansky, L., Rosenman, G., and Gazit, E., *Self-assembled arrays of peptide nanotubes by vapour deposition.* Nat Nanotechnol, 2009. **4**(12): p. 849-54.

100.   Ryu, J., Kim, S. W., Kang, K., and Park, C. B., *Synthesis of diphenylalanine/cobalt oxide hybrid nanowires and their application to energy storage.* ACS Nano, 2010. **4**(1): p. 159-64.

101. Ryu, J. and Park, C. B., *Synthesis of diphenylalanine/polyaniline core/shell conducting nanowires by peptide self-assembly.* Angew Chem Int Ed Engl, 2009. **48**(26): p. 4820-3.

102. Ryu, J. and Park, C. B., *Solid-Phase Growth of Nanostructures from Amorphous Peptide Thin Film: Effect of Water Activity and Temperature.* Chemistry of Materials, 2008. **20**(13): p. 4284-4290.

103. Ryu, J. and Park, C. B., *High-Temperature Self-Assembly of Peptides into Vertically Well-Aligned Nanowires by Aniline Vapor.* Advanced Materials, 2008. **20**(19): p. 3754-+.

104. Reches, M. and Gazit, E., *Controlled patterning of aligned self-assembled peptide nanotubes.* Nat Nanotechnol, 2006. **1**(3): p. 195-200.

105. Li, M. and Ou-Yang, Z.-c., *Concentration-induced shape transition of nano-aggregates in solution.* Thin Solid Films, 2008. **517**(4): p. 1424-1427.

106. Zhu, P., Yan, X., Su, Y., Yang, Y., and Li, J., *Solvent-induced structural transition of self-assembled dipeptide: from organogels to microcrystals.* Chemistry, 2010. **16**(10): p. 3176-83.

107. Kumaraswamy, P., Lakshmanan, R., Sethuraman, S., and Krishnan, U. M., *Self-assembly of peptides: influence of substrate, pH and medium on the formation of supramolecular assemblies.* Soft Matter, 2011. **7**(6): p. 2744-2754.

108. Heredia, A., Bdikin, I., Kopyl, S., Mishina, E., Semin, S., Sigov, A., German, K., Bystrov, V., Gracio, J., and Kholkin, A. L., *Temperature-driven phase transformation in self-assembled diphenylalanine peptide nanotubes.* Journal of Physics D-Applied Physics, 2010. **43**(46).

109. Tarabout, C., Roux, S., Gobeaux, F., Fay, N., Pouget, E., Meriadec, C., Ligeti, M., Thomas, D., M, I. J., Besselievre, F., Buisson, D. A., Verbavatz, J. M., Petitjean, M., Valery, C., Perrin, L., Rousseau, B., Artzner, F., Paternostre, M., and Cintrat, J. C., *Control of peptide nanotube diameter by chemical modifications of an aromatic residue involved in a single close contact.* Proc Natl Acad Sci U S A, 2011. **108**(19): p. 7679-84.

110.   Vauthey, S., Santoso, S., Gong, H., Watson, N., and Zhang, S., *Molecular self-assembly of surfactant-like peptides to form nanotubes and nanovesicles.* Proc Natl Acad Sci U S A, 2002. **99**(8): p. 5355-60.

111.   Posa, M., Kevresan, S., Mikov, M., Cirin-Novta, V., and Kuhajda, K., *Critical micellar concentrations of keto derivatives of selected bile acids: Thermodynamic functions of micelle formation.* Colloids and Surfaces B-Biointerfaces, 2008. **64**(2): p. 151-161.

112.   Srinivasan, V. and Blankschtein, D., *Effect of counterion binding on micellar solution behavior: 1. Molecular-thermodynamic theory of micellization of ionic surfactants.* Langmuir, 2003. **19**(23): p. 9932-9945.

113.   Yan, X. H., Cui, Y., He, Q., Wang, K. W., Li, J. B., Mu, W. H., Wang, B. L., and Ou-yang, Z. C., *Reversible transitions between peptide nanotubes and vesicle-like structures including theoretical modeling studies.* Chemistry-a European Journal, 2008. **14**(19): p. 5974-5980.

114.   Amdursky, N., Beker, P., Koren, I., Bank-Srour, B., Mishina, E., Semin, S., Rasing, T., Rosenberg, Y., Barkay, Z., Gazit, E., and Rosenman, G., *Structural transition in peptide nanotubes.* Biomacromolecules, 2011. **12**(4): p. 1349-54.

115.   Carny, O., Shalev, D. E., and Gazit, E., *Fabrication of coaxial metal nanocables using a self-assembled peptide nanotube scaffold.* Nano Lett, 2006. **6**(8): p. 1594-7.

116.   Han, T. H., Kim, J., Park, J. S., Park, C. B., Ihee, H., and Kim, S. O., *Liquid crystalline peptide nanowires.* Advanced Materials, 2007. **19**(22): p. 3924-+.

117.   Yang, Z., Liang, G., and Xu, B., *Enzymatic hydrogelation of small molecules.* Acc Chem Res, 2008. **41**(2): p. 315-26.

118.   Smith, A. M., Williams, R. J., Tang, C., Coppo, P., Collins, R. F., Turner, M. L., Saiani, A., and Ulijn, R. V., *Fmoc-Diphenylalanine self assembles to a hydrogel via a novel architecture based on pi-pi interlocked beta-sheets.* Advanced Materials, 2008. **20**(1): p. 37-+.

119. Jayawarna, V., Ali, M., Jowitt, T. A., Miller, A. E., Saiani, A., Gough, J. E., and Ulijn, R. V., *Nanostructured hydrogels for three-dimensional cell culture through self-assembly of fluorenylmethoxycarbonyl-dipeptides.* Advanced Materials, 2006. **18**(5): p. 611-+.

120. Hoffman, A. S., *Hydrogels for biomedical applications.* Ann N Y Acad Sci, 2001. **944**: p. 62-73.

121. Yan, X., Cui, Y., He, Q., Wang, K., and Li, J., *Organogels based on self-assembly of diphenylalanine peptide and their application to immobilize quantum dots.* Chemistry of Materials, 2008. **20**(4): p. 1522-1526.

122. Panda, J. J., Mishra, A., Basu, A., and Chauhan, V. S., *Stimuli responsive self-assembled hydrogel of a low molecular weight free dipeptide with potential for tunable drug delivery.* Biomacromolecules, 2008. **9**(8): p. 2244-2250.

123. Mahler, A., Reches, M., Rechter, M., Cohen, S., and Gazit, E., *Rigid, self-assembled hydrogel composed of a modified aromatic dipeptide.* Advanced Materials, 2006. **18**(11): p. 1365-+.

124. Tang, C., Smith, A. M., Collins, R. F., Ulijn, R. V., and Saiani, A., *Fmoc-diphenylalanine self-assembly mechanism induces apparent pKa shifts.* Langmuir, 2009. **25**(16): p. 9447-53.

125. Zhou, M., Smith, A. M., Das, A. K., Hodson, N. W., Collins, R. F., Ulijn, R. V., and Gough, J. E., *Self-assembled peptide-based hydrogels as scaffolds for anchorage-dependent cells.* Biomaterials, 2009. **30**(13): p. 2523-2530.

126. Huang, R., Qi, W., Feng, L., Su, R., and He, Z., *Self-assembling peptide-polysaccharide hybrid hydrogel as a potential carrier for drug delivery.* Soft Matter, 2011. **7**(13): p. 6222-6230.

127. Roy, S. and Banerjee, A., *Amino acid based smart hydrogel: formation, characterization and fluorescence properties of silver nanoclusters within the hydrogel matrix.* Soft Matter, 2011. **7**(11): p. 5300-5308.

128. Thornton, K., Smith, A. M., Merry, C. L. R., and Ulijn, R. V., *Controlling stiffness in nanostructured hydrogels produced by*

enzymatic dephosphorylation. Biochemical Society Transactions, 2009.
37: p. 660-664.

129. vanEijk, H. M. H., Rooyakkers, D. R., Wagenmakers, A. J. M., Soeters, P. B., and Deutz, N. E. P., *Isolation and quantitation of isotopically labeled amino acids from biological samples.* Journal of Chromatography B, 1997. **691**(2): p. 287-296.

130. Kim, J., Han, T. H., Kim, Y. I., Park, J. S., Choi, J., Churchill, D. G., Kim, S. O., and Ihee, H., *Role of water in directing diphenylalanine assembly into nanotubes and nanowires.* Adv Mater, 2010. **22**(5): p. 583-7.

131. Yemini, M., Reches, M., Gazit, E., and Rishpon, J., *Peptide nanotube-modified electrodes for enzyme-biosensor applications.* Anal Chem, 2005. **77**(16): p. 5155-9.

132. Yemini, M., Reches, M., Rishpon, J., and Gazit, E., *Novel electrochemical biosensing platform using self-assembled peptide nanotubes.* Nano Lett, 2005. **5**(1): p. 183-6.

133. Adler-Abramovich, L., Badihi-Mossberg, M., Gazit, E., and Rishpon, J., *Characterization of Peptide-Nanostructure-Modified Electrodes and Their Application for Ultrasensitive Environmental Monitoring.* Small, 2010. **6**(7): p. 825-831.

134. Kim, J. H., Ryu, J., and Park, C. B., *Selective detection of neurotoxin by photoluminescent peptide nanotubes.* Small, 2011. **7**(6): p. 718-22.

135. Jayawarna, V., Smith, A., Gough, J. E., and Ulijn, R. V., *Three-dimensional cell culture of chondrocytes on modified di-phenylaianine scaffolds.* Biochemical Society Transactions, 2007. **35**: p. 535-537.

136. Liebmann, T., Rydholm, S., Akpe, V., and Brismar, H., *Self-assembling Fmoc dipeptide hydrogel for in situ 3D cell culturing.* Bmc Biotechnology, 2007. **7**.

137. Reches, M. and Gazit, E., *Biological and chemical decoration of peptide nanostructures via biotin-avidin interactions.* Journal of Nanoscience and Nanotechnology, 2007. **7**(7): p. 2239-2245.

138. Helen, W., Ulijn, R. V., and Gough, J. E., *Hydrogels based on Fmoc-diphenylalanine and Fmoc-diglycine for nucleus pulposus disc tissue engineering.* International Journal of Experimental Pathology, 2009. **90**(2): p. A113-A114.

139. Sutton, S., Campbell, N. L., Cooper, A. I., Kirkland, M., Frith, W. J., and Adams, D. J., *Controlled Release from Modified Amino Acid Hydrogels Governed by Molecular Size or Network Dynamics.* Langmuir, 2009. **25**(17): p. 10285-10291.

140. Kakizawa, T., Koide-Yoshida, S., Kimura, T., Uchimura, H., Hayashi, Y., Saito, K., and Kiso, Y., *Fmoc-based solid phase chemical synthesis of 71-meric neuregulin 1-beta 1, an epidermal growth factor-like domain.* Journal of Peptide Science, 2008. **14**(3): p. 261-266.

141. Orbach, R., Adler-Abramovich, L., Zigerson, S., Mironi-Harpaz, I., Seliktar, D., and Gazit, E., *Self-Assembled Fmoc-Peptides as a Platform for the Formation of Nanostructures and Hydrogels.* Biomacromolecules, 2009. **10**(9): p. 2646-2651.

142. Kuhl, P., Sauberlich, S., and Jakubke, H. D., *Model studies on protease-catalyzed peptide-synthesis using 9-fluorenylmethoxycarbonyl protected amino-acid derivatives.* Monatshefte Fur Chemie, 1992. **123**(11): p. 1015-1022.

143. Yang, K. W., Sobieski, D. N., Carenbauer, A. L., Crawford, P. A., Makaroff, C. A., and Crowder, M. W., *Explaining the inhibition of glyoxalase II by 9-fluorenylmethoxycarbonyl-protected glutathione derivatives.* Arch Biochem Biophys, 2003. **414**(2): p. 271-278.

144. Perich, J. W., Ruzzene, M., Pinna, L. A., and Reynolds, E. C., *Efficient Fmoc solid-phase peptide-synthesis of O-phosphotyrosyl-containing peptides and their use as phsphatase substrates.* International Journal of Peptide and Protein Research, 1994. **43**(1): p. 39-46.

145. Yao, Z. J., Gao, Y., Voigt, J. H., Ford, H., and Burke, T. R., *Synthesis of Fmoc-protected 4-carboxydifluoromethyl-L-phenylalanine: A phosphotyrosyl mimetic of potential use for signal transduction studies.* Tetrahedron, 1999. **55**(10): p. 2865-2874.

146. Yan, X. H., He, Q., Wang, K. W., Duan, L., Cui, Y., and Li, J. B., *Transition of cationic dipeptide nanotubes into vesicles and oligonucleotide delivery.* Angewandte Chemie-International Edition, 2007. **46**(14): p. 2431-2434.

147. Anwer, K., Logan, M., Tagliaferri, F., Wadhwa, M., Monera, O., Tung, C. H., Chen, W., Leonard, P., French, M., Proctor, B., Wilson, E., Singhal, A., and Rolland, A., *Synthetic glycopeptide-based delivery systems for systemic gene targeting to hepatocytes.* Pharmaceutical Research, 2000. **17**(4): p. 451-459.

148. Wiradharma, N., Tong, Y. W., and Yang, Y.-Y., *Design and Evaluation of Peptide Amphiphiles with Different Hydrophobic Blocks for Simultaneous Delivery of Drugs and Genes.* Macromolecular Rapid Communications, 2010. **31**(13): p. 1212-1217.

149. Lehn, J. M., *Toward complex matter: supramolecular chemistry and self-organization.* Proc Natl Acad Sci U S A, 2002. **99**(8): p. 4763-8.

150. Whitesides, G. M. and Grzybowski, B., *Self-assembly at all scales.* Science, 2002. **295**(5564): p. 2418-2421.

151. Vendruscolo, M., Zurdo, J., MacPhee, C. E., and Dobson, C. M., *Protein folding and misfolding: a paradigm of self-assembly and regulation in complex biological systems.* Philos Transact A Math Phys Eng Sci, 2003. **361**(1807): p. 1205-22.

152. Gething, M. J. and Sambrook, J., *Protein folding in the cell.* Nature, 1992. **355**(6355): p. 33-45.

153. Aizenberg, J. and Fratzl, P., *Biological and Biomimetic Materials.* Advanced Materials, 2009. **21**(4): p. 387-388.

154. Sanchez, C., Arribart, H., and Guille, M. M. G., *Biomimetism and bioinspiration as tools for the design of innovative materials and systems.* Nature Materials, 2005. **4**(4): p. 277-288.

155. Ariga, K., Hill, J. P., Lee, M. V., Vinu, A., Charvet, R., and Acharya, S., *Challenges and breakthroughs in recent research on self-assembly.* Science and Technology of Advanced Materials, 2008. **9**(1).

156.   Gazit, E., *Self-assembled peptide nanostructures: the design of molecular building blocks and their technological utilization.* Chem. Soc. Rev., 2007. **36**: p. 1263-1269.

157.   Dong, H., Yang, Z., Yang, W., Yin, W., Song, Y., and Yang, H., *Synthesis and self-assembly of CdSe nanometer scale building blocks.* Progress in Chemistry, 2006. **18**(12): p. 1608-1614.

158.   Tsai, C.-J., Zheng, J., Zanuy, D., Haspel, N., Wolfson, H., Aleman, C., and Nussinov, R., *Principles of nanostructure design with protein building blocks.* Proteins-Structure Function and Bioinformatics, 2007. **68**(1): p. 1-12.

159.   Amdursky, N., Molotskii, M., Gazit, E., and Rosenman, G., *Elementary Building Blocks of Self-Assembled Peptide Nanotubes.* Journal of the American Chemical Society, 2010. **132**(44): p. 15632-15636.

160.   Zayed, J. M., Nouvel, N., Rauwald, U., and Scherman, O. A., *Chemical complexity-supramolecular self-assembly of synthetic and biological building blocks in water.* Chemical Society Reviews, 2010. **39**(8): p. 2806-2816.

161.   Charalambidis, G., Kasotakis, E., Lazarides, T., Mitraki, A., and Coutsolelos, A. G., *Self-Assembly Into Spheres of a Hybrid Diphenylalanine-Porphyrin: Increased Fluorescence Lifetime and Conserved Electronic Properties.* Chemistry-a European Journal, 2011. **17**(26): p. 7213-7219.

162.   Huang, R., Su, R., Qi, W., Zhao, J., and He, Z., *Hierarchical, interface-induced self-assembly of diphenylalanine: formation of peptide nanofibers and microvesicles.* Nanotechnology, 2011. **22**(24).

163.   Wang, M., Du, L., Wu, X., Xiong, S., and Chu, P. K., *Charged Diphenylalanine Nanotubes and Controlled Hierarchical Self-Assembly.* ACS Nano, 2011. **5**(6): p. 4448-4454.

164.   Yuan, J., Chen, J., Wu, X., Fang, K., and Niu, L., *A NADH biosensor based on diphenylalanine peptide/carbon nanotube nanocomposite.* Journal of Electroanalytical Chemistry, 2011. **656**(1-2): p. 120-124.

165.   Raman   band   database,
        http://www.horiba.com/fileadmin/uploads/Scientific/Documents/Rama
        n/bands.pdf

166.   Sidelman, N., Rosenberg, Y., and Richter, S., *Peptide-based spherulitic films--formation and properties.* J Colloid Interface Sci, 2010. **343**(1): p. 387-91.

167.   Friedrich, R. P., Tepper, K., Ronicke, R., Soom, M., Westermann, M., Reymann, K., Kaether, C., and Fandrich, M., *Mechanism of amyloid plaque formation suggests an intracellular basis of Abeta pathogenicity.* Proc Natl Acad Sci U S A, 2010. **107**(5): p. 1942-7.

168.   Liang, Y., Lynn, D. G., and Berland, K. M., *Direct observation of nucleation and growth in amyloid self-assembly.* J Am Chem Soc, 2010. **132**(18): p. 6306-8.

169.   Hu, X., Cook, S., Wang, P., Hwang, H. M., Liu, X., and Williams, Q. L., *In vitro evaluation of cytotoxicity of engineered carbon nanotubes in selected human cell lines.* Sci Total Environ, 2010. **408**(8): p. 1812-7.

170.   Davoren, M., Herzog, E., Casey, A., Cottineau, B., Chambers, G., Byrne, H. J., and Lyng, F. M., *In vitro toxicity evaluation of single walled carbon nanotubes on human A549 lung cells.* Toxicol In Vitro, 2007. **21**(3): p. 438-48.

171.   Helland, A., Wick, P., Koehler, A., Schmid, K., and Som, C., *Reviewing the environmental and human health knowledge base of carbon nanotubes.* Environ Health Perspect, 2007. **115**(8): p. 1125-31.

172.   Feazell, R. P., Nakayama-Ratchford, N., Dai, H., and Lippard, S. J., *Soluble single-walled carbon nanotubes as longboat delivery systems for Platinum(IV) anticancer drug design.* Journal of the American Chemical Society, 2007. **129**(27): p. 8438-+.

173.   Zeni, O., Palumbo, R., Bernini, R., Zeni, L., Sarti, M., and Scarfi, M. R., *Cytotoxicity investigation on cultured human blood cells treated with single-wall carbon nanotubes.* Sensors, 2008. **8**(1): p. 488-499.

174. Casey, A., Herzog, E., Lyng, F. M., Byrne, H. J., Chambers, G., and Davoren, M., *Single walled carbon nanotubes induce indirect cytotoxicity by medium depletion in A549 lung cells.* Toxicology Letters, 2008. **179**(2): p. 78-84.

175. Hitoshi, K., Katoh, M., Suzuki, T., Ando, Y., and Nadai, M., *Differential effects of single-walled carbon nanotubes on cell viability of human lung and pharynx carcinoma cell lines.* Journal of Toxicological Sciences, 2011. **36**(3): p. 379-387.

176. Ago, H., Uchimura, E.-i., Saito, T., Ohshima, S., Ishigami, N., Tsuji, M., Yumura, M., and Miyake, M., *Mechanical immobilization of Hela cells on aligned carbon nanotube array.* Materials Letters, 2006. **60**(29-30): p. 3851-3854.

177. Yehia, H. N., Draper, R. K., Mikoryak, C., Walker, E. K., Bajaj, P., Musselman, I. H., Daigrepont, M. C., Dieckmann, G. R., and Pantano, P., *Single-walled carbon nanotube interactions with HeLa cells.* Journal of Nanobiotechnology, 2007. **5**: p. 8.

178. Patlolla, A., Patlolla, B., and Tchounwou, P., *Evaluation of cell viability, DNA damage, and cell death in normal human dermal fibroblast cells induced by functionalized multiwalled carbon nanotube.* Molecular and Cellular Biochemistry, 2010. **338**(1-2): p. 225-232.

179. Patlolla, A. and Tchounwou, P., *Multiwalled carbon nanotube-induce cytotoxicity, genotoxicity and apoptosis in normal human dermal fibroblast cells.* Environmental and Molecular Mutagenesis, 2007. **48**(7): p. 563-563.

180. Murray, A. R., Kisin, E., Leonard, S. S., Young, S. H., Kommineni, C., Kagan, V. E., Castranova, V., and Shvedova, A. A., *Oxidative stress and inflammatory response in dermal toxicity of single-walled carbon nanotubes.* Toxicology, 2009. **257**(3): p. 161-171.

181. Isaksson, B., Wang, F., Permert, J., Olsson, M., Fruin, B., Herrington, M. K., Enochsson, L., Erlanson-Albertsson, C., and Arnelo, U., *Chronically administered islet amyloid polypeptide in rats serves as an*

adiposity inhibitor and regulates energy homeostasis. Pancreatology, 2005. **5**(1): p. 29-36.

182. Sakaguchi, N., Watari, F., Yokoyama, A., and Nodasaka, Y., *High-resolution electron microscopy of multi-wall carbon nanotubes in the subcutaneous tissue of rats.* Journal of Electron Microscopy, 2008. **57**(5): p. 159-164.

183. Sato, Y., Yokoyama, A., Shibata, K., Akimoto, Y., Ogino, S., Nodasaka, Y., Kohgo, T., Tamura, K., Akasaka, T., Uo, M., Motomiya, K., Jeyadevan, B., Ishiguro, M., Hatakeyama, R., Watari, F., and Tohji, K., *Influence of length on cytotoxicity of multi-walled carbon nanotubes against human acute monocytic leukemia cell line THP-I in vitro and subcutaneous tissue of rats in vivo.* Molecular Biosystems, 2005. **1**(2): p. 176-182.

184. Casey, A., Herzog, E., Davoren, M., Lyng, F. M., Byrne, H. J., and Chambers, G., *Spectroscopic analysis confirms the interactions between single walled carbon nanotubes and various dyes commonly used to assess cytotoxicity.* Carbon, 2007. **45**(7): p. 1425-1432.

185. Monteiro-Riviere, N. A., Inman, A. O., and Zhang, L. W., *Limitations and relative utility of screening assays to assess engineered nanoparticle toxicity in a human cell line.* Toxicology and Applied Pharmacology, 2009. **234**(2): p. 222-235.

186. Jos, A., Pichardo, S., Puerto, M., Sanchez, E., Grilo, A., and Camean, A. M., *Cytotoxicity of carboxylic acid functionalized single wall carbon nanotubes on the human intestinal cell line Caco-2.* Toxicology in Vitro, 2009. **23**(8): p. 1491-1496.

187. Lobo, A. O., Corat, M. A. F., Antunes, E. F., Palma, M. B. S., Pacheco-Soares, C., and Corat, E. J., *Cytotoxicity analysis of vertically aligned multi-walled carbon nanotubes by colorimetric assays.* Synthetic Metals, 2009. **159**(21-22): p. 2165-2166.

188. Worle-Knirsch, J. M., Pulskamp, K., and Krug, H. F., *Oops they did it again! Carbon nanotubes hoax scientists in viability assays.* Nano Letters, 2006. **6**(6): p. 1261-1268.

189.   Fisichella, M., Dabboue, H., Bhattacharyya, S., Saboungi, M.-L., Salvetat, J.-P., Hevor, T., and Guerin, M., *Mesoporous silica nanoparticles enhance MTT formazan exocytosis in HeLa cells and astrocytes.* Toxicology in Vitro, 2009. **23**(4): p. 697-703.

190.   Vittorio, O., Raffa, V., and Cuschieri, A., *Influence of purity and surface oxidation on cytotoxicity of multiwalled carbon nanotubes with human neuroblastoma cells.* Nanomedicine-Nanotechnology Biology and Medicine, 2009. **5**(4): p. 424-431.

191.   Zhu, Y. and Li, W., *Cytotoxicity of carbon nanotubes.* Science in China Series B-Chemistry, 2008. **51**(11): p. 1021-1029.

192.   Cui, H.-F., Vashist, S. K., Al-Rubeaan, K., Luong, J. H. T., and Sheu, F.-S., *Interfacing Carbon Nanotubes with Living Mammalian Cells and Cytotoxicity Issues.* Chemical Research in Toxicology, 2010. **23**(7): p. 1131-1147.

193.   Wang, X., Xia, T., Ntim, S. A., Ji, Z., George, S., Meng, H., Zhang, H., Castranova, V., Mitra, S., and Nel, A. E., *Quantitative Techniques for Assessing and Controlling the Dispersion and Biological Effects of Multiwalled Carbon Nanotubes in Mammalian Tissue Culture Cells.* ACS Nano, 2010. **4**(12): p. 7241-7252.

194.   Sun, Z., Liu, Z., Meng, J., Duan, J., Xie, S., Lu, X., Zhu, Z., Wang, C., Chen, S., Xu, H., and Yang, X.-D., *Carbon Nanotubes Enhance Cytotoxicity Mediated by Human Lymphocytes In Vitro.* PLoS One, 2011. **6**(6).

195.   Elgrabli, D., Abella-Gallart, S., Aguerre-Chariol, O., Robidel, F., Rogerieux, F., Boczkowski, J., and Lacroix, G., *Effect of BSA on carbon nanotube dispersion for in vivo and in vitro studies.* Nanotoxicology, 2007. **1**(4): p. 266-278.

196.   Geys, J., Nemery, B., and Hoet, P. H. M., *Assay conditions can influence the outcome of cytotoxicity tests of nanomaterials: Better assay characterization is needed to compare studies.* Toxicology in Vitro, 2010. **24**(2): p. 620-629.

197.   Zhu, Y., Li, W., Li, Q., Li, Y., Li, Y., Zhang, X., and Huang, Q., *Effects of serum proteins on intracellular uptake and cytotoxicity of carbon nanoparticles.* Carbon, 2009. **47**(5): p. 1351-1358.

198.   Campidelli, S., Klumpp, C., Bianco, A., Guldi, D. M., and Prato, M., *Functionalization of CNT: Synthesis and applications in photovoltaics and biology.* Journal of Physical Organic Chemistry, 2006. **19**(8-9): p. 531-539.

199.   Kulamarva, A., Bhathena, J., Malhotra, M., Sebak, S., Nalamasu, O., Ajayan, P., and Prakash, S., *In vitro cytotoxicity of functionalized single walled carbon nanotubes for targeted gene delivery applications.* Nanotoxicology, 2008. **2**(4): p. 184-188.

200.   Hussain, M. A., Kabir, M. A., and Sood, A. K., *On the cytotoxicity of carbon nanotubes.* Current Science, 2009. **96**(5): p. 664-673.

201.   Tong, H., McGee, J. K., Saxena, R. K., Kodavanti, U. P., Devlin, R. B., and Gilmour, M. I., *Influence of acid functionalization on the cardiopulmonary toxicity of carbon nanotubes and carbon black particles in mice.* Toxicology and Applied Pharmacology, 2009. **239**(3): p. 224-232.

202.   Lacerda, L., Herrero, M. A., Venner, K., Bianco, A., Prato, M., and Kostarelos, K., *Carbon-nanotube shape and individualization critical for renal excretion.* Small, 2008. **4**(8): p. 1130-2.

203.   Pastorin, G., Wu, W., Wieckowski, S., Briand, J. P., Kostarelos, K., Prato, M., and Bianco, A., *Double functionalisation of carbon nanotubes for multimodal drug delivery.* Chemical Communications, 2006(11): p. 1182-1184.

204.   Prato, M., Kostarelos, K., and Bianco, A., *Functionalized carbon nanotubes in drug design and discovery.* Acc Chem Res, 2008. **41**(1): p. 60-68.

205.   Samori, C., Ali-Boucetta, H., Sainz, R., Guo, C., Toma, F. M., Fabbro, C., da Ros, T., Prato, M., Kostarelos, K., and Bianco, A., *Enhanced anticancer activity of multi-walled carbon nanotube-methotrexate*

conjugates using cleavable linkers. Chem Commun (Camb), 2010. **46**(9): p. 1494-6.

206. Wu, W., Li, R., Bian, X., Zhu, Z., Ding, D., Li, X., Jia, Z., Jiang, X., and Hu, Y., *Covalently Combining Carbon Nanotubes with Anticancer Agent: Preparation and Antitumor Activity.* ACS Nano, 2009. **3**(9): p. 2740-2750.

207. Hillebrenner, H., Buyukserin, F., Stewart, J. D., and Martin, C. R., *Template synthesized nanotubes for biomedical delivery applications.* Nanomedicine, 2006. **1**(1): p. 39-50.

208. Hilder, T. A. and Hill, J. M., *Carbon nanotubes as drug delivery nanocapsules.* Current Applied Physics, 2008. **8**(3-4): p. 258-261.

209. Singh, I., Rehni, A. K., Kumar, P., Kumar, M., and Aboul-Enein, H. Y., *Carbon Nanotubes: Synthesis, Properties and Pharmaceutical Applications.* Fullerenes Nanotubes and Carbon Nanostructures, 2009. **17**(4): p. 361-377.

210. Degim, I. T., Burgess, D. J., and Papadimitrakopoulos, F., *Carbon nanotubes for transdermal drug delivery.* Journal of Microencapsulation, 2010. **27**(8): p. 669-681.

211. Li, S., He, H., Jiao, Q., and Chuong, P.-H., *Applications of Carbon Nanotubes in Drug and Gene Delivery.* Progress in Chemistry, 2008. **20**(11): p. 1798-1803.

212. Panda, J. J., Dua, R., Mishra, A., Mittra, B., and Chauhan, V. S., *3D cell growth and proliferation on a RGD functionalized nanofibrillar hydrogel based on a conformationally restricted residue containing dipeptide.* ACS Appl Mater Interfaces, 2010. **2**(10): p. 2839-48.

213. Peek, M. J., Markham, R., and Fraser, I. S., *A comparison of fetal and newborn bovine serum components.* Australian Journal of Medical Laboratory Science, 1989. **10**(2): p. 40-41.

214. Temple, P. A., *Total internal-reflection microscopy - a surface inspection technique.* Applied Optics, 1981. **20**(15): p. 2656-2664.

215.   Jabr, S. N., *Total internal-reflection microscopy - inspection of surfaces of high bulk scatter materials* Applied Optics, 1985. **24**(11): p. 1689-1692.

216.   Antonelli, A., Serafini, S., Menotta, M., Sfara, C., Pierige, F., Giorgi, L., Ambrosi, G., Rossi, L., and Magnani, M., *Improved cellular uptake of functionalized single-walled carbon nanotubes.* Nanotechnology, 2010. **21**(42): p. 425101.

217.   Menard-Moyon, C., Venturelli, E., Fabbro, C., Samori, C., Da Ros, T., Kostarelos, K., Prato, M., and Bianco, A., *The alluring potential of functionalized carbon nanotubes in drug discovery.* Expert Opinion on Drug Discovery, 2010. **5**(7): p. 691-707.

218.   Shi, X., Sitharaman, B., Pham, Q. P., Liang, F., Wu, K., Billups, W. E., Wilson, L. J., and Mikos, A. G., *Fabrication of porous ultra-short single-walled carbon nanotube nanocomposite scaffolds for bone tissue engineering.* Biomaterials, 2007. **28**(28): p. 4078-4090.

219.   Abarrategi, A., Gutierrez, M. C., Moreno-Vicente, C., Hortiguela, M. J., Ramos, V., Lopez-Lacomba, J. L., Ferrer, M. L., and del Monte, F., *Multiwall carbon nanotube scaffolds for tissue engineering purposes.* Biomaterials, 2008. **29**(1): p. 94-102.

220.   Avdulov, N. A., Chochina, S. V., Daragan, V. A., Schroeder, F., Mayo, K. H., and Wood, W. G., *Direct binding of ethanol to bovine serum albumin: A fluorescent and C-13 NMR multiplet relaxation study.* Biochemistry, 1996. **35**(1): p. 340-347.

221.   Chipot, C. and Tarek, M., *Interaction of a peptide nanotube with a water-membrane interface.* Physical Biology, 2006. **3**(1): p. S20-S25.

222.   Ren, Y., Wong, S. M., and Lim, L. Y., *Folic acid-conjugated protein cages of a plant virus: a novel delivery platform for doxorubicin.* Bioconjug Chem, 2007. **18**(3): p. 836-43.

223.   Robertson, S. K. and Bike, S. G., *Quantifying cell-surface interactions using model cells and total internal reflection microscopy.* Langmuir, 1998. **14**(4): p. 928-934.

224. Picart, C., Lavalle, P., Hubert, P., Cuisinier, F. J. G., Decher, G., Schaaf, P., and Voegel, J. C., *Buildup mechanism for poly(L-lysine)/hyaluronic acid films onto a solid surface.* Langmuir, 2001. **17**(23): p. 7414-7424.

225. Byrne, G. D., Pitter, M. C., Zhang, J., Falcone, F. H., Stolnik, S., and Somekh, M. G., *Total internal reflection microscopy for live imaging of cellular uptake of sub-micron non-fluorescent particles.* J Microsc, 2008. **231**(Pt 1): p. 168-79.

226. Hillaireau, H. and Couvreur, P., *Nanocarriers' entry into the cell: relevance to drug delivery.* Cellular and Molecular Life Sciences, 2009. **66**(17): p. 2873-2896.

227. Dalby, M. J., Berry, C. C., Riehle, M. O., Sutherland, D. S., Agheli, H., and Curtis, A. S. G., *Attempted endocytosis of nano-environment produced by colloidal lithography by human fibroblasts.* Exp Cell Res, 2004. **295**(2): p. 387-394.

228. Jones, A. T., *Macropinocytosis: searching for an endocytic identity and role in the uptake of cell penetrating peptides.* Journal of Cellular and Molecular Medicine, 2007. **11**(4): p. 670-684.

229. Boado, R. J., Tsukamoto, H., and Pardridge, W. M., *Drug delivery of antisense molecules to the brain for treatment of Alzheimer's disease and cerebral AIDS.* J Pharm Sci, 1998. **87**(11): p. 1308-1315.

230. Jayawarna, V., Richardson, S. M., Hirst, A. R., Hodson, N. W., Saiani, A., Gough, J. E., and Ulijn, R. V., *Introducing chemical functionality in Fmoc-peptide gels for cell culture.* Acta Biomaterialia, 2009. **5**(3): p. 934-943.

231. Boggs, A., *The Therapeutic Value of Salicylic Acid.* Br Med J, 1878. **2**(928): p. 558-9.

232. Olson, K. B. and Greene, J. R., *Evaluation of 5-fluorouracil in the treatment of cancer.* Journal of the National Cancer Institute, 1960. **25**(1): p. 133-140.

233. Rao, K. S. V. K., Rao, K. M., Kumar, P. V. N., and Chung, I.-D., *Novel Chitosan-based pH Sensitive Micro-networks for the Controlled*

Release of 5-Fluorouracil. Iranian Polymer Journal, 2010. **19**(4): p. 265-276.

234. Qian, F., Nasongkla, N., and Gao, J. M., *Membrane-encased polymer millirods for sustained release of 5-fluorouracil.* Journal of Biomedical Materials Research, 2002. **61**(2): p. 203-211.

235. Kaiser, N., Kimpfler, A., Massing, U., Burger, A. M., Fiebig, H. H., Brandl, M., and Schubert, R., *5-Fluorouracil in vesicular phospholipid gels for anticancer treatment: entrapment and release properties.* Int J Pharm, 2003. **256**(1-2): p. 123-31.

236. Holte, O., Onsoyen, E., Myrvold, R., and Karlsen, J., *Sustained release of water-soluble drug from directly compressed alginate tablets.* Eur J Pharm Sci, 2003. **20**(4-5): p. 403-7.

237. Singh, B., Chauhan, G. S., Sharma, D. K., Kant, A., Gupta, I., and Chauhan, N., *The release dynamics of model drugs from the psyllium and N-hydroxymethylacrylamide based hydrogels.* Int J Pharm, 2006. **325**(1-2): p. 15-25.

238. Xu, Y., Yin, H., Lu, Y., Yin, S., Wu, H., Jiang, I., and Wada, Y., *Size- and morphology-controlled preparation of extra fine salicylic acid crystallites by organic modifiers.* Materials Letters, 2006. **60**(23): p. 2873-2876.

239. Siepmann, J. and Siepmann, F., *Mathematical modeling of drug delivery.* Int J Pharm, 2008. **364**(2): p. 328-43.

240. Chouhan, R. and Bajpai, A. K., *An in vitro release study of 5-fluoro-uracil (5-FU) from swellable poly-(2-hydroxyethyl methacrylate) (PHEMA) nanoparticles.* J Mater Sci Mater Med, 2009. **20**(5): p. 1103-14.

241. Lin, M. S., Chen, L. Y., Tsai, H. T., Wang, S. S., Chang, Y., Higuchi, A., and Chen, W. Y., *Investigation of the mechanism of beta-amyloid fibril formation by kinetic and thermodynamic analyses.* Langmuir, 2008. **24**(11): p. 5802-8.

242.   Guo, Z. and Thirumalai, D., *The nucleation-collapse mechanism in protein folding: evidence for the non-uniqueness of the folding nucleus.* Fold Des, 1997. **2**(6): p. 377-91.

243.   Edwin, N. J., Hammer, R. P., McCarley, R. L., and Russo, P. S., *Reversibility of beta-Amyloid Self-Assembly: Effects of pH and Added Salts Assessed by Fluorescence Photobleaching Recovery.* Biomacromolecules, 2010. **11**(2): p. 341-347.

244.   Mohsen-Nia, M., Amiri, H., and Jazi, B., *Dielectric Constants of Water, Methanol, Ethanol, Butanol and Acetone: Measurement and Computational Study.* Journal of Solution Chemistry, 2010. **39**(5): p. 701-708.

245.   Sirotkin, V. A. and Winter, R., *Volume Changes Associated with Guanidine Hydrochloride, Temperature, and Ethanol Induced Unfolding of Lysozyme.* Journal of Physical Chemistry B, 2010. **114**(50): p. 16881-16886.

246.   Grinberg, V. Y., Grinberg, N. V., Burova, T. V., Dalgalarrondo, M., and Haertle, T., *Ethanol-induced conformational transitions in holo-alpha-lactalbumin: Spectral and calorimetric studies.* Biopolymers, 1998. **46**(4): p. 253-265.

247.   Sassi, P., Onori, G., Giugliarelli, A., Paolantoni, M., Cinelli, S., and Morresi, A., *Conformational changes in the unfolding process of lysozyme in water and ethanol/water solutions.* Journal of Molecular Liquids, 2011. **159**(1): p. 112-116.

248.   Dufour, E., Robert, P., Bertrand, D., and Haertle, T., *Conformation changes of beta-lactoglobulin - an ATR infrared spectroscopic study of the effect of pH and ethanol.* Journal of Protein Chemistry, 1994. **13**(2): p. 143-149.

249.   Jordens, S., Adamcik, J., Amar-Yuli, I., and Mezzenga, R., *Disassembly and reassembly of amyloid fibrils in water-ethanol mixtures.* Biomacromolecules, 2011. **12**(1): p. 187-93.

250. Andersen, K. B., Castillo-Leon, J., Hedstrom, M., and Svendsen, W. E., *Stability of diphenylalanine peptide nanotubes in solution.* Nanoscale, 2011. **3**(3): p. 994-8.

251. Yan, S., Zhu, J., Wang, Z., Yin, J., Zheng, Y., and Chen, X., *Layer-by-layer assembly of poly(l-glutamic acid)/chitosan microcapsules for high loading and sustained release of 5-fluorouracil.* Eur J Pharm Biopharm, 2011. **78**(3): p. 336-45.

252. Delnobile, M. A., Mensitieri, G., Netti, P. A., and Nicolais, L., *Anomalous diffusion in poly-ether-ether-ketone.* Chemical Engineering Science, 1994. **49**(5): p. 633-644.

253. Costa, P. and Sousa Lobo, J. M., *Modeling and comparison of dissolution profiles.* Eur J Pharm Sci, 2001. **13**(2): p. 123-33.

254. Wang, L. and Tang, X., *A novel ketoconazole bioadhesive effervescent tablet for vaginal delivery: design, in vitro and 'in vivo' evaluation.* Int J Pharm, 2008. **350**(1-2): p. 181-7.

255. Alkhraisat, M. H., Rueda, C., Cabrejos-Azama, J., Lucas-Aparicio, J., Marino, F. T., Torres Garcia-Denche, J., Jerez, L. B., Gbureck, U., and Cabarcos, E. L., *Loading and release of doxycycline hyclate from strontium-substituted calcium phosphate cement.* Acta Biomater, 2010. **6**(4): p. 1522-8.

256. Ofori-Kwakye, K. and Fell, J. T., *Biphasic drug release from film-coated tablets.* Int J Pharm, 2003. **250**(2): p. 431-440.

257. Ofori-Kwakye, K. and Fell, J. T., *Biphasic drug release: the permeability of films containing pectin, chitosan and HPMC.* Int J Pharm, 2001. **226**(1-2): p. 139-145.

258. Maggi, L., Machiste, E. O., Torre, M. L., and Conte, U., *Formulation of biphasic release tablets containing slightly soluble drugs.* European Journal of Pharmaceutics and Biopharmaceutics, 1999. **48**(1): p. 37-42.

259. Cai, C., Mao, S., Germershaus, O., Schaper, A., Rytting, E., Chen, D., and Kissel, T., *Influence of morphology and drug distribution on the release process of FITC-dextran-loaded microspheres prepared with*

different types of PLGA. Journal of Microencapsulation, 2009. **26**(4): p. 334-345.

260. Raman, C., Berkland, C., Kim, K., and Pack, D. W., *Modeling small-molecule release from PLG microspheres: effects of polymer degradation and nonuniform drug distribution.* Journal of Controlled Release, 2005. **103**(1): p. 149-158.

261. Yang, Y. Y., Chung, T. S., and Ng, N. P., *Morphology, drug distribution, and in vitro release profiles of biodegradable polymeric microspheres containing protein fabricated by double-emulsion solvent extraction/evaporation method.* Biomaterials, 2001. **22**(3): p. 231-241.

Appendix A

Diphenylalanine nanotube production yield calculation

The percentage nanotube production is calculated in such a way: freshly prepared nanotube suspensions were evaporated overnight at 65 °C in an oven. The collected solid at the end of the process was mixed with ddH2O and centrifuged for 5 minutes at 10,000 rpm. The supernatant was removed after centrifugation and the purified nanotubes were again evaporated and weighed. The yield of production was calculated by dividing the weight of purified nanotubes by the total weight of FF peptide used. The calculation was repeated three times and data is presented as mean±SEM.
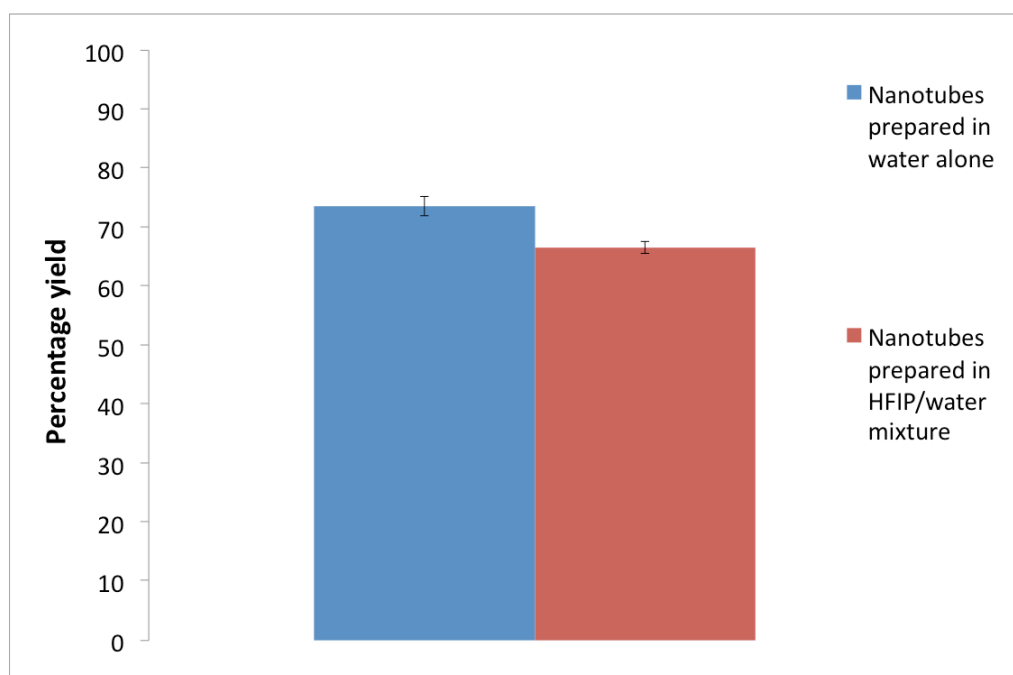
Appendix B

Animations

The video on the enclosed CD contains high-speed time-lapse sequence of TIRM images of HeLa cells exposed to FF nanotube suspension (1000 μg/ml).

To view the animation, copy and paste file to Desktop and open.